

## Design and Fabrication of Stretchable Photonic Fibers

Présentée le 11 mai 2021

Faculté des sciences et techniques de l'ingénieur  
Laboratoire des fibres et matériaux photoniques  
Programme doctoral en science et génie des matériaux

pour l'obtention du grade de Docteur ès Sciences

par

**Nicola BARTOLOMEI**

Acceptée sur proposition du jury

Prof. F. Nüesch, président du jury  
Prof. F. Sorin, directeur de thèse  
Prof. C. Hou, rapporteur  
Prof. R. Rossi, rapporteur  
Dr Y. Leterrier, rapporteur





"Thank God we don't have to kill the stars!

What if a man was supposed to try and kill the moon or the sun every day?

What if the sun and the moon run away like the fish?"

— Ernest Hemingway, *The Old Man and the Sea*

To my family and friends.

# Abstract

Optical fibers have reshaped the technological landscape, from optical networks and high-speed data communication to in situ imaging and non-invasive surgery methods. The revolution allowed by these fibers has been made possible by its fabrication method, the thermal drawing process, which combines high scalability and nanoscale fabrication accuracy. Despite tremendous successes, silica step-index and photonic crystal fibers have held intrinsic limitations due to their mechanical rigidity and fragility, limiting their possible applications . There is however an increasing demand for optical fibers that could guide light efficiently while sustaining large deformations in fields like robotics, smart textiles and the automotive world. Other fields in sensing, healthcare or advanced textiles could benefit from soft fibers that could display tunable optical effects. Techniques like lithography and molding have proven valuable to fabricate complex elastomeric photonic fibers, but their limited scalability intrinsically limits their use in several fields of application. On the other hand, scalable fabrication techniques like extrusion guarantee the desired throughput but fail to deliver the architectural complexity required to realize soft fibers advanced optical properties.

In this thesis, we propose to exploit the thermal drawing process to realize different

types of soft and highly stretchable optical fibers, from the classic step-index architecture to 1D photonic crystal fibers, liquid core fibers and 2D photonic crystal fibers. To achieve this overall objective, we first establish a theoretical framework to evaluate the material requirements from the rheological, optical and mechanical point of view. After selecting the materials, we develop a step-by-step fabrication process that starts from the material pellets and ends with the fabrication of meters of elastomeric photonic fiber via thermal drawing. We then move on to fully characterize the optical and mechanical properties of the fibers and design several fiber-based devices with specific optical effects.

More specifically in Chapter 2, we demonstrate the materials selection, innovative fabrication process, and the optical and mechanical characterizations to realize a soft optical wave-guide based on a step-index design. To highlight its optical and mechanical performance, we demonstrate a strain sensing sport gear that integrates this newly developed fiber. In chapter 3, we go one step further in the control over feature size by going about a similar demonstration for a 1D photonic crystal fibers based on all-elastomeric materials, with feature sizes down to sub-100 nm. We show in particular a mechanochromic fiber that can reversibly change color upon stretching. In Chapter 4, we propose a series of other fiber architectures based on our scientific and technological achievements that include a multicore stretchable step-index fiber that form the basis of an advanced demonstrator of a soft fiber with multiple channels and functionalities found in endoscopes. We also present preliminary results on a liquid-core step index fiber, and a stretchable 2D photonic crystal fiber, that pave the way towards highly complex and high-performance soft optical fiber devices.

Key words: Photonics, material science, optical fiber, stretchable optical fiber, thermal drawing, elastomers, optical fiber sensors, photonic crystal fiber, advanced textiles.

# Résumé

Les fibres optiques ont remodelé le monde technologique tel que nous le connaissons aujourd'hui, des réseaux optiques et de la communication de données à haute vitesse à l'imagerie in situ et aux méthodes de chirurgie non invasive. La révolution apportée par les fibres optiques n'a été possible que grâce à sa méthode de fabrication, le procédé d'étirage à chaud, qui combine une grande scalabilité et une précision de fabrication à l'échelle nanométrique. Néanmoins, les fibres optiques à saut d'indice de silice et à cristal photonique ont conservé des limitations intrinsèques en raison de leur rigidité mécanique et de leur fragilité, restreignant leurs possibilités d'application. Il existe cependant une demande croissante pour des fibres optiques capables de subir de grandes déformations dans des domaines tels que la robotique, les textiles intelligents et le monde automobile, ou qui pourraient présenter des cristaux photoniques accordables pour des applications dans les textiles et les capteurs. Des techniques telles que la lithographie et le moulage se sont avérées adaptées pour fabriquer des fibres photoniques complexes à base d'élastomères, mais leur évolutivité limitée restreint intrinsèquement leurs possibilités d'application. D'autre part, les techniques de fabrication scalables comme l'extrusion permettent le débit souhaité mais ne parviennent pas à fournir la complexité architecturale requise par ces

fibres. Dans cette thèse, nous proposons d'exploiter le procédé d'étirage à chaud pour réaliser différents types de fibres à cristal photonique, de l'architecture classique à saut d'indice et à cristaux photoniques 1D, aux fibres à noyau liquide et aux fibres à cristaux photoniques 2D. Pour arriver à ce résultat, nous établissons d'abord un cadre théorique pour évaluer les exigences en matériaux d'un point de vue rhéologique, optique et mécanique. Après avoir sélectionné les matériaux, nous développons un processus de fabrication étape par étape qui commence à partir des pastilles de matériau et se termine par la fabrication de mètres de fibre photonique élastomérique par étirage à chaud. Nous passons ensuite à la caractérisation complète des propriétés optiques et mécaniques des fibres et finissons par concevoir un dispositif qui exploite leurs propriétés. Cette approche est appliquée à une fibre à saut d'indice entièrement extensible dans le deuxième chapitre, à une fibre à cristal photonique 1D extensible dans le troisième chapitre et à une fibre saut d'indice à noyau liquide, une fibre à cristal photonique 2D extensible et une étape extensible multicœur -index fibre dans le quatrième chapitre.

# Contents

<b>Abstract</b>	<b>i</b>
<b>List of figures</b>	<b>vii</b>
<b>List of tables</b>	<b>xv</b>
<b>1 Introduction</b>	<b>1</b>
1.1 Soft optics . . . . .	1
1.1.1 Tunable lenses . . . . .	3
1.1.2 Self-assembly 3D structures . . . . .	5
1.2 Soft optical waveguides and fibers . . . . .	7
1.3 Soft Photonic Crystal fibers . . . . .	12
1.4 Thermal drawing . . . . .	15
<b>2 Stretchable step-index fiber</b>	<b>19</b>
2.1 Theoretical introduction . . . . .	20
2.2 Materials . . . . .	24
2.3 Fabrication . . . . .	26
2.4 Optical and mechanical properties . . . . .	28
2.5 Strain sensing . . . . .	32

<b>3</b>	<b>Soft 1D Photonic crystal fiber</b>	<b>37</b>
3.1	Theoretical introduction . . . . .	37
3.1.1	Computational methods for film stack reflectivity . . . . .	39
3.1.2	Computational methods for chromaticity determination . . . . .	42
3.2	Fabrication . . . . .	46
3.2.1	Design and Material selection . . . . .	46
3.2.2	Core fabrication . . . . .	50
3.2.3	First generation fibers - casting and rolling . . . . .	51
3.2.4	second generation fibers - Dip coating . . . . .	53
3.3	Results . . . . .	59
3.3.1	First generation fibers - Casting and rolling . . . . .	59
3.3.2	Second generation fibers - Dip coating . . . . .	60
<b>4</b>	<b>Alternative architectures for stretchable optical fibers</b>	<b>71</b>
4.1	Multicore stretchable optical fiber . . . . .	71
4.2	Liquid core Stretchable optical fiber . . . . .	75
4.3	Liquid-based 2D photonic fiber . . . . .	84
<b>5</b>	<b>Conclusion</b>	<b>89</b>
5.1	Stretchable step-index fiber . . . . .	89
5.2	Soft 1D photonic crystal fiber . . . . .	90
5.3	Alternative architectures for Stretchable optical fibers . . . . .	91
5.3.1	Multicore stretchable optical fiber . . . . .	91
5.3.2	Liquid core Stretchable optical fiber . . . . .	92
5.3.3	Liquid-based 2D photonic fiber . . . . .	92
	<b>Bibliography</b>	<b>101</b>

# List of Figures

1.1	(a) DEA membrane (1), frame (2,3) and passive elastomer membrane forming the lens. (b) 3D cross-section. (c) Optical photograph of the lens in front of a grid. (d) Lens at rest state. (e) Lens under actuation. [7]	4
1.2	Top view(a) and cross view (b) of the PAAm–P(St–MMA–AA) PC hydrogel.[17]	6
1.3	Uv- visible and NIR reflection spectra of the opal films in different humidity conditions.[17]	7
1.4	a)Hydrogel step index fiber and (b) its fabrication steps [24] c) Stretchable PDMS waveguide for optical linking of LEDs and diodes[37]	9
1.5	(a)Stretchable fiber fabrication steps and respective cross-section , (b,c,d) waveguides with different LEDs, waved and in a knot.(e) schematics and cross-section of the soft innervated finger.[38]	9
1.6	Fabrication schematics of the bandgap fibers: the spin-coated double film of elastomer is transferred to a liquid surface and rolled on itself [45].	13
1.7	Mechanoresponsive photonic bandgap fibers confirm the predicted stress patterns for the trefoil knot (A) and the figure eight knot (B) [46].	13
2.1	A light ray entering at the maximal acceptance angle and being transmitted through total reflection mechanism[65].	22



2.2	top) Rheological properties: Loss modulus, storage modulus and complex viscosity of PC (a) and SEBS (b). c) TEM images of the preform and the fibers that were drawn at 220 oC and m145 oC. The PS domains appear dark due to the RuO4 staining. d) Rheological properties of Geniomer. . . . .	25
2.3	a) Schematic of the fabrication steps for the step index fiber preform, rolling a film of low refractive index polymer around a cylinder of SEBS. b) Schematic of an alternative fabrication technique of the preform. The SEBS core is stretched and inserted into a hollow cylinder of low refractive index polymer. c) Schematic of the thermal drawing process. d) Tens of meters of fiber obtained by the drawing of one preform. e) Portion of the fiber at rest (top) and while stretched (bottom). . . . .	27
2.4	a, Attenuation coefficient of the fiber in the visible and near-IR range, obtained through cut-back measurement. b, Light transmission performance of the fiber in different media, compared with the performance of the core without cladding. c, Cross section of the step-index fiber obtained with thermal drawing transmitting white, red, blue and green light. The cladding elastomer(a) has a refractive index of 1.42 while the core (b) refractive index is 1.52 . . . . .	29
2.5	a) Tensile test of the fiber until the mechanical failure b) Dynamic tensile test of a fiber stretched between 0 and 100% multiple times. c) Relative losses of the light transmitted versus the indentation depth in a 1 mm diameter fiber. . . . .	32
2.6	a, Relative light transmission of a single core fiber while stretched and (b) cycled at 100% elongation. . . . .	33

- 2.7 a) Light intensity dependence (blue) and force dependence (red) versus absolute elongation of a single core fiber. b) The stretch sensing device, composed of an optical fiber with LED source at one end and photodiode at the opposite end, is clipped to an elastic band. The signal is analyzed by the Arduino in the black box and the force applied is assessed by the number of LEDs that turn on the box. c) Transmitted light intensity versus force applied on the elastic band. The orange regions highlight the points where the force is too low (one LED illuminated out of three) and too high (all three LEDs illuminated). The green region represents the adequate amount of applied force (2 LEDs). . . . . 35
- 3.1 a) Double layer on a substrate with thicknesses  $d_1$  and  $d_2$ , interfaces  $r_o$ ,  $r_1$  and  $r_2$  and the complex reflectivity of layer 2 as  $\rho_2$ . b) The same two layer stack with the second layer replaced by the effective complex reflectivity.  $\rho$  is the effective complex reflectivity of the whole stack.[70] 40
- 3.2 a) The two graphs display the reflectivity of a multilayer stack, in this case a Bragg mirror made of 3 doublestacks with thickness of each layer of 200 nm and refractive index of 1.52 and 1.41, for parallel (1) and perpendicular (2) polarisation. The x axis displays all the possible incident angles while the y axis the wavelength of the incident light. The colorbar defines the reflectivity value. b) Reflectivity plot for a Bragg stack at AOI=0 (1) and AOI=60 (2). . . . . 42

3.3	a) The sensitivity spectra of the human cone cells for short (blue), middle (green) and long (red) wavelengths. b) The chromaticity functions $\bar{X}(\lambda)$ , $\bar{Y}(\lambda)$ and $\bar{Z}(\lambda)$ , clearly recalling the sensitivity spectra of the human eye. c) The Chromaticity diagram displaying all the possible colors that can be described. The black line in the center shows the black body color trajectory and their temperatures. [72]	45
3.4	Representation of the cross-sections of two design hypothesis for the stretchable photonic crystal fiber: a) A hollow core fiber with the multi-layer stack deposited on the inside of the core. b) A solid core fiber with the photonic crystal deposited on the outside of the core.	46
3.5	Simulation of the reflectivity profile of Bragg multilayer mirrors, all made of transparent materials with refractive index $n_1=1.41$ $n_2=1.52$ , but with a different number of layers deposited.	47
3.6	a) Illustration of the streamlines in the solution when the substrate is withdrawn vertically. b) Film thickness vs withdrawal speed, clearly showing the two dip coating regimes. c) Illustration of the streamlines in the solution when the substrate is withdrawn vertically and in presence of strong capillary reflow.[73] b) Illustration of the different passages of the dip coating process.	54
3.7	Deposited thickness vs concentration in Chloroform for the three elastomers under investigation. The values are fitted by a) a polynomial curve $h_x = aC^{3/2}$ and b) a generic curve $h_x = aC^{3/2} + b$ .	57
3.8	a,b) Optical microscope images of the preform after one step of drawing with low draw-down ratio: the core, films and claddings are still visible. Optical microscope image of the fiber obtained, with no polarization filter (c) and polarization filter tuned to increase the fiber reflectivity (d).	59

3.9	a) Optical image of a stack of alternating films deposited with dip-coating. b) SEM image of the cross section of a fiber after drawing. . . . .	61
3.10	a) Image of a fiber with main resonance in the IR that, under stretching and after the removal of its cladding, shows a bright red color. b) A fiber that shows different colors without removing its cladding. c) A fiber stripped of its cladding under different stretch conditions. . . . .	62
3.11	SEM images of the multilayer stack deposited on the outside of a drawn fiber, after the removal of the cladding. . . . .	64
3.12	SEM images of the multilayer stack deposited on the inside of a hollow core fiber, after drawing. . . . .	65
3.13	a) The recorded reflection spectra of the same portion of a fiber under different stretch extensions, before any data processing. Although the presence of the strong internal reflection due to the beam splitter, not collected at the fiber tip, the resonance peak and its shift is clearly visible. b) The position of the maximum of the resonance peaks, calculated after data processing of the curves shown in the top graph, vs. the relative elongation that the fiber was undergoing. The fitting curve confirms the adherence of the results to the mechanical model proposed to quantify the shift of the color. . . . .	66
3.14	The resonance peaks recorded from their appearance in the recorded spectrum to their disappearance. They were recorded by keeping the fiber tip always perpendicular to the suspended drawn fiber and moving the along the z axis. . . . .	68
3.15	a) The simulated resonance peak (1) and their position on the Chromaticity diagram (2). b) The resonance peaks measured experimentally (1) and their position on the diagram (2). . . . .	69

- 4.1 A 7-core stretchable optical fiber is squeezed (a), bent (b) and shaped into a knot (c). Big deformations provoke, as expected, light leakage but don't prevent light to reach the tip of the fiber. . . . . 72
- 4.2 The graph on the right displays the intensity of light collected collectively by the 3 external cores (b) after it was transmitted through the central core (a) and reflected by a flat object (c) versus the distance of the reflecting object (d). . . . . 73
- 4.3 a) Cross-section of the stretchable endoscope: the central core, entitled to guide light, is green while the cores devoted to collect light are transmitting red light. A metallic wire tool is inserted through the hollow channel devoted while the channels for liquid and gas are empty. b,1, 2) The metallic wire can be extracted from the fiber head and controlled to move and turn in different directions c), The Red liquid is inserted with a syringe in a hollow core and liquid easily travels the channel (1) and reaches the tip of the fiber (2) . . . . . 74
- 4.4 a,b,c) Preforms with silicone oil in the core, ready to be drawn. d) Optical microscope image of the fiber after 1 (1) and 2 (2) drawing processes. e) optical image of the cross-section of two fibers, with core diameter down to  $3.8\mu m$ . . . . . 77
- 4.5 Losses of the fiber with hollow core (a) and Liquid core (b) in the visible and low-IR range, obtained through cut-back measurement. . . . . 80
- 4.6 Transmission losses of fibers with different grades of PM oils in the core: PM-50 (green), PM-125(red) and a mixture PM-50:PM-125=6:1 (blue). . . 82
- 4.7 a) Transmission losses of fibers with different diameters. b) effective transmission losses of fibers under stretching). . . . . 83

4.8	a) Rendered image of the design of the structure to insert in the mould. b)The structure with metallic needles ready to be inserted. c) The structure after the polymer has flown around it. . . . .	85
4.9	a) A cross-section of the polymer preform after all the rigid parts have been removed. b) The preform getting filled with Silicone oil through vacuum pressure. . . . .	86
4.10	La,c)Microscope images of the cross-section of the fiber after 1 drawing step. b,d) Microscope images of the cross-section of the fiber after two drawing steps. . . . .	87





## List of Tables





# 1 Introduction

Soft materials and optical materials have developed following parallel tracks for a long time. Until relatively recently optical components such as optical lenses and reflectors, have been made out of hard materials like glass and metal. When soft polymers were first synthesized and implemented in devices, their optical properties were far from ideal and prevented their use in any application that required manipulation of light. In this chapter we discuss in detail how, in the last decades, a growing demand for scalability in photonics and a steep improvement in optical properties of soft materials has paved the way for a new research field of soft photonic materials and devices.

## 1.1 Soft optics

Advances in photonics, the science of light and its interaction with the environment, have brought major changes to our everyday lives. Fields like photovoltaics [1], medical treatments[2], lightening and data transmission and processing[3] are now pillars of the world economy and their expansions is due to the evolution of photonic technologies. Despite the high number of fields, applications and optical phenomena

exploited, the class of materials used in the photonic field has remained somewhat limited for a long time. Inorganic semiconductors and noble metals have been the building blocks of most of the technology developed for photonics. The fabrication techniques are also limited and include top-down approaches like mask assisted lithography, physical or chemical vapour deposition (PVD and CVD) and etching. Optical fiber materials, similarly, have been mostly glass and other rigid dielectric materials with similar properties. Conversely from the examples cited before, the most widespread fabrication technique for optical fibers, thermal drawing, allows great scalability and has allowed optical fibers to become a fundamental pillar of photonics and telecommunications. This fabrication technique will be discussed more in detail later in this manuscript. The selection of materials and fabrication techniques that has lead the development of photonics, while very successful, has also revealed some limitations, in regards to fabrication as well as application.

First of all, traditional fabrication techniques like lithography remain difficult to scale, which increases fabrication costs, reduces output and ultimately lessens their impact. Complex 3D photonic structures, for example, composed of different elements, remain difficult or even impossible to fabricate with standard techniques. Secondly, traditional techniques are not well adapted to materials with elastomeric like mechanical properties. The limited choice in material and, therefore, material properties available mostly have limited the use of photonic devices in fields such as in-vivo surgery and other invasive medical techniques where softness and stretchability are necessary in order to avoid, for instance, damage to the host tissue. Several other mechanically demanding environments such as a variety of textiles configurations on mattresses or automotive tissue, would benefit from materials and processes that can combine state-of-the-art photonic based sensing while allowing for mechanical flexibility and softness.

To develop deeper the following review; we can divide optical components into three main categories depending on the ratio between the material features sizes and the wavelength of operation. If the wavelength is one order of magnitude (or more) greater than the feature, the photonic elements act as meta-atoms and their plasmonic, or Mie-type dielectric resonances, determine the overall photonic properties of the materials. These materials are defined as metamaterials[4–6] and go beyond the scope of this manuscript.

If the wavelength is of the same order of magnitude of the material feature size, we are within the realm of nanophotonics, which includes diffraction gratings, on-chip waveguides or resonators, photonic crystals, and photonic micro- and nano-structured glasses and polymers forming optical fibers discussed extensively in chapter 2 and 4. Photonic crystals, particularly relevant in chapters 3 and 4 of this thesis, are ordered periodical structures of dielectric materials with different refractive indices that can show macroscopic photonic features deriving from the collective result of reflection and refraction of light and its ordered microscopic geometrical features. When the structural and geometrical feature sizes of the material are orders of magnitude larger than the wavelength of light we are in the geometrical optics domain. Multimode waveguides and lenses fall into this category. In what follows, we will focus our bibliography exposé on the evolution of the latter two categories of optical devices regarding their development towards mechanically soft components.

### 1.1.1 Tunable lenses

Geometrical optics was the first branch of photonics to be developed. By the middle ages, lens optics and refraction laws were already well known. This knowledge led to the design and fabrication of the first microscopes and telescopes, which paved the

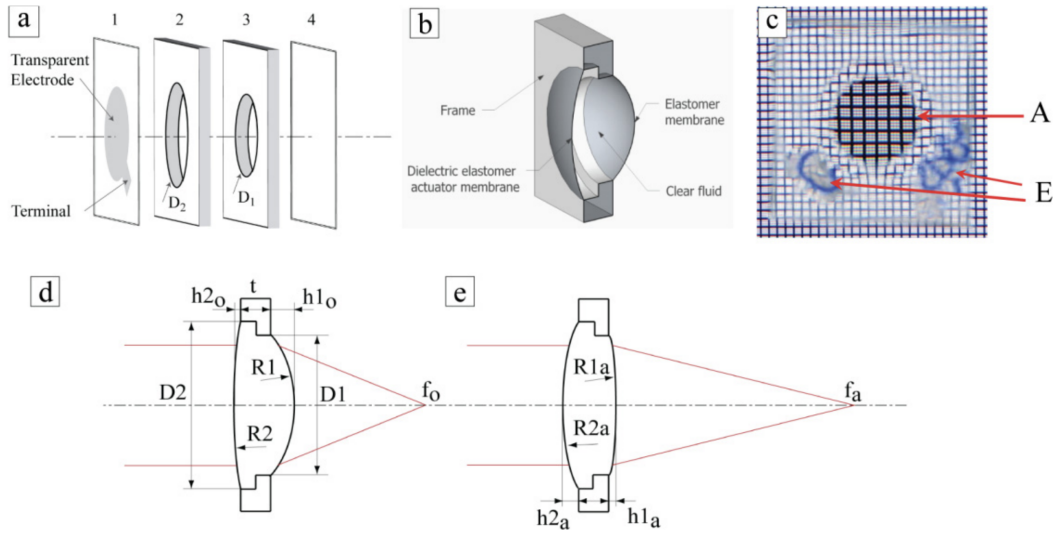


Figure 1.1 – (a) DEA membrane (1), frame (2,3) and passive elastomer membrane forming the lens. (b) 3D cross-section. (c) Optical photograph of the lens in front of a grid. (d) Lens at rest state. (e) Lens under actuation. [7]

way to the study of everything that was too small for, or too away from, the human eye. Being the simplest and most well understood optical elements, lenses were the first photonic devices for which scientists developed a soft and tunable alternative. The first focus tunable lenses were designed in the 1970s and were made of natural rubber encapsulating silicone fluid. Due to their low optical quality, they were used for underwater acoustic wave focusing[8]. With improvements in the optical properties of elastomers, tunable lenses became key components in many optical systems in which space efficiency was vital. The focus in lenses can be tuned in different ways. Focal distance can be controlled by index-changing liquid crystals[9], a method that does not require a change in volume but cannot assure a perfect light transmission because of polarization effects and slow response. Another technique requires the pumping of transparent liquid in order to tune the internal volume of the lens[10]. Lately, with the discovery and control of dielectric elastomers, tunable lenses made of dielectric elastomer actuators have proven to be an optimal alternative to the earlier

lenses and are on their way to revolutionizing several different fields.

Shian et al. have shown how, using dielectric elastomers actuators as membrane to encapsulate transparent liquid, they could obtain a 100% variation of the focal length of the lens and a response time lower than a second [7].

### 1.1.2 Self-assembly 3D structures

In recent years, self-assembly techniques have presented a way to achieve both a top-down fabrication approach for 3D photonic systems and a reliable way to fabricate soft photonic devices. With this technique, photonic devices can be fabricated at low cost and with high throughput, and in some 3D configurations that would be otherwise unachievable. It is usually performed in two steps: first, nanoparticles self-arrange in an ordered crystal (FCC for spheres). When in position, a matrix is inserted between the particles and consolidated. The particles can then be etched, forming a negative crystal, or left in position. We will discuss now some examples of photonic devices obtained through self-assembly with different materials. DNA strands have been used to induce autonomous assembly of nanoparticles in order to obtain Raman-active nanodumbbells[11], enhance surface Raman scattering[12], build plasmonic nanostructures [13] and enhance fluorescence [14].

Hydrogels, colloidal gels made of hydrophilic chains of polymer, have proved to be a good matrix for self-assembling photonic crystals: Lee et al. from the University of Pennsylvania first showed that a photonic crystal obtained from a hydrolyzed, polymerized, crystal colloidal array could be used to sense pH and ionic strength [15], while in 2004 Sharma et al. used the same principle to fabricate a photonic crystal that could sense creatinine concentration, a molecule marker that gives information about kidney dysfunction [16].

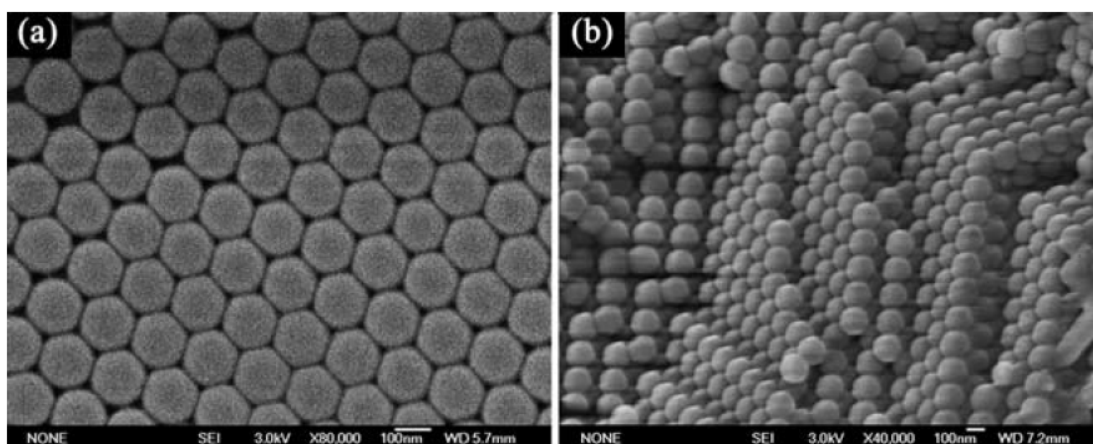


Figure 1.2 – Top view(a) and cross view (b) of the PAAm–P(St–MMA–AA) PC hydrogel.[17]

Due to the high water-intake capability of hydrogels, hydrogel-based photonic crystal are the ideal platform for humidity sensing. In this work from 2008[17], Tian et al. first fabricated a PC made of monodisperse latex spheres that naturally self-assembled in a tetrahedral pattern (Figure 1.2), then infiltrated it with hydrogel precursor and photopolymerized. The intake of water of the PC would change the periodic distance between the embedded spheres and would therefore induce a shift in the visible bandgap, triggering a visible quantitative and passive information change. (fig 1.3).

Elastomers can be used in a similar way to fabricate self-assembled opals, being the matrix that binds together an organized array of nanospheres. As described in the work of Viel et. al.,[18] These spheres, composed of an hard inner core of polystyrene (PS) polymethylmethacrylate (PMMA) and a softer shell of polyethylacrylate (PEA) with a diameter between 150 and 300 nm, self-assemble in a face-centred cubic (FCC) lattice and are then photocrosslinked in an elastomer matrix. The result is a "stretchable opal" where the 111 plane of particles reflects the visible light as a Bragg mirror and stretching can induce a shift in the structural color of the opal. They show that the elastomer-nanospheres composite can undergo cyclical stretching with little hys-

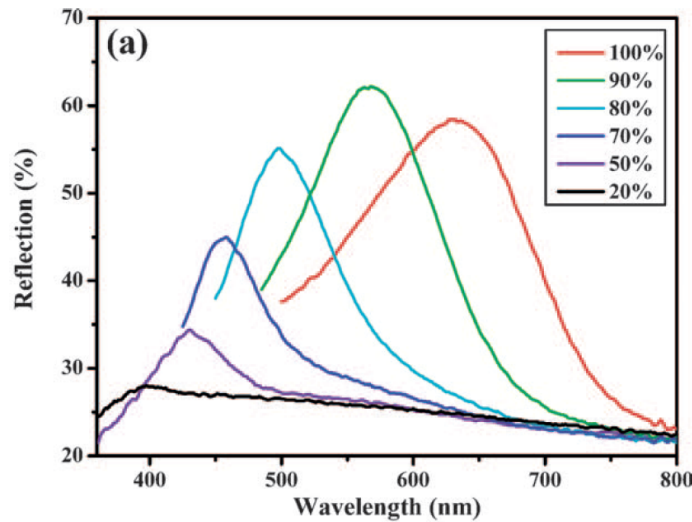


Figure 1.3 – Uv- visible and NIR reflection spectra of the opal films in different humidity conditions.[17]

teresis.

Although not showing clear structural colors as the works discussed previously, the work from Morikawa et al. [19] is noteworthy; they show how an array of cylinders embedded in a co-block elastomer can be aligned via photo-induced massive migration. Using light as a control of the nanoparticle array could be an important step for responsive photonic crystals in the future. Another class of materials that can arrange themselves in a periodical order are biological assemblies. Protein-antibody interactions have been used to form assemblies of silver nanoparticles in a liquid medium, creating a metafluid that displays strong magnetic refraction in the visible[20].

## 1.2 Soft optical waveguides and fibers

Optical fibers have been a fundamental pillar of telecommunications as we know them today[21]. Information, in the form of light, can be transmitted through them with much lower losses and higher bandwidth than through electrical cables, making



them an ideal platform for global communications[22].

Soft optical fibers have known a steep development in the last decade. They are becoming increasingly important in fields like robotics, medical and wearable devices, bioengineering and advanced textiles. In applications related to robotics, optical fibers have been inserted into smart textiles[23] and 3D matrices to create a network of information channels[22]. The combination of light guiding and high deformability makes them the ideal platform for stretch and pressure sensors[24–28]. These sensors are otherwise usually based on electronic properties, such as capacitance and resistivity measurements[29–36], , but the mechanical properties of the sensor are limited by the low stretchability, the limited conductivity of materials, or the possibility of releasing harmful liquids in case of leakage. On the other hand, transparent elastomers can stretch elastically up to 500% and maintain their mechanical and optical properties after thousands of cycles. The dielectric nature of the polymers is also a key feature in all applications that require powerful magnetic fields; as any electronic signal would interfere with the fields, all communications must be based on optical signals. Up to now, fabrication techniques have failed to combine scalable and low-cost output volumes with architectural complexity within the fiber, and their high attenuation coefficient have led to poor optical performance.

The concept of mechanically stretchable optical waveguides was introduced for the first time in 2014 by Missinne et al. [37] from the University of Ghent. The waveguides were fabricated with commercially available PDMS material, where the refractive index contrast was achieved in two ways: by a difference in concentration of curing agent between the core and the cladding, or by adding silicon oil to the precursor of one of the two materials. The bottom cladding of the waveguides was obtained by over-coating and thermally curing the cladding PDMS on a master mold with

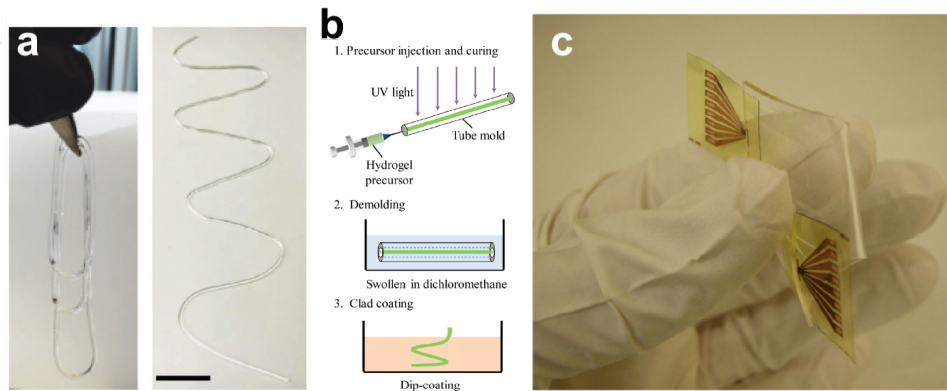


Figure 1.4 – a) Hydrogel step index fiber and (b) its fabrication steps [24] c) Stretchable PDMS waveguide for optical linking of LEDs and diodes[37]

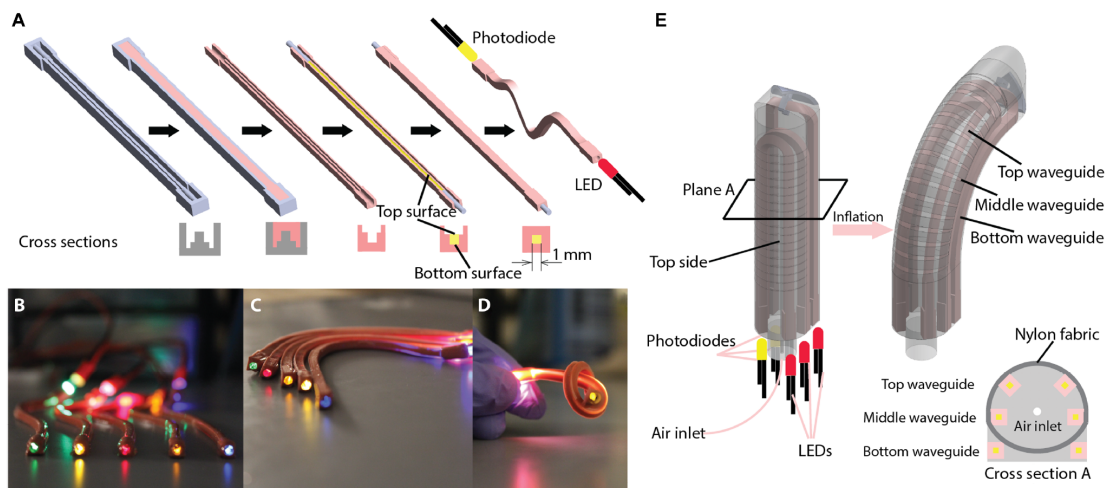


Figure 1.5 – (a) Stretchable fiber fabrication steps and respective cross-section, (b,c,d) waveguides with different LEDs, waved and in a knot. (e) schematics and cross-section of the soft innervated finger. [38]

50x50  $\mu\text{m}$  ribs. When released, a previously cross-linked layer of the same grade of PDMS was positioned on top. The two parts were then connected together after being treated with plasma. The last step consisted in filling the channels obtained with the precursors of the PDMS with a higher refractive index material and curing it. LEDs were then embedded in the waveguides and the fibers were tested for optical losses under stretching and bending.

In 2019 Prayzler et al. [39], rebuilt stretchable waveguides with the same dimension of 50  $\mu\text{m}$  with a similar technique and a grade of PDMS with better optical properties. They reported losses of 0.6 dB/cm in the visible spectrum and 0.76 dB/cm at 650 nm. This family of stretchable waveguides has been successfully integrated into a soft prosthetic hand [38] that could demonstrate a signal-to-noise ratio of 50, stretchability over 85% and could recognize different degrees of surface roughnesses and shapes from a single sweep. Although the waveguides previously presented showed promising results in several applications, the squared geometry of the core still limits its transmission properties and the fabrication technique can barely match the output required for a mass use of these devices.

Thermoplastic elastomers have proven themselves as a valid alternative to cross-linked elastomers as building blocks of soft optical fibers and waveguides. Leber et Al. [27] demonstrated for the first time the fabrication of a step-index stretchable optical fiber in a single-step extrusion process. The two polymers are injected into a co-extruder nozzle from two different extruders. In the nozzle the cladding elastomer is distributed around the extruded core elastomer, which is shaped with a cylindrical cross section. Thermoplastic elastomers display a wider range of refractive indexes compared to cross-linked transparent elastomers, which usually have similar chemical composition, therefore their RI does not shift significantly from that of PDMS. The two extruded polymers have refractive index values of 1.54 for the core and 1.36 for

the cladding. This fabrication technique provides major improvements compared to lithography: for example, the transmission core of the fiber is round, which optimizes light transmission. Furthermore, the the fiber assembly requires only one step compared to the multiple steps of lithography and allows a continuous fiber output, resulting in a much higher yield of fiber length. The fiber showed optimal resistance to cycling and losses around 1 dB/cm for the visible spectrum. A knee brace, a glove and an impact sensor on a tennis racket were equipped with these fibers and were able to sense pressure, stretch and bending.

Wet spinning has been for a long time a valid alternative to fabricate optical fibers. In 2010 Hu et. al [40] conceived an alternative technique, microfluidic wet spinning, that consists in fabricating fibers through the control of coagulant solutions and polymers within adjacent laminar flows. Gursoy et al. [41] developed an elastomer based microfluidic platform to fabricate thermoplastic polyurethane fibers, ensuring a high throughput of material. Another technique suitable for the fabrication of thermoplastic soft fibers could be melt spinning, which consists in extruding polymer pellets and collecting, through a system of pulleys, the fiber that exits the spinneret. A graded index optical fiber has been obtained from melt spinning by Kallweit et al. [42]. The index grading in the cross section of the fiber was obtained through a different cooling rate between the center of the fiber and its superficial layers. Hydrogels have been discussed before as a family of materials that meets many requirements of soft optical devices, and they have many features that make them a good candidate for soft optical fibers as well. Guo et al. [24] demonstrated in 2016 that a core-clad optical fiber made of hydrogel could actually be fabricated and had interesting properties: it could be stretched recursively at elongations of 100% and a maximum axial strain up to 700%. The refractive index difference between the core and the cladding was obtained using a different ratio of precursors in the synthesis of the two hydrogels,

while the fabrication process consisted of molding the core first and then adding the cladding as a coating. They also showed as well that, by doping different parts of the fiber with scattering particles of different sizes, they could detect whether a portion of the fiber was under stretch and, from the scattering cross-section, localize that portion of the fiber.

### 1.3 Soft Photonic Crystal fibers

Photonic crystal optical properties were appreciated by humans long before science developed a full understanding of the phenomena. The bright flash of colors in opals and the deep blues, reds and greens of butterflies have always been known, admired, and emulated. Scientists have turned this admiration into a methodical investigation to reproduce these colors in the laboratory.

Kolle et Al. [43] tried realize a photonic crystal that mimic the structural color of the butterfly *Papilio Blumei*, managing to fabricate, with different layer deposition techniques, the intricate composition of pits and multilayered surfaces that could be observed under the microscope. They obtained a reproduction of its green color, although using only inorganic hard materials. In another work[44] the color of the bluish fruit *Margaritaria Nobilis* was investigated: its structural color derives from tightly packed concentric cylindrical multilayer structures. The researchers managed to reproduce the same structural color in the shape of a fully stretchable fiber.

The two elastomers selected where a high refractive index co-polymer ( $n=1.54$ ) and PDMS ( $n=1.41$ ). The elastomers are spin-coated in the form of films on a silica wafer, transferred as a floating bilayer on a liquid, and rolled around a thin glass rod, then removed as shown in figure 1.6.

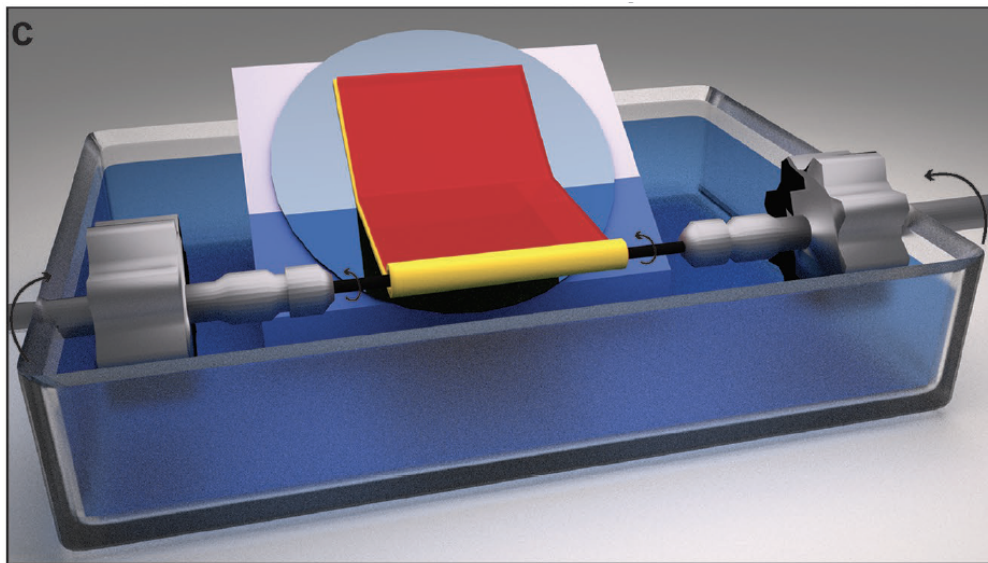


Figure 1.6 – Fabrication schematics of the bandgap fibers: the spin-coated double film of elastomer is transferred to a liquid surface and rolled on itself [45].

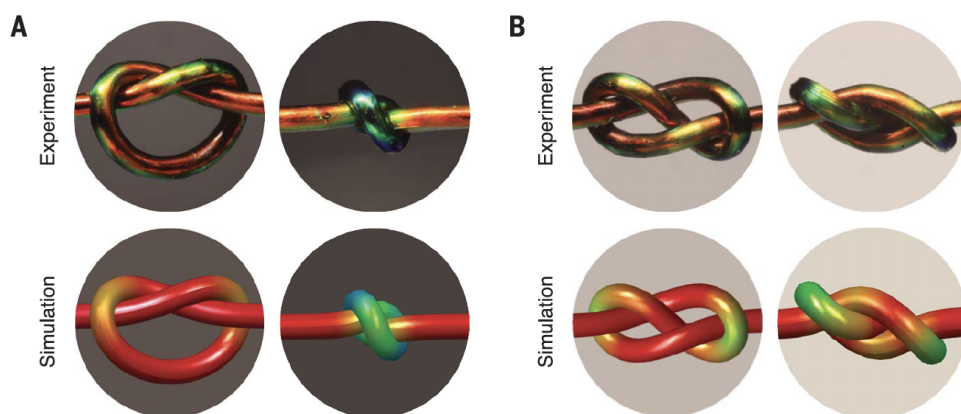


Figure 1.7 – Mechanoresponsive photonic bandgap fibers confirm the predicted stress patterns for the trefoil knot (A) and the figure eight knot (B) [46].

A reversible band-gap shift in the visible spectrum of up to 200 nm was recorded, linked to an axial stretching of 200%. The fine tuning of the layers, accessible by control of the spin-coating technique, and the high number of multilayers forming the Bragg reflector, up to 150, allowed the reflectivity to reach values around 0.9. This last value translates into the bright structural color observable by the naked eye. These fibers have found different applications in the following years. In 2018 Sandt et al.[45] demonstrated how these optomechanical properties could be successfully applied in the field of the medical devices. The fibers used were made of the elastomeric photonic multilayer described above rolled around an extruded elastomer core. The Researchers showed how the colors of these fibers, which were inserted into an elastic bandage, could give a localized information about the pressure applied by the bandage. The color could be univocally associated to a precise value of elongation, which also indicated the precise amount of pressure exerted in that position.

In another recent work, Patil et al.[46], used these fibers to predict the mechanical stability of tangles and knots. The color change of the fiber is localized so that it can display zones of strain and stress on small portions of the fiber. Different knots were made with the fibers, compared with the simulation results and confirmed the theoretical model proposed (figure 1.7).

One final field where these fibers have shown their utility and versatility is vapor sensing. Malekovic et al. [47] have shown that the PDMS and PSPI that composed the bilayers of the photonic stack would swell in the presence of organic vapors such as toluene, benzene, tetrahydrofuran, or chloroform. The swelling induce a change in the thickness of each layer that resulted in a shift of the bandgap peak. As the minimum shift in color perceived by human eye (1-2 nm) can be detected only in the green region, the fibers of this color could have a sensitivity down to 250 ppm for toluene, with a shift of 1 nm. Another note-worthy effort to fabricate polymer

photonic crystal fibers has been carried out by Finalyson et al. [48]. Researchers adapted the extrusion process to stretchable opals[18], already described in a previous section, to the extrusion process. Polymer beads, kept together by a precursor matrix, were extruded through a nozzle and arranged themselves in a periodic structure. After curing, an opal fiber was obtained. The fiber showed structural color and could be tuned through stretching to cover all of the visible wavelengths.

The research efforts discussed in this section clearly point to two main facts, that will shape the future of the soft optical devices research world. First, in the span of a few years stretchable polymers and soft materials in general have become key components in the photonic world, unlocking performances and uses unreachable with the rigid materials used in the past. Second, the fabrication techniques described can't hardly provide the volume of product output required for a device to become ubiquitous in our everyday lives, without sacrificing significant design complexity.

## 1.4 Thermal drawing

The technique mostly used to fabricate multimaterial fibers is thermal drawing from a preform. The preform is first put in a furnace that softens the material and then is pulled uniformly from an external force or with gravity. This top-down process has various advantages. First of all, the architecture of the structure is fabricated in the preform at a macroscopic scale. Second, the law of mass conservation allows the fabrication of extended fiber length starting from a small preform. This technique however puts some limitations on the material that can be used. Some materials, such as cross-linked polymers, can't be reshaped using heat and therefore can't be drawn. A preform formed of different materials can't be drawn if these materials present high



differences in viscosity or melting temperature.

Thermal drawing has been the fundamental fabrication technique for optical fibers, since the fabrication of the first step index fiber [21]. In the recent years hollow core guidance in air has been achieved with the development of photonic crystal fibers, at first [49] and anti-resonant later [50–52].

Since few years ago new materials started to be integrated in fiber drawing: besides already discussed polymers and glasses, metals, semiconductors and insulators were successfully drawn together in a single fiber in order to obtain light sensing features [53]. With the integration of different materials in thermal-processed fibers, thermal drawing has been also considered as a synthesis technique. Through solid state reaction, Nick Orf in 2011 [54], synthesized successfully zinc selenide. The fabrication of selenium nanowires and chalcogenide nanospheres were demonstrated as well [55–57]. New materials integration in fibers opened the field to a new range of applications such as light and heat sensors [53, 57, 58], side emitting lasers with output controlled by liquid crystals [59], touch sensing fibers [60] and piezoelectric fibers for conformal acoustics [61].

Only very recently we have been able to apply this technique to thermoplastic elastomers. For the first time, in 2017, Nguyen et al. [62] fabricated elastomer based fiber with hierarchical structures with this technique and, the same year, Qu et al. [26] showed that purely elastomeric preforms can be drawn in a continuous fiber. After these results, other works showed how this platform is suitable for pressure sensing devices based on soft fibers [63] and as base for soft transmission line sensing [34].

## Thesis objectives

In my thesis project, we wanted to investigate the use of the thermal drawing process to realize advanced soft and micro-structured optical fibers. Each chapter addresses a fundamental question related to this overall objective:

- In Chapter 2, we address the fundamental question as to which soft materials can be compatible with the thermal drawing process. We develop a criteria based on simple rheological analysis, and fabricate a step index optical fiber entirely based on thermoplastic elastomers, via thermal drawing. This result was first published in a paper I co-authored in Adv. Mat., and in a paper more specifically on the optical fiber aspect in SPIE proceedings for which I am the first author.
- In Chapter 3, we go one step further in the nano-structuration of soft optical fibers by demonstrating a 1D photonic band gap fiber entirely made out of thermoplastic elastomers, and with sub-100 nm feature sizes. This is we believe the most advanced soft optical fiber ever made with such a scalable process. We propose different fabrication routes, and demonstrate mechanochromic fiber based devices with reversible color changes upon stretching. A paper is being written up.
- In Chapter 4, we present novel advanced designs based on our knowledge of the processing of thermoplastic elastomers. We in particular demonstrate a multi-core designs and an example of application for novel soft endoscopes. We are submitting a manuscript about these advances .



## 2 Stretchable step-index fiber

As discussed in the introduction, optical fibers, graded and step-index in particular, have been the fundamental building blocks of optical networks and high speed optical data communication. The revolution in telecommunications brought by optical fibers has only been made possible due to its innovative fabrication method, the thermal drawing process, which allows the fiber to combine optimal light transmission, high scalability and cross-sectional design freedom. The process begins with a preform, with the same cross-section of the desired fiber, which is inserted into a furnace and “pulled”. Under the right conditions, the preform flows uniformly into a fiber that maintains the same internal architecture. Currently, kilometers of continuous fiber can be obtained from a single preform in a single process that does not involve bottom up fabrication. This fabrication dramatically decreases the cost of the final fibers, assures a huge output and guarantees superior optical performance.

However, this technique has been limited only to hard materials such as glasses and thermoplastics, as the thermomechanical properties required by the process are rarely found outside of these material families. Until recently, fabrication techniques have failed to combine scalable and low-cost output volumes with complex internal ar-

chitectures for these fibers, and their high attenuation coefficients have led to poor lightening. Scalable methods to fabricate optical fibers such as extrusion[27], melt-spinning[42] or wet-spinning, cannot achieve complexity within the cross-section of the fiber, due to the high grade of melting that the polymer undergoes and to the mechanical solicitations during the fabrication processes. In contrast, fibers assembled via film stacking or with lithography can achieve higher complexity but are limited by high fabrication costs and low volumes[44, 45]. Thermal drawing requires materials with well-defined rheological properties[64] and most of thermoplastic elastomers do not possess the rheological properties that allow a material to be drawn. Until recently, the thermal drawing process was limited to rigid and semirigid materials only[34, 62, 63].

Following a brief theoretical introduction, this chapter will describe how thermal drawing can be used to fabricate soft optical fibers. The success of the process relies on the selection of elastomers with the right thermo-mechanical properties and leads to the large scale-fabrication of stretchable optical fibers possessing a cross-sectional complexity that enables unprecedented functionalities. The fibers are then tested for their optical, mechanical and optomechanical properties. In the last part we will describe the design and fabrication of a device that exploits the extreme stretchability and cyclical resistance of the fiber to build a stretch sensor for elastic gym bands.

## 2.1 Theoretical introduction

As mentioned previously, the fibers we first designed and fabricated fall into the family of step-index fibers. These are optical fibers composed of two transparent materials with different refractive indices: they are organized in a concentric architecture with a central core composed of the material with a higher refractive index and a surrounding

cladding with lower refractive index. Light travels in the core and the cladding shields it from leaking, exploiting the total internal reflection of the light (figure 2.1). We will now introduce some key concepts to describe the light-matter interaction. We can define  $\epsilon$ , the relative electrical permittivity of a material, as:

$$\epsilon = 1 + (P/\epsilon_0 E) \quad (2.1)$$

with  $P$  defined as the polarization of the material, is  $\epsilon_0$  as the permittivity of vacuum and  $E$  the electric field. We then define the permeability of the material as

$$\mu = 1 + (M/H) \quad (2.2)$$

where  $M$  is the magnetization of the material and  $H$  the applied magnetic field. From these two values we can obtain the refractive index of the material, defined as  $n = \sqrt{\epsilon\mu}$ . The refractive index of a medium describes the ratio between the propagation speed of light in the medium compared to light in vacuum. The refractive index of vacuum is therefore  $n=1$  and lights propagates more slowly in materials with higher refractive indices. When light is incident on a material, it can be partially transmitted, reflected or absorbed. In order to explain total internal reflection, we neglect material absorption and assume that surfaces and interfaces are perfectly flat, avoiding scattering. When a light ray, with an incident angle  $\theta_i$ , hits a flat surface between two materials with refractive indices  $n_1$  and  $n_2$ , the light is divided into two rays, one reflected and one transmitted through the second medium. While the reflected ray  $\theta_r$  will have the same angle of the incident, the angle of the transmitted ray  $\theta_t$  can be obtained by

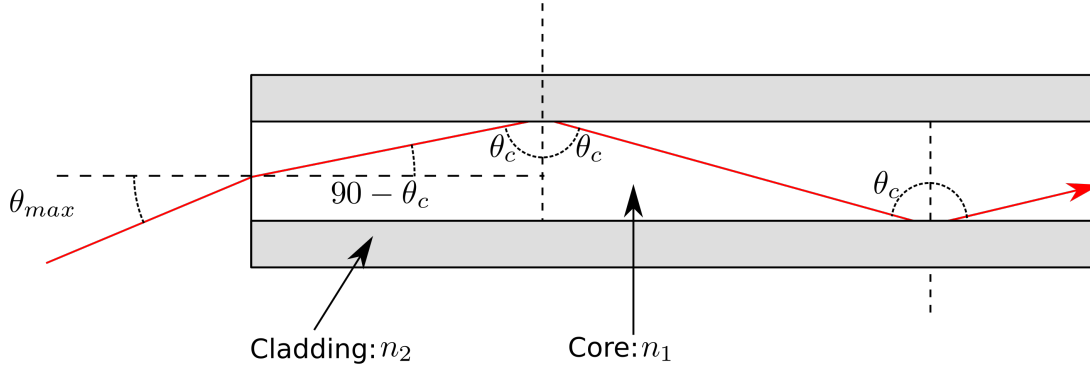


Figure 2.1 – A light ray entering at the maximal acceptance angle and being transmitted through total reflection mechanism[65].

Snell's law:

$$n_1 \cdot \sin \theta_i = n_2 \cdot \sin \theta_t \quad (2.3)$$

From this law, in conditions where  $n_1 > n_2$ , we can easily observe that there is a critical angle  $\theta_c$ , defined as

$$\theta_c = \arcsin \frac{n_2}{n_1} \quad (2.4)$$

at which the refracted angle is parallel to the surface. For angles greater than this, all of the light is reflected back into the medium with higher refractive index. The total internal reflection mechanism that allows light to travel in step- and graded index fibers is based on this principle. We easily recognize the fact that light entering the core, in order to be able to travel, must couple the fiber end with an angle small enough not to be completely reflected by the fiber cross-section or, after entering the core, being refracted into the cladding material. This angle,  $\theta_{max}$  is defined as the acceptance angle. The Numerical Aperture (NA) is a dimensionless number that is usually preferred to describe the degree of acceptancy of a given fiber. It is defined as

$$NA = n_{source} \cdot \sin \theta_{max} = \sqrt{n_1^2 - n_2^2} \quad (2.5)$$

In order to discuss in depth more features of optical fibers, we must introduce new quantities.

We define the fractional index difference as

$$\Delta = \frac{n_1 - n_2}{n_1} \quad (2.6)$$

and we obtain, assuming  $\frac{n_1 + n_2}{2} \approx n_1$ ,

$$NA = n_1 \sqrt{2\Delta} \quad (2.7)$$

We have now all of the elements needed to introduce the V number, which determines how many modes a fiber can support. It is defined as:

$$V = \frac{\pi d}{\lambda} NA = \frac{\pi d}{\lambda} n_1 \sqrt{2\Delta} \quad (2.8)$$

If  $V \leq 2.405$ , the fiber is a single mode fiber, while if  $V > 2.405$  the fiber is multimode. In a single mode fiber light can propagate only in its fundamental guiding mode. This leads to the fact that light propagates with lower attenuation and the information is better preserved, as different modes travel the fiber at different speeds and this discrepancy can "stretch" and induce noise in the light pulse. Single mode transmission is usually helped by a relatively low difference in refractive index, hence numerical aperture. Small numerical aperture insures that light enters the fiber with small angles and reflects fewer times on the core cladding interface, limiting losses. Single mode fiber cores are usually smaller than  $10 \mu m$ , while multimode fiber cores start at around  $50 \mu m$ . Multimode fibers, while not being the preferred fibers for long distance signal



transmission, helpful simplify connections due to their "light gathering" ability[66].

## 2.2 Materials

As discussed before, the selection of the materials to be used in this thesis was a non-trivial process, as the materials must fulfill different requirements in terms of heat resistance, thermo-mechanical properties, optical properties and solubility. Photonic properties are based on internal refraction and reflection of electromagnetic waves in media with different refractive indices. For this reason, every photonic device relies on at least two different media. PC fibers, for example, base their properties on the different refractive indices of silica and air. After investigating different thermoplastic elastomers among fluoropolymers, block-copolymers and silicon-based elastomers, the first polymer selected was styrene ethylene butylene styrene block copolymer (SEBS). It is composed of a styrenic block copolymer, formed by styrene blocks and rubber blocks, with a hydrogenated midblock of styrene-ethylene/butylene-styrene. Block copolymers are formed by two or more homopolymer subunits linked by covalent bonds. From a rheological point of view, a broader requirement for the thermal drawing of a polymeric matrix at high viscosity can be defined as a temperature window where the loss modulus ( $G''$ ) dominates the storage modulus ( $G'$ ) so that the deformation is done in the viscous regime. As shown in Figure 2.2.c, polystyrene blocks do not deform during drawing, but the long chains connecting PS domains soften their physical bonds, lowering  $G'$ . Viscosity does not suddenly drop but the flow remains in the viscous regime due to the high molecular weight: this helps maintain a high value of  $G''$ . Figure 2.2.a,b compares complex viscosity,  $G'$  and  $G''$  of a thermoplastic (polycarbonate, (PC)) commonly used for thermal drawing, and SEBS. The two materials show similar properties at high temperatures. SEBS can be drawn

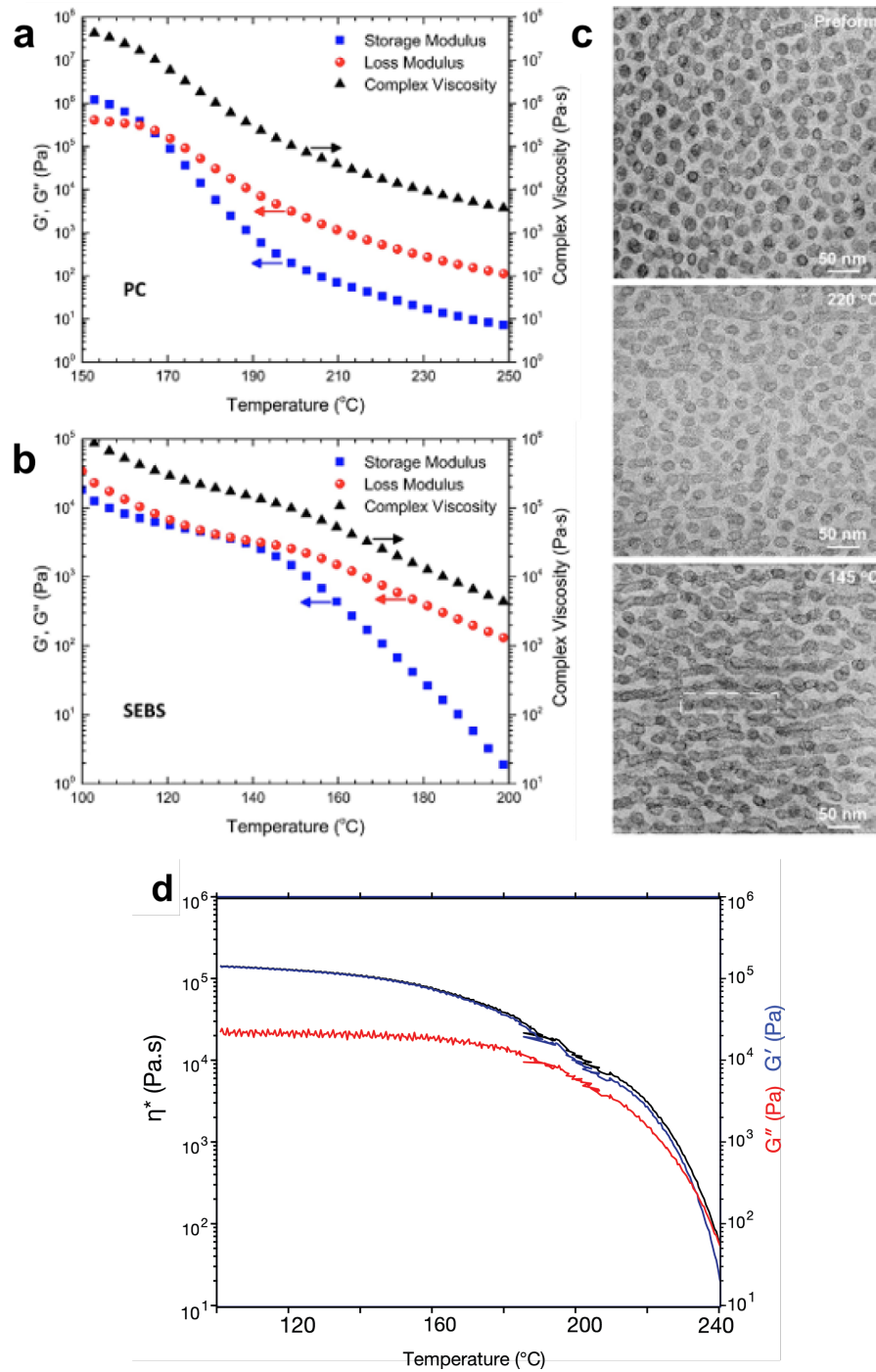


Figure 2.2 – top) Rheological properties: Loss modulus, storage modulus and complex viscosity of PC (a) and SEBS (b). c) TEM images of the preform and the fibers that were drawn at 220  $^{\circ}\text{C}$  and 145  $^{\circ}\text{C}$ . The PS domains appear dark due to the RuO<sub>4</sub> staining. d) Rheological properties of Geniomer.

in long and uniform fibers, and it preserves its high stretchability after drawing. It shows really good resistance to intense heat and extreme elongations, displays good transparency and has a refractive index of  $n=1.52$ .

The second polymer selected was Geniomer 145, a polydimethylsiloxane/urea copolymer. It has properties and behavior under heating that are similar to SEBS, but it is silicone based and displays a lower refractive index,  $n=1.42$ . As we can see from figure 2.2.d, the rheological properties of Geniomer are similar to the ones of SEBS: in the temperature window around  $200^{\circ}$ , the complex viscosity attains values in the same order of SEBS, while the loss and storage moduli have values close to overlapping.

## 2.3 Fabrication

Two different methods were developed to fabricate the preform. The first one requires few fabrication steps, while the second is more complex but allows the fabrication of preforms with different cores in diameter and position. In the first method (Figure 2.3.a), the cylindrical core is obtained by pressing SEBS pellets into a mold placed in a high temperature and low pressure oven, while the low-index elastomer pellets are hot pressed into a uniform film. The film is then rolled around the cylinder and the resulting preform obtained is consolidated again in the oven. In the second method (Figure 2.3.b) the cladding is obtained by pressing the low-index elastomer pellets into a cylindrical mold. Metallic cylindrical bars are placed inside the mold to create a hollow space into which the core material will be inserted. The SEBS cores are also obtained by pressure molding. They are then inserted in the preform while being stretched: when the strain is released the diameter increases and the cores fit the channels. The preform is then consolidated in the oven to increase the adhesion of the different components. The preforms are then inserted into the drawing tower

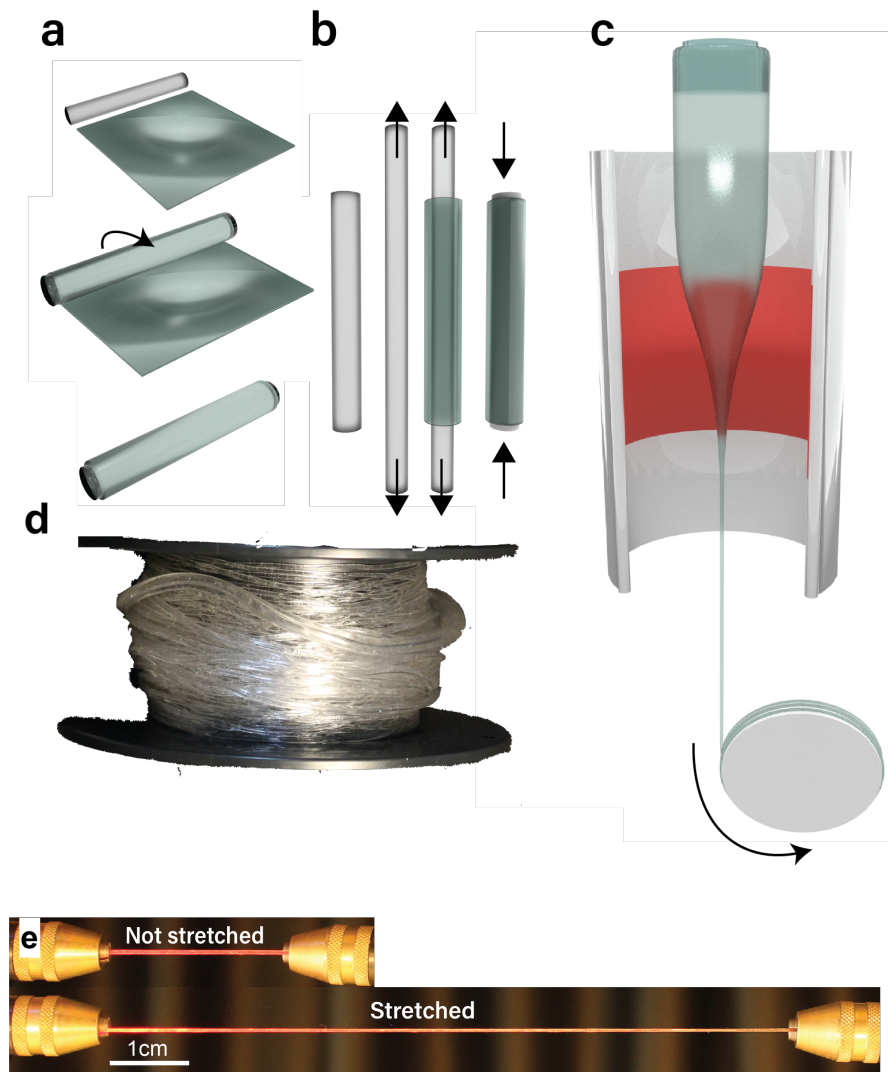


Figure 2.3 – a) Schematic of the fabrication steps for the step index fiber preform, rolling a film of low refractive index polymer around a cylinder of SEBS. b) Schematic of an alternative fabrication technique of the preform. The SEBS core is stretched and inserted into a hollow cylinder of low refractive index polymer. c) Schematic of the thermal drawing process. d) Tens of meters of fiber obtained by the drawing of one preform. e) Portion of the fiber at rest (top) and while stretched (bottom).

furnace and thermally drawn (Figure 2.3.c). The diameter and length of the resulting fiber depends on the drawing ratio, which is defined as the ratio between the diameter of the preform and the diameter of the obtained fiber and which can be calculated with the expression:

$$R = \sqrt{\frac{v_{spool}}{v_{feed}}} \quad (2.9)$$

where  $v_{feed}$  refers to the velocity at which the preform is lowered into the furnace while  $v_{spool}$  is the velocity at which the fiber is pulled out of the furnace and spooled. The diameter of the preforms used was either 2 or 3 cm, while the obtained fiber diameter could be tuned between 3 mm and 500 micrometers. All of the features in the fiber are scaled down with the same ratio, as the features in the preform are mirrored in the fiber. From a preform of 2 cm of diameter and 10 cm of length a fiber of 20 m meters can easily be obtained (Figure 2.3.d). In accordance with the industrial standards, all of the results discussed in this manuscript about single-core fibers refer to fibers with diameter of 1 mm. Preliminary considerations can be assessed for the drawn fiber, as, observing the cross section, light at different wavelengths is successfully confined to the core and the stretching of the fiber - up to 500% as shown in Figure 2.3.e - does not prevent light transmission.

## 2.4 Optical and mechanical properties

We then addressed quantitative measurements of the mechanical and optical properties of the fabricated fiber. The first optical properties that we measured were the

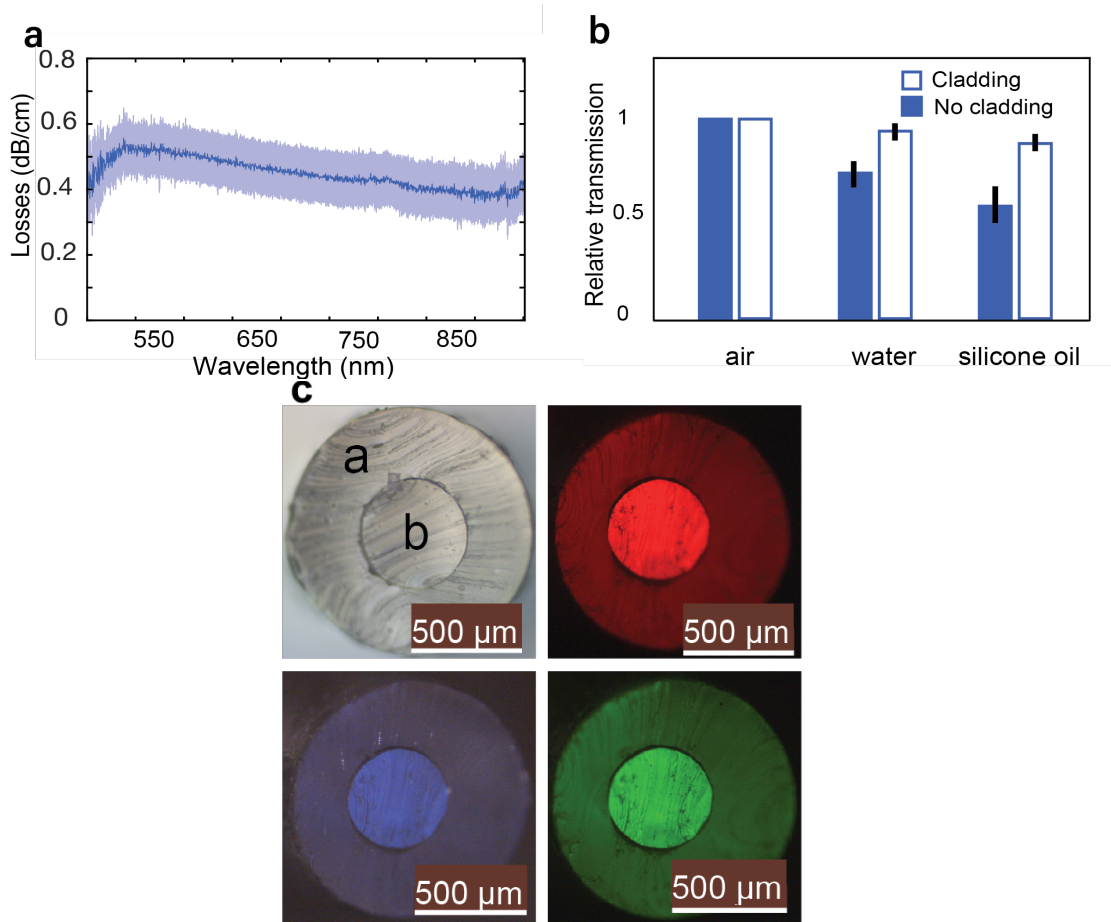


Figure 2.4 – a, Attenuation coefficient of the fiber in the visible and near-IR range, obtained through cut-back measurement. b, Light transmission performance of the fiber in different media, compared with the performance of the core without cladding. c, Cross section of the step-index fiber obtained with thermal drawing transmitting white, red, blue and green light. The cladding elastomer (a) has a refractive index of 1.42 while the core (b) refractive index is 1.52

absolute losses of the fiber for the visible and near IR range. The losses were measured with the cutback technique, which consists in comparing the transmission values of a fiber at its total length to those after it has been shortened multiple times with equally spaced cuts. The results are then plotted on a semi-logarithmic scale that shows the intensity transmitted, in logarithmic scale, versus the length of the fiber. The results are fitted linearly and the slope of the fitting line is the value of the losses, measured in dB/cm.

Figure 2.4.a shows the losses calculated for every wavelength in the visible and near IR range. The losses obtained were around 0.5 dB/cm, varying slightly throughout the spectrum. This value is orders of magnitude lower than that of silica fibers (dB/km) and still far from the results obtained with non-stretchable polymer optical fibers (dB/m)[67], but it shows that this fiber matches the best transmission values of all the stretchable optical fibers with comparable mechanical performance presented in the literature.[24, 27, 39]

We then compared the performances of a step-index fiber and a fiber stripped of its cladding, immersed in different media. The results shown in Figure 2.4.b highlight the importance of the cladding in confining light within the core and obtaining consistent results in different environments: while a fiber with cladding transmits light consistently while immersed in different media, the performance of a fiber with an exposed core depends dramatically on the environment. In addition to these considerations, we must take into account that losses that would also occur if the core is put in contact with an absorbing or transparent material with a higher refractive index. These optical properties clearly show that the fiber studied can efficiently transmit signals for the distances required by applications in medical sensors, smart textiles and robotics. We must now address the characterization of the mechanical properties of the fiber.

From the stress strain curve (Figure 2.5.a) we recognize the expected super elastic

behavior of the fiber, where a super elastic region with lower slope follows the starting elastic region. The overall continuity of the stress recorded shows that the adhesion between the core and cladding materials can sustain large deformations.

We can describe the deformation of the cladding and the core diameter quantitatively: defining the Poisson ratio  $\nu$  as the negative true strain between the true strain  $\epsilon_t$  and the longitudinal strain  $\epsilon_l$   $\nu = -\frac{\epsilon_t}{\epsilon_l}$ , the change in diameter of the core is described by the relation

$$\frac{dt_i}{t_i} = -\nu \frac{dl}{l}. \quad (2.10)$$

There are three different scenarios: if  $\nu_{cladding}$  is bigger than  $\nu_{core}$ , when the fiber is under stretch the cladding, shrinking more, will exert pressure on the core and the adhesion of the two component will be improved. Inversely, if  $\nu_{cladding} < \nu_{core}$ , the fiber will tend to delaminate. The two materials have similar  $\nu$ , therefore we don't observe any delamination when the fiber is under stretch.

If the fiber is stretched multiple times up to 100 % percent, as shown in Figure 2.5.b, we recognize another feature of super elastic polymers: a hysteresis cycle when the fiber undergoes cyclical stretching. Thus far we have investigated the effect of axial stretching, while in fig. 2.5.c we report the effect on transmission of a perpendicular pressure on the fiber on the transmission. The measurements were performed on different fibers of similar diameters. We observed that the drop in transmission that occurs when the fiber is pressed more than 400  $\mu\text{m}$  is probably due to the mechanical delamination between the core and the cladding.



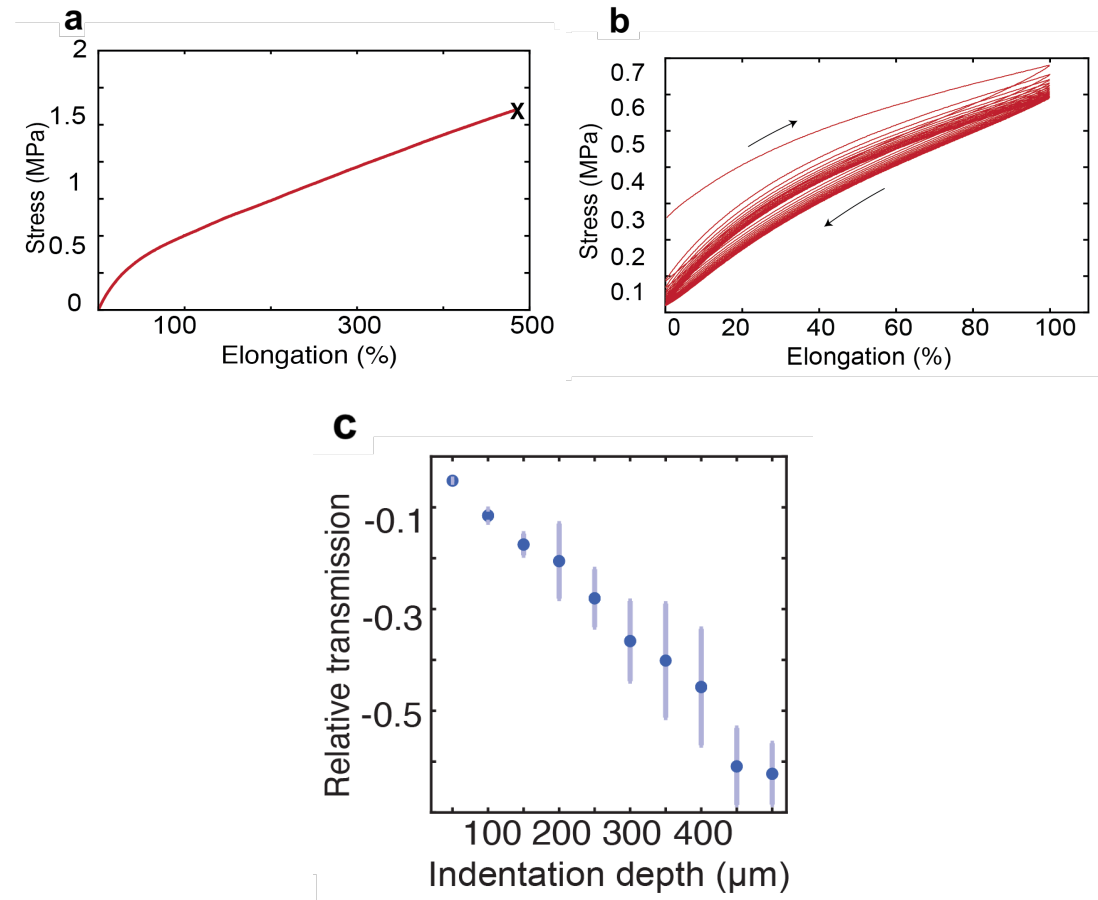


Figure 2.5 – a) Tensile test of the fiber until the mechanical failure b) Dynamic tensile test of a fiber stretched between 0 and 100% multiple times. c) Relative losses of the light transmitted versus the indentation depth in a 1 mm diameter fiber.

## 2.5 Strain sensing

After observing the mechanical and optical properties of the fiber, we investigated how the light transmission is influenced by the deformation of the fiber. We first observed the transmission of light while stretching the fiber at 100%. We observe in Figure 2.6.a that the central part of the curve can be approximated with a linear response and the transmission decay correlates univocally with the stretch percentage.

We stretched the optical fiber up to 1000 cycles and recorded the correlation between the stretch percentage and the light intensity. We observed that the transmission,

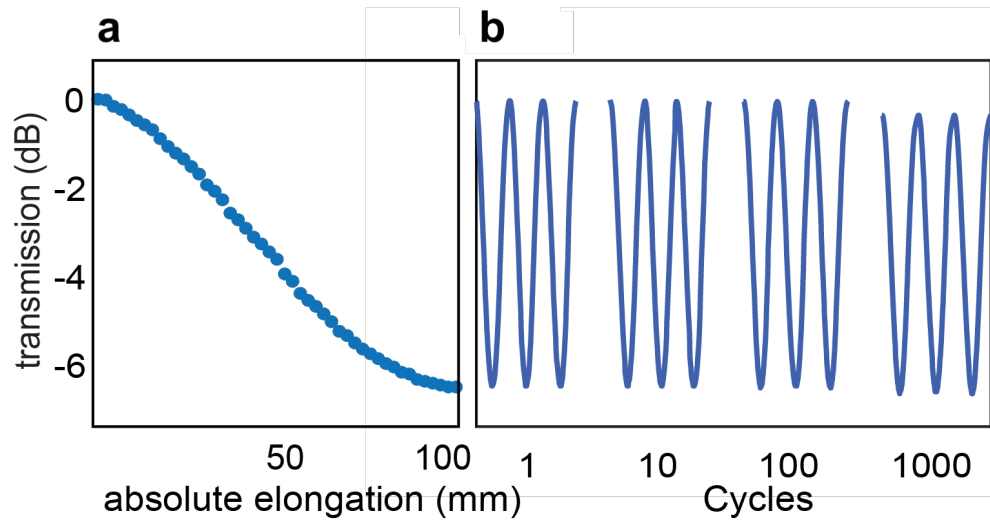


Figure 2.6 – a, Relative light transmission of a single core fiber while stretched and (b) cycled at 100% elongation.

which is consistent between different cycles, starts to decrease only when it reaches 1000 cycles. These features, combined with the mechanical features observed in Figures 2.5.a and 2.5.b, prove this fiber to be the a good candidate for a platform for highly stretchable sensors.

The optomechanical performances of the fiber discussed above allowed us to design a device for an application requiring extreme stretch sensing. We developed a prototype system that could be used to correlate extension and force for superelastic gym bands. These bands are used for training in many disciplines and physiotherapy protocols, but, as the force varies with elongation, it is impossible to predict the actual extension required to exercise a given amount of force.

We connected a 654 nm LED to one end of a 10 cm stretchable optical fiber and a photodiode to the other end, both mounted on clips that can be firmly attached to the elastic band. The intensity of the transmitted light was recorded and processed by a custom electrical circuit and microcontroller. In order to correlate the strain applied to the band and its elongation, we tested it in a tensile strain test machine: the stretch

and applied force were recorded simultaneously and plotted together. Figure 2.7.a shows the results obtained; as the force recorded grows with elongation, the intensity transmitted decreases. They both appear in the linear regime. Once the correlation between stretch of the band and light intensity transmitted is characterized (figure 2.7.c), the device is put in use: the light intensity is collected by a circuit that lights up different LEDs depending on the intensity of the force applied (Figure 2.7.b). The user can therefore know the pressure applied to the band just by looking at the number of LEDs that are illuminated.

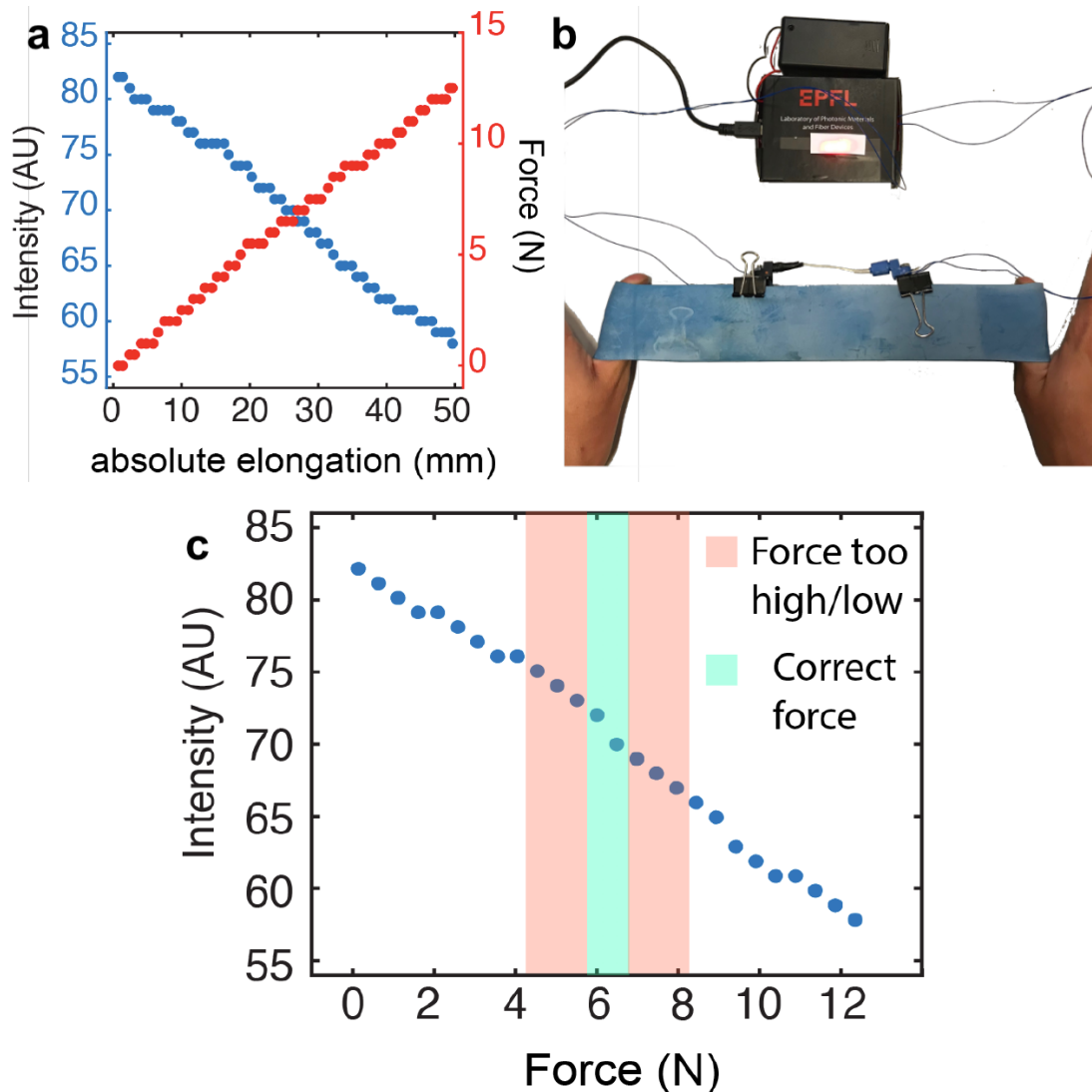


Figure 2.7 – a) Light intensity dependence (blue) and force dependence (red) versus absolute elongation of a single core fiber. b) The stretch sensing device, composed of an optical fiber with LED source at one end and photodiode at the opposite end, is clipped to an elastic band. The signal is analyzed by the Arduino in the black box and the force applied is assessed by the number of LEDs that turn on the box. c) Transmitted light intensity versus force applied on the elastic band. The orange regions highlight the points where the force is too low (one LED illuminated out of three) and too high (all three LEDs illuminated). The green region represents the adequate amount of applied force (2 LEDs).



## **3 Soft 1D Photonic crystal fiber**

In this chapter, the design, fabrication via thermal drawing and characterization of a soft 1D photonic crystal fiber with bandgap in the visible spectrum are presented and discussed. The first part will introduce the mathematical models used, the materials chosen and the expected design of the fiber, the fabrication part will go through and evaluate the process of trial and error used to obtain a drawable preform, while in the last part we will discuss the performances of the obtained fiber. The fabrication of such fibers would constitute a double achievement, from a materials engineering and processing point of view. In order to obtain optical features in the visible or NIR, we will need to make a multi-material elastomeric structure with 100-nm feature size, with an extreme aspect ratio, a prouesse in advanced manufacturing never demonstrated before.

### **3.1 Theoretical introduction**

Photonic crystals are ordered periodic structures of dielectric materials with different refractive indices that, when ordered in a particular fashion, they can interact with

photons in a similar way that lattices interact with electrons in solids[68]. In case the energy band structure has forbidden energy ranges, called band-gaps, all the light with a wavelength that corresponds to the forbidden energy can't propagate and consequently gets reflected. When this energy band-gap corresponds to a range of wavelengths in the visible range, a photonic crystal illuminated under white light will reflect just the color corresponding to the forbidden energy. This results in all the structural colors that we can observe in nature, from the blue wings of butterflies to the bright green feathers of a peacock.

This property has been used as well to confine light in the core of a fiber and transmit it over long distances: photonic crystal fibers can confine light in a hollow core and transmit it as information or energy for therapeutics over long distances[66]. As the EM waves don't enter the cladding, high intensity light, like CO<sub>2</sub> lasers, can be transmitted in photonic crystal fiber without degrading the fiber material [69]. Periodicity in photonic crystals can occur in 1, 2 or 3 dimensions: in this chapter we will discuss a photonic crystal fiber based on a photonic crystal with periodicity in only one dimension, commonly also called Bragg mirrors, because of their reflection properties. They are structured as a stack of alternating films of 2 different materials with different refractive indices. The optical properties of a Bragg mirror can be described as a reiterated thin layer constructive interference. The condition for constructive interference of a light that gets reflected from a thin film is [68]:

$$2nd \cos \theta = (i - \frac{1}{2})\lambda \quad (3.1)$$

where  $n$  is the refractive index of the material,  $d$  the thickness of the layer,  $\theta$  the angle of incidence,  $i$  an integer number and  $\lambda$  the wavelength of the incident light. The  $\frac{1}{2}$  comes from the fact that when light is reflected on the surface of a material with

higher refractive index, a  $\pi$  shift occurs. This equation is valid for unpolarized light and doesn't take in account the multiple reflections that can occur in the film. We need therefore to define the phase shift of an incident light ray as

$$\delta = \frac{2\pi}{\lambda} 2nd \cos \theta \quad (3.2)$$

and, generalizing for rays that occur to reflect  $m$  times in the thin film:

$$\delta_m = (m + 1) \frac{2\pi}{\lambda} 2nd \cos \theta \quad (3.3)$$

We want now to describe the reflection of a multilayer made of two alternating materials of respective thickness  $d_1$  and  $d_2$  and refractive index  $n_1 > n_2$ , enclosed between a medium with index  $n_o$  on top and a substrate medium with index  $n_s$ . We can easily derive a relation similar to equation 3.2 but generalized for a multistack of bi-layers, hence a Bragg mirror:

$$2d_j \sqrt{n_j^2 - n_0^2 \sin^2 \theta_0} = (i - \frac{1}{2})\lambda \quad (3.4)$$

where  $j$  is the considered layer.

Now that we have an analytical description of the behaviour of a Bragg mirror, we need to select and implement a computational method to describe the optical behavior of a generic film stack made of alternating layers.

### 3.1.1 Computational methods for film stack reflectivity

In order to optimize the design the fiber, we need a mathematical model that could simulate the optical response of a thin film stack. The most common models used for



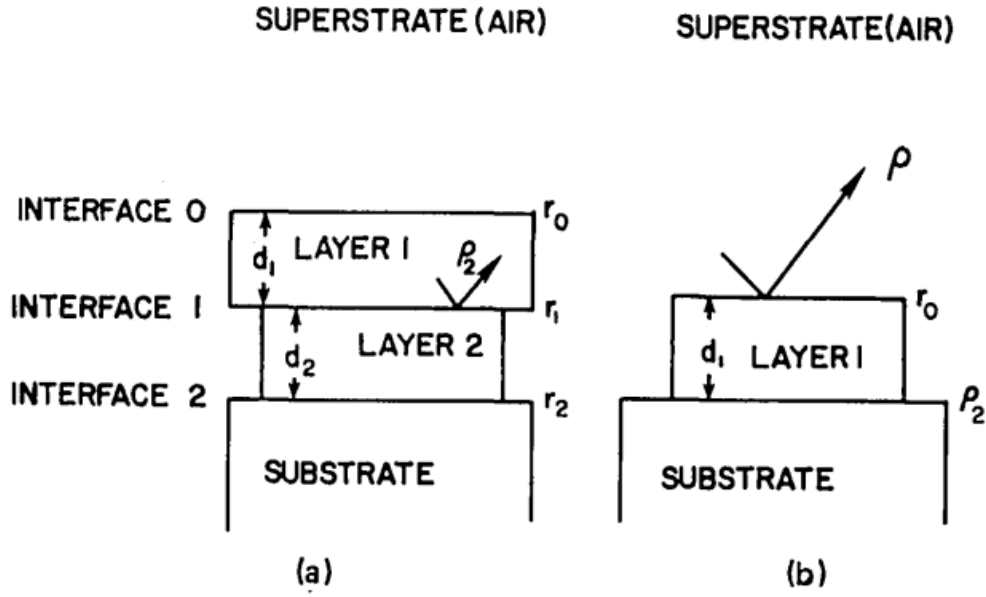


Figure 3.1 – a) Double layer on a substrate with thicknesses  $d_1$  and  $d_2$ , interfaces  $r_0$ ,  $r_1$  and  $r_2$  and the complex reflectivity of layer 2 as  $\rho_2$ .

b) The same two layer stack with the second layer replaced by the effective complex reflectivity.  $\rho$  is the effective complex reflectivity of the whole stack.[70]

this are the transfer matrix method and the Rouard's technique. The transfer matrix method, starting from the Fresnel coefficients, relies on the continuity of EM fields, derived from Maxwell equations, and assigns every layer of the stack a matrix that describes, given the field at the beginning of the layer, the fields at the end of the same layer. Transmission and reflection coefficients of multilayer stack can be therefore calculated from a matrix system.

For simplicity of coding, we decided to use Rouard's technique: it is a recursive technique that is based on substituting a thin film in the stack with a single interface with the same effective complex reflectivity. When Rouard's technique is applied to a thin film stack, it starts with taking in account the first bottom layer of the stack, compute the effective complex reflectivity, substitute it to the layer itself and recursively do the same for the adjacent bottom layer until all the stack is described with just one

effective complex reflectivity value, that takes in account reflection coefficient, polarisation and phase shifts of the whole stack. We can formalize the technique for the simplest case: a double layer stack on a substrate (figure 3.1). As said before, the first step is to compute the effective complex reflectivity of the first stack, computed as:

$$\rho_2 = \frac{r_1 + r_2 e^{-2i\delta_2}}{1 + r_1 r_2 e^{-2i\delta_2}} \quad (3.5)$$

Where  $\delta_2$  is the phase shift of a thin film described in equation 3.2,  $r_1$  and  $r_2$  are the reflectivity values obtained from the appropriate Fresnel coefficients. We can now move to layer 1, as we have reduced the optical properties of layer 2 as those of an interface. We therefore compute, in a similar way, the complex effective reflectivity of total stack  $\rho$ , substituting the actual  $r_1$  values with the effective reflectivity of the whole stack beneath it  $\rho_1$ .

$$\rho = \frac{r_o + \rho_2 e^{-2i\delta_1}}{1 + r_o \rho_2 e^{-2i\delta_1}} \quad (3.6)$$

where  $\delta_1$  in this case is the phase shift occurring from layer 1. We then write a simple script to compute the reflectivity of any given multilayer stack given the angle of incidence, the thickness of the layers and their refractive index. As the complex reflectivity holds the information about the two polarization modes, we can obtain the absolute reflectivity of both parallel (figure 3.2.a.1) and perpendicular (figure 3.2.a.2) polarization. A higher number of layers would results in a stronger reflection, as the final properties are a cumulative effect of every double stack of films. A higher refractive index difference would not only increase the reflectivity but it would increase the range of forbidden wavelengths composing the bandgap. As shown in figure 3.2.b, the reflectivity of the same Bragg stack can result in different peak positions depending

on the angle of incidence: this depends on different optical paths traveled by light rays entering at different angles.

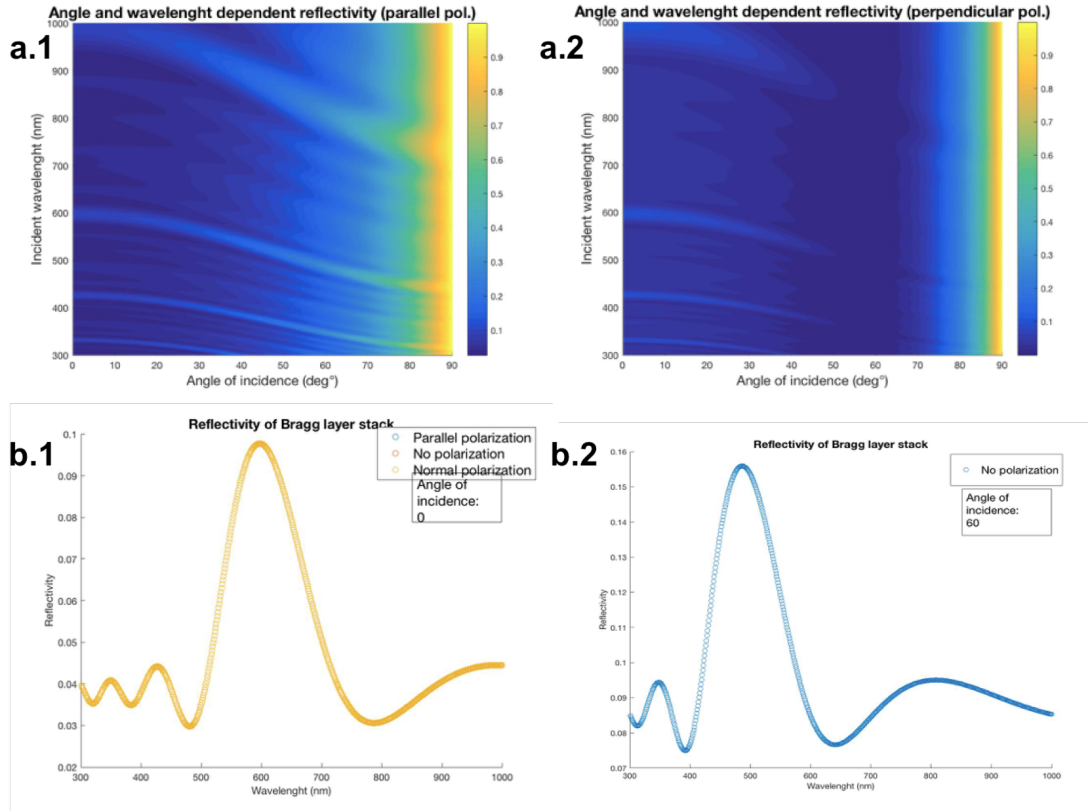


Figure 3.2 – a) The two graphs display the reflectivity of a multilayer stack, in this case a Bragg mirror made of 3 doublestacks with thickness of each layer of 200 nm and refractive index of 1.52 and 1.41, for parallel (1) and perpendicular (2) polarisation. The x axis displays all the possible incident angles while the y axis the wavelength of the incident light. The colorbar defines the reflectivity value. b) Reflectivity plot for a Bragg stack at AOI=0 (1) and AOI=60 (2).

### 3.1.2 Computational methods for chromaticity determination

As already discussed, one main characteristic of Bandgap fibers and photonic crystals in general is the eventuality of displaying a structural color. This occurs when a bandgap, that could be fundamental or of higher order, exists for wavelengths in the visible range. Color, unlike other physical parameters, can't be quantified directly but

depends on how the human eye perceives it. The human eye perceives color with three different cone cells, and has peaks of sensitivity in short (420-440 nm) medium (530-540) and long (560-580) wavelengths. The quantitative description of color has therefore always been a difficult and has evolved over time. Already in ancient times, the trade of gemstones required a way to categorize the different colors to assess their value, but the biggest advancement of color theory has come about with the development of color displays: technicians and programmers, forced to find a universal code to transmit and display color, developed many frameworks and tools to effectively do it.

A color can be described as a combination of the 3 primary spectral colors red, green and blue (RGB color model), or by its hue, saturation and brightness/lightness (HSB/HSL models). For our work, we decided to characterize structural colors using the CIE 1931 chromaticity diagram[71]. It was created by the International Commission on illumination and tries to evaluate a color as closely as possible to how the human eye would do it. Through multiple testing on different patients, they defined three functions  $\bar{X}(\lambda)$ ,  $\bar{Y}(\lambda)$  and  $\bar{Z}(\lambda)$  that could match human eye cones response to perceived colors. Every color can be identified by three values (XYZ), that can be seen as the three values of overlap of the functions discussed before with a given spectrum in the visible.

In our case we will focus only on the hue and saturation of the color. Brightness depends mostly on the illumination settings and doesn't give clear information of the quality of the color displayed. This will allow us to work with only two variables (xy) that can be obtained by the three variables described before via normalisation and to work on the chromaticity diagram displayed in figure 3.3.c.

We wrote a code that could assign a xy pair of CIE coordinates to any spectrum  $P(\lambda)$  used as input. The input spectrum is normalized, then the coordinates X, Y and Z are

computed as:

$$X = \int P(\lambda) \bar{X}(\lambda) d\lambda \quad Y = \int P(\lambda) \bar{Y}(\lambda) d\lambda \quad Z = \int P(\lambda) \bar{Z}(\lambda) d\lambda \quad (3.7)$$

and then normalized as

$$x = \frac{X}{X + Y + Z} \quad y = \frac{Y}{X + Y + Z} \quad z = \frac{Z}{X + Y + Z} = 1 - x - y \quad (3.8)$$

For computational simplicity, the exact CIE chromaticity functions are substituted by their Gaussian approximations from the work of Wyman et al. [72]

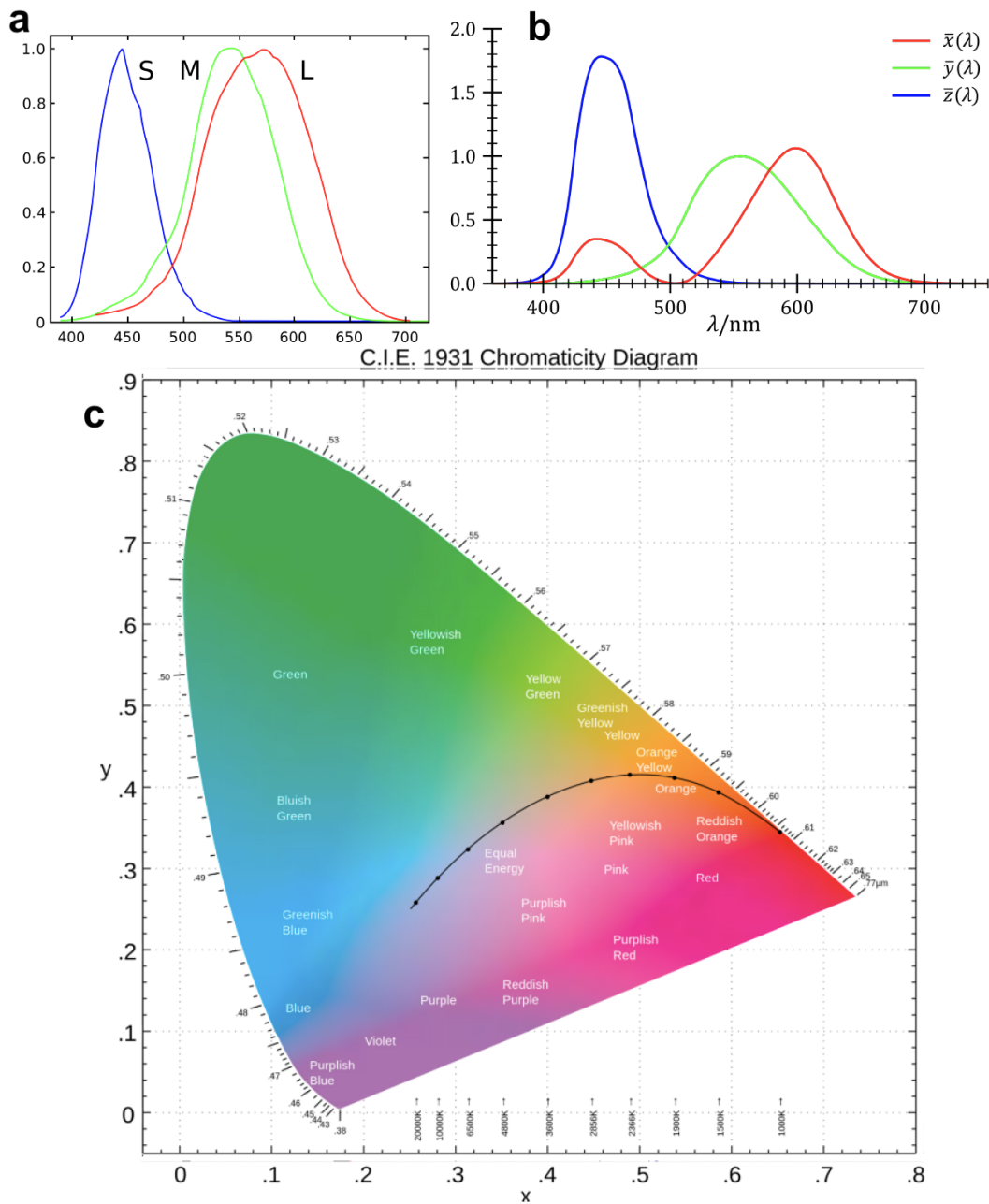


Figure 3.3 – a) The sensitivity spectra of the human cone cells for short (blue), middle (green) and long (red) wavelengths. b) The chromaticity functions  $\bar{X}(\lambda)$ ,  $\bar{Y}(\lambda)$  and  $\bar{Z}(\lambda)$ , clearly recalling the sensitivity spectra of the human eye. c) The Chromaticity diagram displaying all the possible colors that can be described. The black line in the center shows the black body color trajectory and their temperatures. [72]

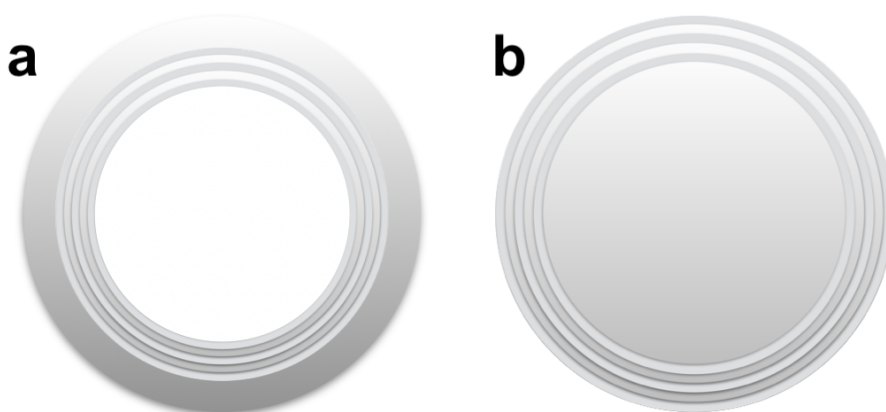


Figure 3.4 – Representation of the cross-sections of two design hypothesis for the stretchable photonic crystal fiber: a) A hollow core fiber with the multilayer stack deposited on the inside of the core. b) A solid core fiber with the photonic crystal deposited on the outside of the core.

## 3.2 Fabrication

In this section we discuss and explain all the steps we identified to fabricate a soft 1D photonic crystal fiber. We will start with the description of the fabrication of the preform core, then we'll evaluate the optimal film deposition technique to fabricate the multilayer stack among the ones we tried and we'll conclude with the optimal drawing steps to obtain a fiber.

### 3.2.1 Design and Material selection

In this part of the project, we aimed at the development and fabrication of two fiber designs, both already existing for fibers made of rigid materials, but never demonstrated for thermally drawn soft fibers. The objective is to identify clear fabrication steps that would lead to the production through thermal drawing of 1D photonic fibers, using stretchable elastomers as building blocks. The elastomeric feature would open to new properties and application possibilities while the scalability granted by

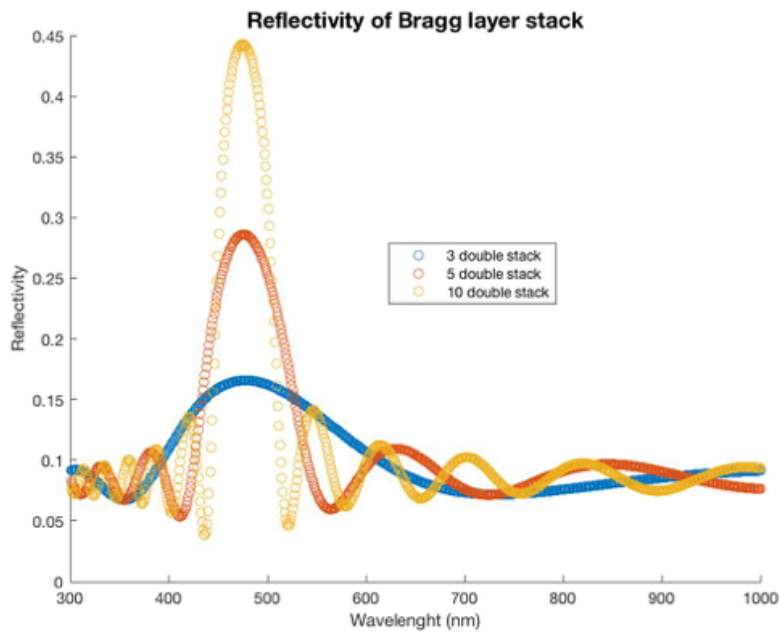


Figure 3.5 – Simulation of the reflectivity profile of Bragg multilayer mirrors, all made of transparent materials with refractive index  $n_1=1.41$   $n_2=1.52$ , but with a different number of layers deposited.

the thermal drawing technique would ensure large scale production for applications in textiles or requiring transport over long distances. Both of these fibers have to be designed with just two transparent elastomers with different refractive indices.

The first simpler design consisted in an elastomeric core, made of the polymer with higher index. Around it, as shown in figure 3.4.b, we want to position a high number of concentric alternating layers forming a Bragg mirror. This fiber would display strong structural color on the outside, and a stretching of the fiber would induce a blue shift of the bandgap frequency. Similar soft 1D fibers have been already fabricated, as largely discussed in the first chapter, but their fabrication processes were cumbersome and only allowed for the production of very short fibers, preventing any applications requiring long fiber lengths and low costs.

The second fiber design would consist in a hollow core stretchable photonic crystal



fiber (figure3.4.a). It would have the same design of a commercially available 1D photonic crystal fiber but completely made out of thermoplastic elastomers. This last feature would allow a tunability of the transmission band and modes, and the possibility of using for applications that require extreme softness and/or solicitations. The ultimate goal would be to use such advanced soft fibers to transmit light in the visible or infrared region, as such structure would avoid the detrimental effect of the high intrinsic light guiding losses in elastomers. Moreover, soft fibers with such a level of control down to tens-of-nanometer scale has never been reported in literature. The materials selected for the design of the Photonic bandgap fiber must match various requirements. In addition to the properties already discussed for the selected materials for step-index stretchable chapter, most of thin film deposition techniques require additional solubility properties. The high index polymer selected ( $n=1.52$ ) was Styrene Ethylene Butylene Styrene Block Copolymer, a block copolymer that was used as core in the stretchable step-index fibers. It is soluble in a wide range of organic solvents. The second polymer selected, as low refractive index polymer ( $n=1.42$ ) was Geniomer, a polydimethylsiloxane/urea copolymer. This polymer is soluble in chloroform, but doesn't dissolve in most of the less aggressive organic solvents. This asymmetry can be successfully used to deposit consecutive layers. As discussed in the previous chapter, these polymers have matching visco-elastic behaviour and can be drawn together. Their mechanical properties at room temperature are also similar, which should help to prevent delamination under stretching. On top of the optical properties already discussed, these two materials can be successfully dissolved in various organic solvents, fundamental property for thin film deposition.

We then needed to identify quantitatively the preform design required to obtain the

expected optical and mechanical properties of the fiber. We focused first on the fabrication of the first design proposed and we tried to adapt the techniques to obtain the second design discussed subsequently. Using the simulation tools described in the previous section, we first addressed the number of bi-layers that should be present around the core to obtain a good light reflection in the visible range. We run simulation as described above of multilayer stacks with different number of layers. We didn't follow strictly the  $\frac{\lambda}{4}$  rule, as we didn't expect to have a complete control on the film thicknesses, but we inserted an error of about 10% from the ideal thickness ratio of the two films. We run the simulation with films of thicknesses of about 80 nm that would result, taking in account the refractive index, in a resonance peak in the visible region, slightly shorter than 500 nm. The results obtained, in figure 3.5, clearly showed that around 10 bi-layers, therefore 20 films, are needed to obtain a reflectivity peak of 0.45. We set our initial reflectivity goal value around 0.5, as it would already give a reflection resulting in a clear color.

The core of the preform should have been cylindrical, as the thermal drawing process might induce disuniformities in the film thicknesses during the drawing process if the preform cross-section hasn't cylindrical symmetry. The preform diameter must be as large as possible in order to allow for a high draw-down ratio and reach the targeted thickness of the bilayers. Our furnace is however limited by an internal diameter of 3,5 cm. We started with preform cores of 2 cm in diameter and we moved up to 3 cm in the development of the project.

The length of the preform should be enough to enter a steady state drawing process but not too long, in order to be easily fabricated, to fit into ovens and to limit the required extension of the thin films. We decided to work with preforms of 10 cm in length.

To evaluate the maximum thickness that the films should have on the preform in

order to reflect in the visible after drawing we needed first to assess the maximum draw-down ratio achievable with preforms made of the elastomers we selected. From previous experiences, the maximum draw-down ratio achieved with elastomer-based preforms was around 50, with a feed velocity of 1 mm/min and a draw velocity of 2,5m/min. So as to obtain film thicknesses in the final fiber around 100 nm, we consequently need to deposit films of not more than  $5\mu m$  on the preform. If this minimum thickness can't be achieved, the preform can be drawn multiple times, allowing a higher draw-down ratio but increasing the incidence of mechanical failures and process-induced inhomogeneities.

### 3.2.2 Core fabrication

Every process starts with the polymers bought as pellets, so we need to identify the most suitable process to consolidate them into a cylindrical rod that will form the core of the preform. The first attempts were made distributing the pellets in a mould structured in 2 parts with a concave semi-cylindrical internal shape. A first portion of pellets was inserted in a semi-cylindrical mould that was then closed with a fitting metallic rectangular bar. The preform was then inserted in a vacuum hot press, first heated in order to melt the polymer and then a controlled amount of pressure of 0.5 Bar was exerted perpendicularly on the preform. The amount of polymer had to be finely tuned in order to obtain exactly a semi-cylinder. When the semi-cylinder was obtained, the same amount of pellets had to be added within another semi-cylindrical mould, and consolidated against the first one to obtain the desired polymer rod. This process held many intrinsic limitations: a small error in the amount of polymer in any of the steps would have resulted in a misshapen cross section, while the different heating time of the two sides of the preform could have led to different thermo-

mechanical behavior when drawn. Moreover, the surface roughness resulting from the interfaces of the different elements of the mould could have dramatically affected the uniformity of the film deposited on top. Due to these limitations, we designed a new cylindrical mould with a vertical piston that could press the pellet along the cylinder axis, avoiding all the limitations just discussed. In order to easily release the polymer cylinder after, the walls of the mould were covered with either a Teflon film, or coated with a release agent.

### 3.2.3 First generation fibers - casting and rolling

The deposition of thin films on the cylinder, in order to obtain a Bragg mirror around the core of the preform, has been achieved with various techniques during the development of the project. The first approach we decided to follow was the "cast and roll" technique. It consists in fabricating a double stack of films as large as possible and then roll it around the preform.

In the interest of having the two films fabricated on top of each other, we needed to identify two solvents with orthogonal solubility property with respect to the two elastomers. That way, when the second polymer film is deposited from a solution on top of the already deposited one, the latter will not be damaged. With this in mind, we identified two suitable solvents for the polymers. The low-index, silicone-based polymer, hardly soluble in any organic solvent, would be dissolved in Chloroform. The high-index tri-block copolymer was instead dissolved in Xylene, an organic solvent, less aggressive than Chloroform and hence not able to dissolve the low-index polymer. The first technique used to deposit the films and obtain the large-area bi-layer structure to be rolled was spin coating. However, the films obtained, while reaching the desired thicknesses of less than 5  $\mu\text{m}$ , could not reach the desired size and its

thickness uniformity was consistently poor and hard to improve.

We then turned to another technique that would allow us to fabricate films with much larger size: solution drop-casting. The process is extremely simple: on a flat Teflon surface, carefully oriented to be perfectly horizontal, the solution containing the polymer is gently poured and, after the evaporation of the solvent, a fine film of polymer is formed. The concentration of the solution is a key element, as the thickness of the resulting film will depend on it. A solution with too low concentration however will be characterized by low viscosity, favoring surface reflow during solvent evaporation which affects negatively film uniformity. To best balance these two effects, we found the best trade off conditions with a solution of Chloroform and a 1% mass of the low-index polymer. For the high index polymer, we chose Xylene as solvent and a polymer solution at 1,5% mass. The Solution with chloroform was cast first, while the solution with Xylene, not able to dissolve the low index polymer, was cast on top of the polymer film obtained after the evaporation of all the Chloroform. After multiple essays, the minimum thicknesses that could be reached for both films was around  $20\mu m$ . The film could be cast over a surface of 20x30 cm, but the regions where both film thicknesses were uniform were smaller, in the order of few squared centimeters. In order to spread the solution more evenly, we added a blading step. A metallic bar with a uniform and tunable distance from the surface was passed over the solution right after the casting process. This step helped spreading the solutions more uniformly and to obtain a double stack of films with uniform thicknesses that extended on a surface of 10 X 20 cm. A high-index polymer rod with a diameter of 2 centimeters was then rolled over the film that adhered to it and formed an alternating stack of films that counted up to 4 double stacks. As the film thicknesses were still around  $20\mu m$ , the draw-dawn ratio required to reach the expected thicknesses, around 200, had to be achieved in 2 successive drawing steps. The preform was drawn once with a relatively

low draw-down ratio (4-8), another cladding of few mm of low-index polymer was then added to the single-drawn fiber through rolling and another drawing process was performed, this time with higher drawing ratio (25-50).

### 3.2.4 second generation fibers - Dip coating

The fiber fabricated with the method described above held many intrinsic limitations: the minimum thickness achieved for the films deposited on the preform was still 4 times larger than the values of  $5\mu m$  or less that we decided to achieve, in order to fabricate the fiber with just one drawing step. The number of stacks deposited (3-4) was not enough to display a strong enough reflection in the visible, and even less so to reach good light transmission properties. Moreover, increasing the core to diameter of 3 cm to improve the stability of the drawing process would have reduced even more the number of double stacks that could be rolled around the fiber.

We introduced therefore a new technique to deposit the films directly on the preform core: dip coating. The dip coating process consists in immersing the preform core directly in a solution reservoir and extract it at a steady velocity. The solution distributes uniformly on the core, depositing a uniform polymer film after the solvent evaporation. We are now going to give a brief theoretical introduction to better understand the process.

When the substrate is extracted vertically from the liquid at velocity  $U_0$ , the liquid mechanically driven up by the substrate, delimited by the boundary layer  $\delta$ , is split in two: a part of the liquid streamlines, left of the stagnation point S in figure 3.6.a, remains mechanically adhered to the substrate while the outer layer, right of S, returns to the reservoir. In a steady state condition, the profile of the liquid doesn't change and the deposited film thickness is constant. Different mathematical models are used

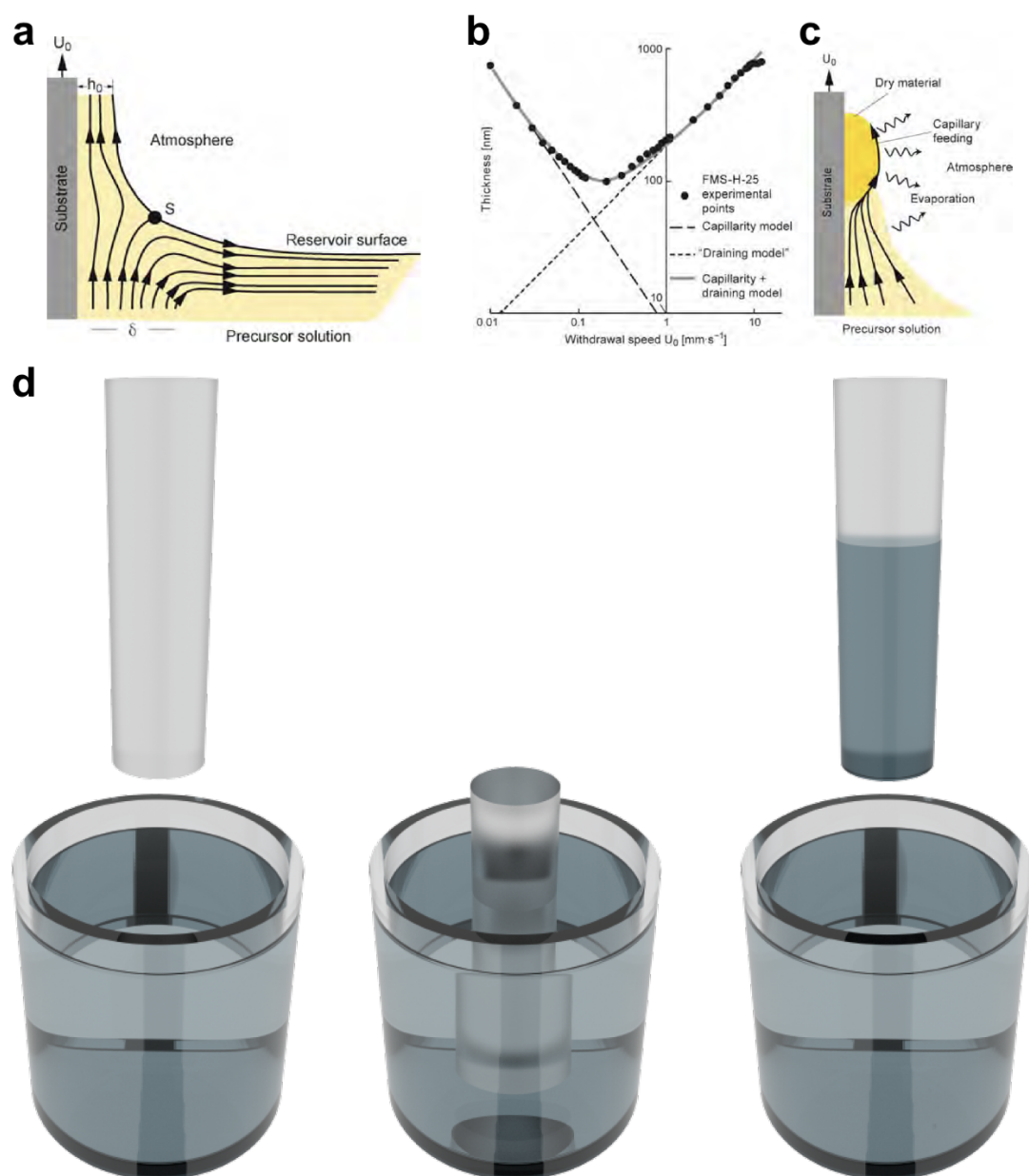


Figure 3.6 – a) Illustration of the streamlines in the solution when the substrate is withdrawn vertically. b) Film thickness vs withdrawal speed, clearly showing the two dip coating regimes. c) Illustration of the streamlines in the solution when the substrate is withdrawn vertically and in presence of strong capillary reflow.[73] b) Illustration of the different passages of the dip coating process.

to describe the dependence between the thickness of the liquid coating the substrate  $h_0$ , the withdrawal velocity  $U_0$  and the viscosity of the solution  $\eta_{tot}$ , depending on the viscosity of the solution and the withdrawal velocity. As shown in the graph of figure 3.6.b, in conditions of  $U_0$  and  $\eta_{tot}$  high enough, an increase of  $\eta_{tot}$  would lead to a similar increase of  $h_0$ . When the withdrawal velocity gets to small enough values, the capillary forces start playing a role and induce a vertical reflow of the solution on the substrate (figure 3.6.c). When this process becomes dominant, a decrease of  $U_0$  induces an increase in  $h_0$ . When  $U_0$  and  $\eta_{tot}$  are high enough, the thickness  $h_0$  is the result of the equilibrium between the viscous drag force, proportional to  $\mu h$  and the gravity force, proportional to  $gh$ , and can be expressed as [73]:

$$h_0 = c_1 \sqrt{\frac{\eta U_0}{\rho g}} \quad (3.9)$$

where  $\eta U_0$  is the viscous drag,  $\rho g$  the gravity force and  $c_1$  is has been shown to be 0.8 for Newtonian fluids, with experiments in different conditions of baths[74]. As we will work with withdrawal velocities of  $U_0 = 1 \text{ mm/s}$  and higher, we expect to be always working in this frame, therefore we are not discussing further the mathematical description of dip coating in conditions where the capillary reflow plays a role. As we will need to control the thickness  $h_x$  of the deposited polymer film, we will now discuss its dependence on the weight concentration of the polymer dissolved in the solvent, defined as  $C$ . We can define  $h_x = h_0 C$ , as the solvent and the polymer have similar density [75, 76]. Using equation 3.10, we obtain:

$$h_x = h_0 C = c_1 \sqrt{\frac{\eta_{tot} U_0}{\rho g}} C \quad (3.10)$$



From the fact that the viscosity of the polymer is orders of magnitude bigger than the one of the solvent, we can approximate  $\eta_{tot}$  as:

$$\eta_{tot} = \eta_{sol}(1 + \frac{\eta}{\eta_{sol}}C + ..) \approx \eta C \quad (3.11)$$

and we obtain:

$$h_x = h_0 C \approx c_1 \sqrt{\frac{\eta U_0}{\rho g}} C^{3/2} \quad (3.12)$$

We have now a proportionality relation between the film thickness  $h_x$  and the solution concentration  $C$ . We moved on to characterise the dip coating of the polymers selected before. We decided to use two different grades of low-index polymer, both drawable with the high index polymer, to increase our chances of success. The polymers were dissolved in Chloroform with different concentrations, between 2% and 5%.

After multiple trials, we decided to perform all the tests with the same withdrawal velocity  $U_0=1\text{mm/m}$ , for multiple reasons. First, with longer immersion times the chloroform tends to attack the polymers and diffuse inside it, resulting in bubbles in the preform after the degassing process. On the contrary, higher withdrawal velocities would have required less concentrated solutions, increasing the possibility of the solution to reflow on the substrate before evaporating and resulting in thickness dishomogenities of the film. We deposited multiple coatings for every concentration and every polymer, the results are shown in figure 3.7. The graphs on the left (3.7.a) are fitted with a polynomial curve  $h_x = aC^{3/2}$ , while the ones on the right are fitted with a generic curve  $h_x = aC^{3/2} + b$ . As we can observe, the dependence between  $h_x$  and the concentration  $C$  is better described by a polynomial dependence with an offsetting coefficient  $b$ . The offset could be explained by two factors: with lower densities, the

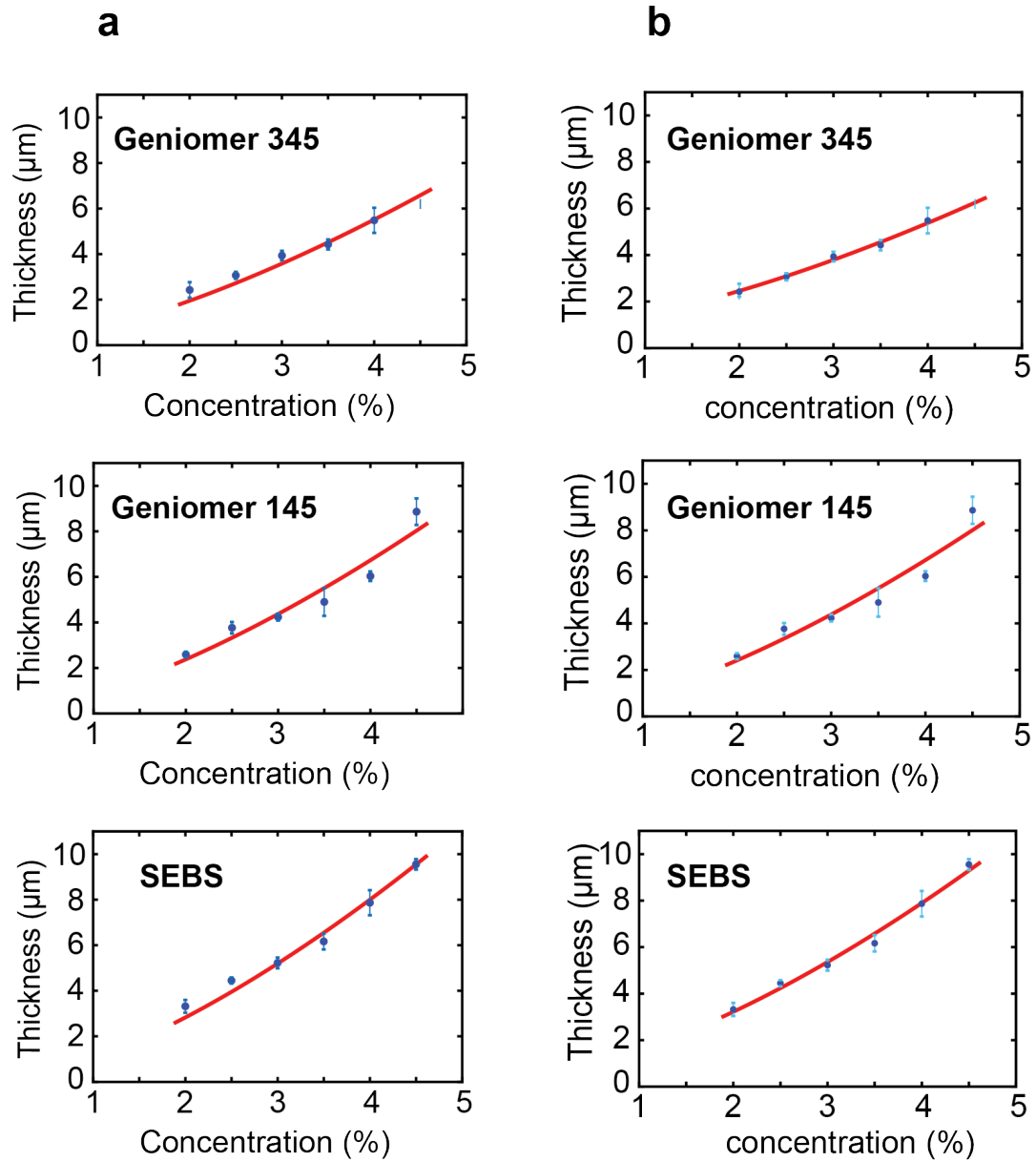


Figure 3.7 – Deposited thickness vs concentration in Chloroform for the three elastomers under investigation. The values are fitted by a) a polynomial curve  $h_x = aC^{3/2}$  and b) a generic curve  $h_x = aC^{3/2} + b$ .

viscosity of the solution might drop to the point that the capillary forces start playing a role and increasing the amount of solution deposited on the substrate, therefore the thickness of the resulting layer. Another explanation could come from the uneven distribution of polymer chains in the solution: as the polymers are slightly less dense (density  $\sim 1$ ) than the solvent Chloroform (density  $\sim 1.5$ ), the chains might tend to move to the surface, increasing the effective concentration of the surface layer that enters in contact with the substrate.

With the modeling of the dip coating process complete, we could fabricate our preform. The low-index polymer selected was the Geniomer 145, as it appeared to deposit more uniformly as a film. On a high index polymer rod of 3 cm in diameter, we deposited 20 alternating films using an automatic dip coating machine, in order to control the velocity and keep track of the number of cycles. The solution concentrations are 2.5 % for the low index polymer and 2% for the high index: the expected thicknesses were around  $3\mu m$  per layer deposited. The total process took a few hours, as Chloroform needed several minutes to evaporate at every coating step. After depositing all the films, the preform was left degasing in a room temperature oven for a few days, to make sure that every trace of solvent had evaporated. A cladding of low-index polymer was then added around the preform through rolling and consolidated in a vacuum for 4 hours at  $180^{\circ}C$ . The preform could now be drawn and on single drawing step is sufficient to scale fiber dimensions down enough to shift the bandgap of the Bragg mirror in the visible. Alternatively, the preform could be first drawn at low draw-dawn ratio, then the cladding was added by rolling a polymer film around it and the preform was drawn again: adding this steps helps drawing at much lower drawing ratios and, as a consequence, controlling the process better. Note that the process we have just described can also work to coat the inside walls of hollow polymer tubes, enabling the deposition of a Bragg mirror on the inside of a fiber.

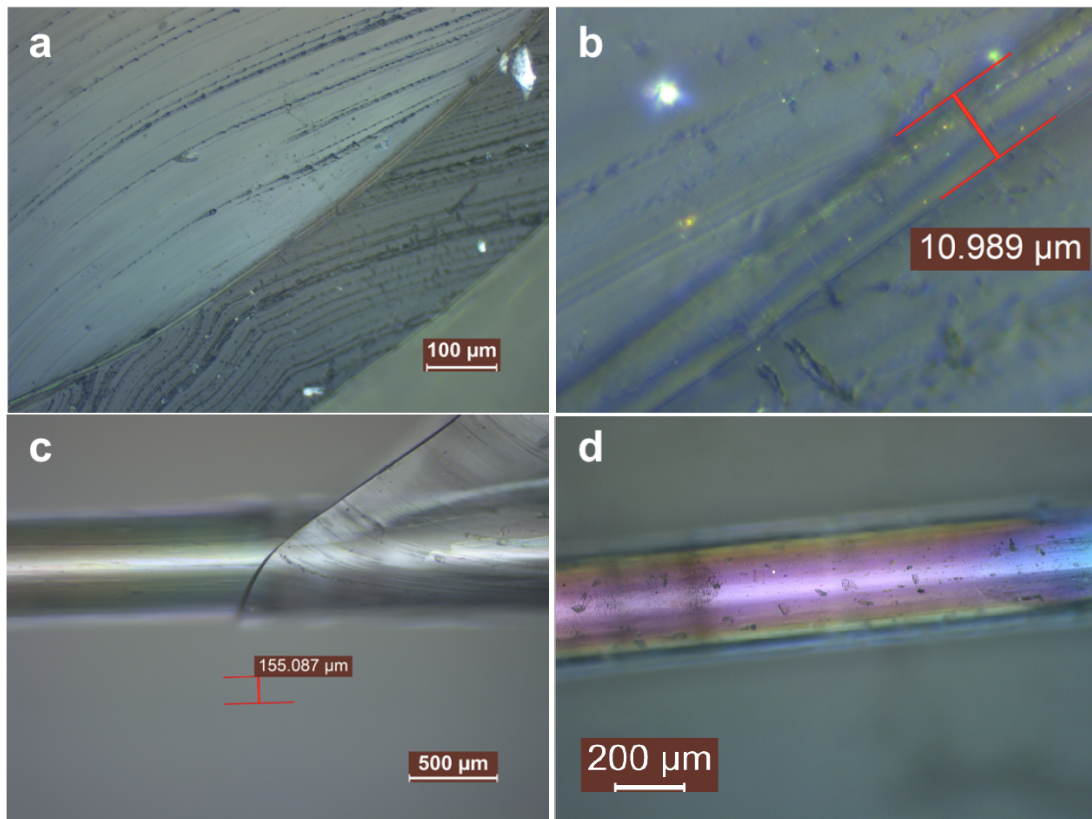


Figure 3.8 – a,b) Optical microscope images of the preform after one step of drawing with low draw-down ratio: the core, films and claddings are still visible. Optical microscope image of the fiber obtained, with no polarization filter (c) and polarization filter tuned to increase the fiber reflectivity (d).

### 3.3 Results

#### 3.3.1 First generation fibers - Casting and rolling

Multiple fibers were drawn from the preforms obtained via the rolling technique. With the optical microscope, we could verify if the film stack was still present after the first drawing steps, when the films were still observable with an optical microscope. As we can see in figure 3.8.a,b, the films are clearly visible between the high-index polymer core and the low-index polymer cladding. This result was encouraging, as

any multilayer stack of elastomers had ever been drawn to these dimensions. After the second drawing, the films became too thin to be observed with the microscope. Their fiber diameters ranged between  $200\mu m$  and  $500\mu m$ . As the core of the preform was 2 cm in diameter, the drawing ratio of the two drawing steps combined was between 40 and 100. This resulted in films between 500 and 200 nm. Given the simulation done before, these values were too large to obtain a 0 order bandgap in the visible spectrum, but we could hope to see a higher order bandgap, testifying the presence of the multilayer stack. The outer cladding was easily removable and, as confirmed later by SEM images, didn't delaminate the films of the Bragg stack. As shown in figure 3.8.c, a light color is easily recognizable on the fiber with exposed Bragg film. The color corresponds to a first order incomplete bandgap in the green region. The fundamental bandgap is therefore expected to be in the infrared region. The microscope picture in figure 3.8.d is taken with polarized filters. As discussed in section 1, certain polarizations increase dramatically the performance of the Bragg mirror, when the incidence angle is different from 0. We can clearly observe that a resonance in the visible is present and the color varies depending on the diameter of the fiber. With these encouraging first results, we moved on to the fabrication and the characterization of the fibers obtained by preforms fabricated through the dip coating process.

### 3.3.2 Second generation fibers - Dip coating

The fibers obtained by dip coating had been fabricated over a large period of time. Not only the deposition process itself, being not automatised yet, was time consuming, but the solution synthesis, double drawing and degassing steps made the whole process taking a big part of the project efforts. In figure 3.9.a the Bragg stack of polymer films

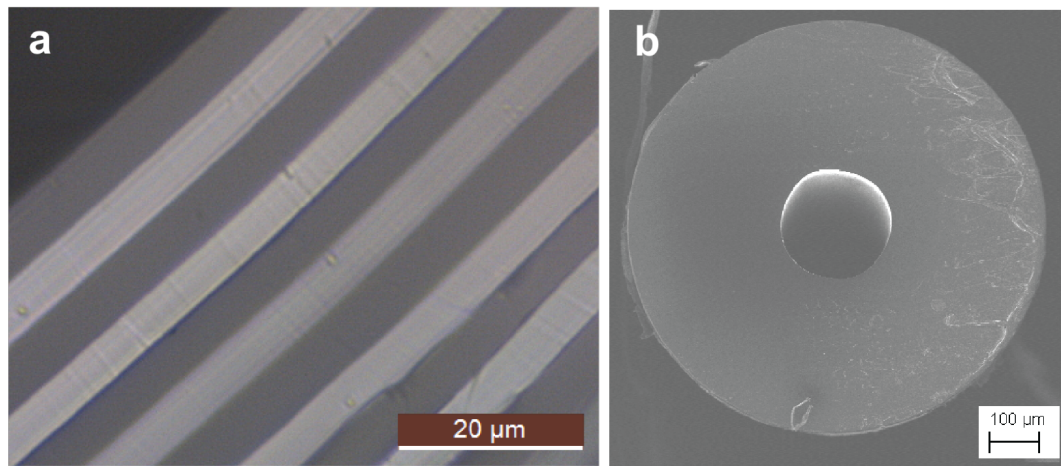


Figure 3.9 – a) Optical image of a stack of alternating films deposited with dip-coating. b) SEM image of the cross section of a fiber after drawing.

is shown before drawing, showing the results of the optimization process described before: the films are highly uniform in thickness and regular over the stack, their thickness of around  $4\mu m$  is in the order of what we were aiming at from the start of the project. The fibers obtained after thermal drawing showed a clear reflection in the visible, either under stretch when the bandgap had to be mechanically shifted from the near IR to the visible spectrum (figure 3.10.a), or at rest immediately after drawing (figure 3.10.b).

To investigate the fiber cross-section at such scales we turned to electron microscopy. The cladding was removed, then the fiber were frozen in liquid nitrogen and sectioned. The exposed cross section was then coated with Osmium and observed in the microscope. The cross section of a fiber can be observed in figure 3.9.b, while the multilayer stack deposited on the outside of the fiber is clearly visible in figure 3.11. As both polymers have similar electronic properties and are both coated with Osmium, The possibility of distinguishing the single layers wasn't guaranteed. Unexpectedly, one family of films, after the crio-cut, expands more than the other due to their difference

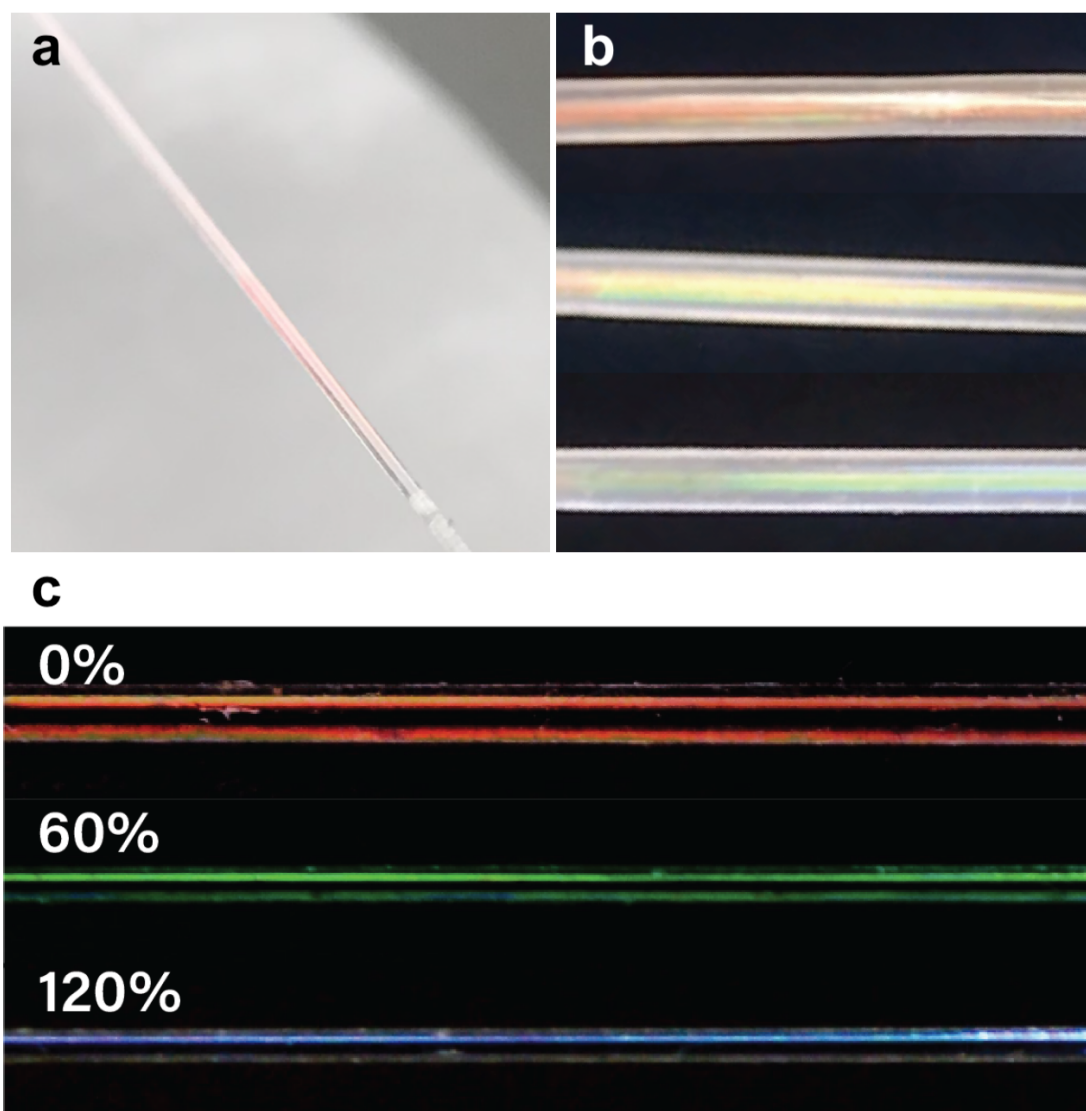


Figure 3.10 – a) Image of a fiber with main resonance in the IR that, under stretching and after the removal of its cladding, shows a bright red color. b) A fiber that shows different colors without removing its cladding. c) A fiber stripped of its cladding under different stretch conditions.

in thermal expansion coefficients. This allows to clearly distinguish the two different elastomers in the stack and evaluate their regularity and order. The films appear to have retained their order and relative thicknesses, allowing indeed the development of a strong structural color. In figure 3.12 we can observe the SEM images of a multilayer stack that was deposited inside the hollow channel of the preform. The films appear to have adhered to the inner surface and to have conserved their mechanical stability throughout the deposition process, the consolidation steps and the double drawing process.

Mechanical stretching clearly induced a reversible color shift in the fibers, as expected. We built a setup to characterize the shift with a bifurcated optical fiber, with a single tip on one end and a double on the other. The fibers composing the double end were jointed with a 50% beam splitter. White light was injected by one of the two ends of the bifurcation, guided to the single tip pointing perpendicularly on the fiber. The reflection was then collected by the same optical fiber tip and analyzed by a spectrometer connected to the second end of the bifurcation. The single tip of the fiber was connected to an XYZ stage in order to perfectly control the alignment and position of the fiber, as most of the light reflected by the photonic structure on the fiber was highly directional.

As shown in figure 3.13, the light resonance peak was clearly visible and easy to identify, even without source normalisation. The fiber was suspended by two clamps whose bases could move on a graduated rail. The color peak was recorded stretching the fiber at multiple relative elongations, from rest to 200%. In order to observe always the same portion of fiber, the stretching was induced by moving each clamp with the same amplitude on each side and observing always the central portion of the fiber. The spectra were normalized on the source, the light contribution reflected from the splitter subtracted and then fitted to obtain the exact position of the peak in the



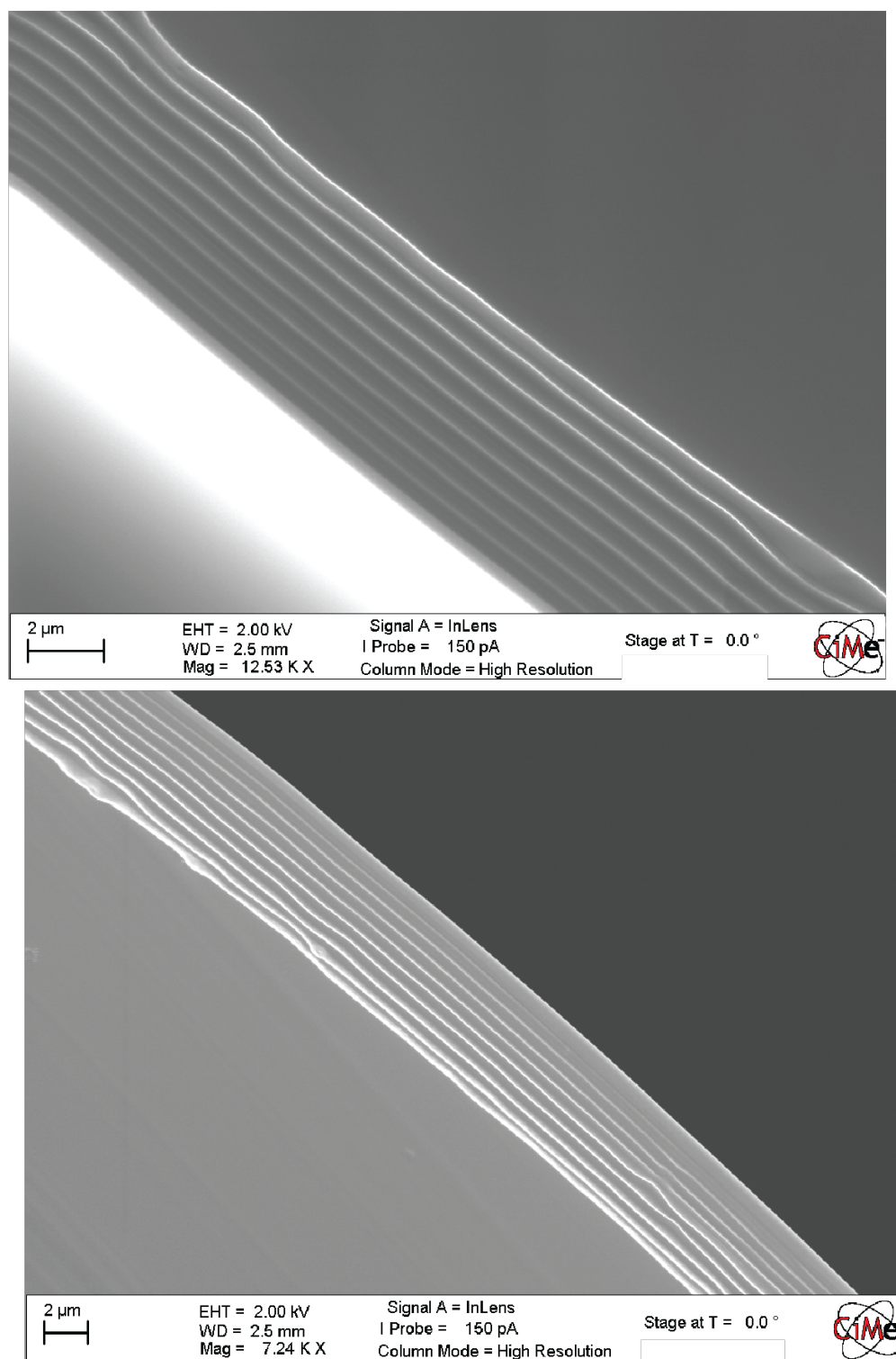


Figure 3.11 – SEM images of the multilayer stack deposited on the outside of a drawn fiber, after the removal of the cladding.

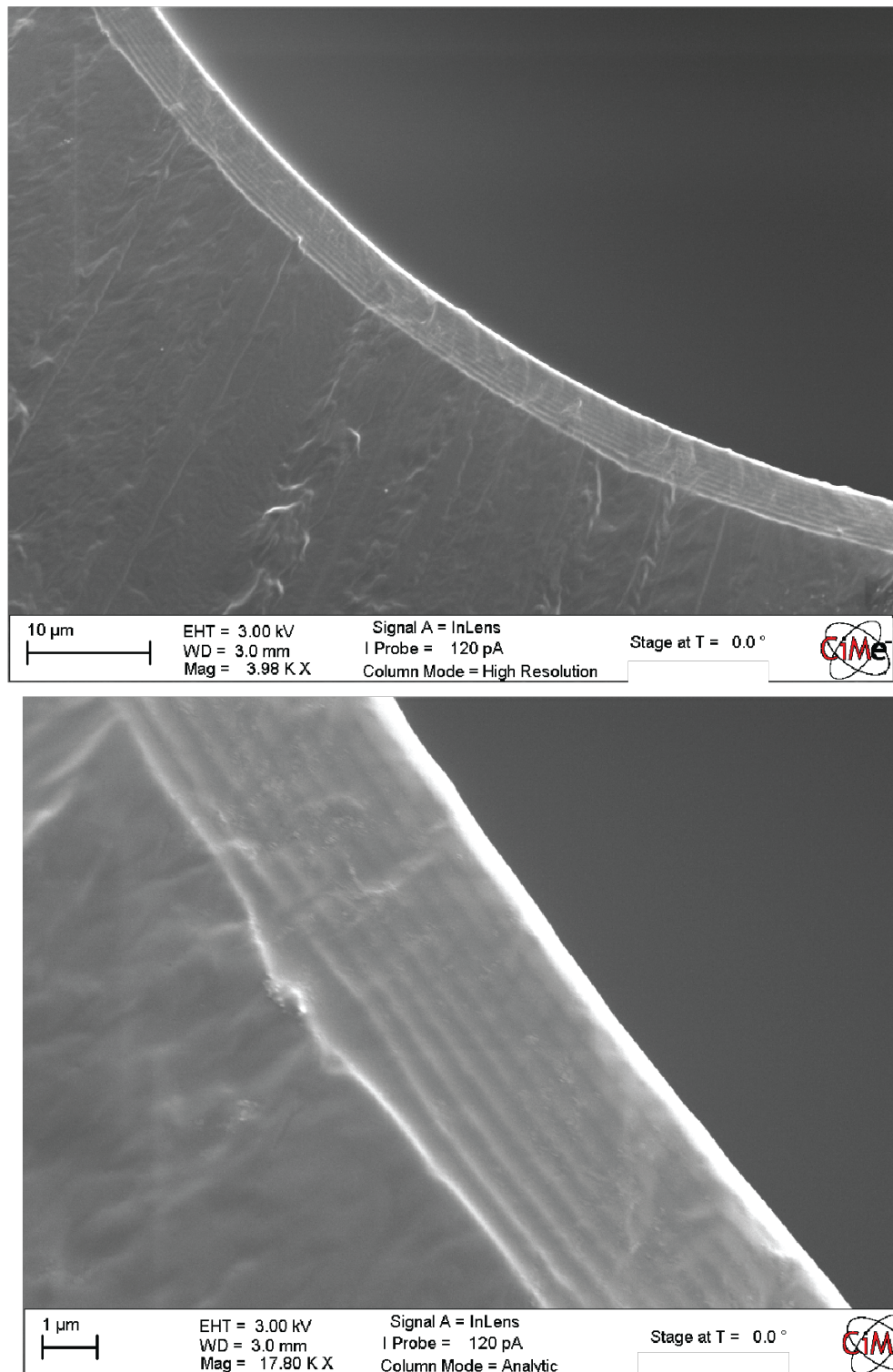


Figure 3.12 – SEM images of the multilayer stack deposited on the inside of a hollow core fiber, after drawing.

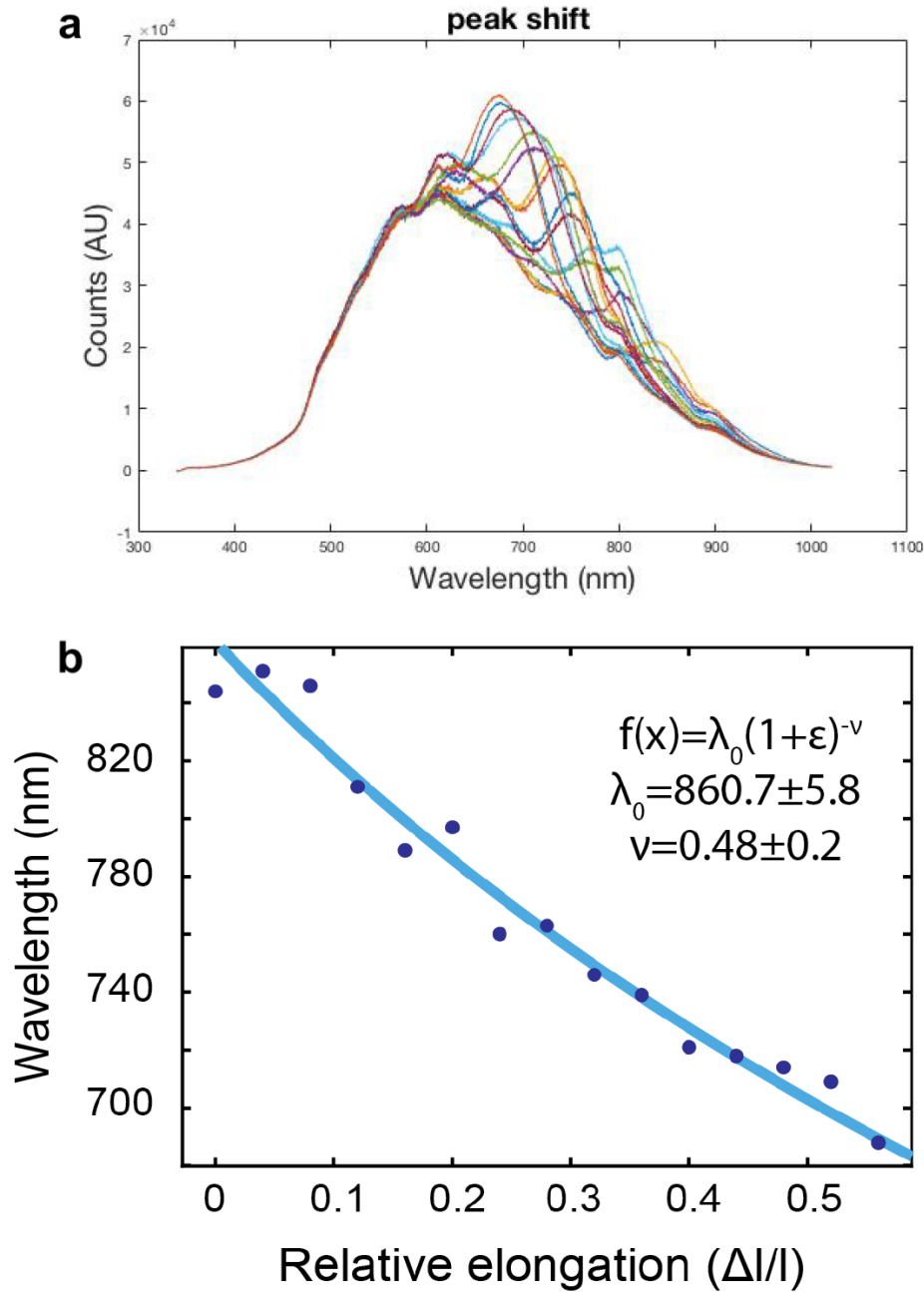


Figure 3.13 – a) The recorded reflection spectra of the same portion of a fiber under different stretch extensions, before any data processing. Although the presence of the strong internal reflection due to the beam splitter, not collected at the fiber tip, the resonance peak and its shift is clearly visible. b) The position of the maximum of the resonance peaks, calculated after data processing of the curves shown in the top graph, vs. the relative elongation that the fiber was undergoing. The fitting curve confirms the adherence of the results to the mechanical model proposed to quantify the shift of the color.

spectrum. The position of the peaks were then plotted with the relative elongation. The evolution of the thickness of the films under stretching can be easily modelled mathematically treating the fiber as an elastic cylindrical object under uniaxial strain. We know that the reflection peak of an ideal Bragg mirror is  $\lambda_m = \frac{4n_i t_i}{m}$ . Defining the Poisson ratio  $\nu$  as the negative true strain between the true strain  $\epsilon_t$  and the longitudinal strain  $\epsilon_l$   $\nu = -\frac{\epsilon_t}{\epsilon_l}$  and integrating the relation  $\frac{dt_i}{t_i} = -\nu \frac{dl}{l}$  from  $l_0$  and  $l_0 + \Delta l$  we obtain

$$t_i(\Delta l) = t_{i,0} \left(1 + \frac{\Delta l}{l_0}\right)^{-\nu} \quad (3.13)$$

Using the definition for engineering strain  $\epsilon = \frac{\Delta l}{l_0}$

$$\lambda(\epsilon) = \lambda_0 (1 + \epsilon)^{-\nu} \quad (3.14)$$

We fitted the data obtained with this model (figure 3.13.b) and we obtained the resonance wavelength at rest of  $\lambda_0 = 860.7 \pm 5.8$  and the Poisson ratio of  $0.48 \pm 0.2$ , in agreement with other results for similar elastic multilayers[77]

We then decided to investigate the uniformity of the Bragg stack from the shape of its resonance peak: a well ordered, uniformly deposited stack with the right thickness ratio would result in a sharp, symmetrical peak, while a multilayer Bragg stack with imperfections would display multiple and broader peaks. We could observe that, as shown in figure 3.14, along the fiber, different portions of the Bragg stack were giving very different resonating peaks, which indicates that the uniformity of the Bragg architectures requires optimization. Further investigation should prove if the imperfections appear during the drawing of the fiber or in a post-process manipulation. Nevertheless, the perceived color is quite uniform over some fiber portion, which

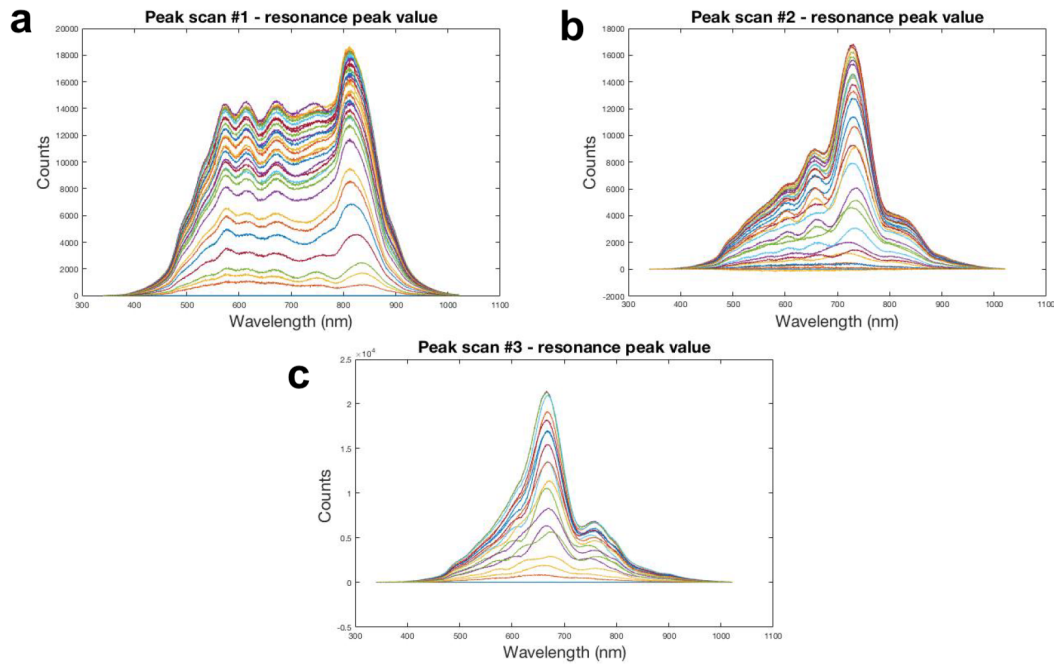


Figure 3.14 – The resonance peaks recorded from their appearance in the recorded spectrum to their disappearance. They were recorded by keeping the fiber tip always perpendicular to the suspended drawn fiber and moving the along the z axis.

demonstrates that with a simple and scalable process, we could fabricate a soft and stretchable photonic bandgap fibers with sub-100 nm feature sizes.

Finally, the feature of the fiber we were most interested in this part of the project was its structural color; we could quantitatively address its performance with the mathematical chromaticity tools introduced before. First of all, we could simulate the chromaticity values that we would have expected from a perfect Bragg mirror made of the same polymers used for the fibers and 10 double-layers. We simulated the reflection spectra in the visible for different film thicknesses, all with their bandgap resonance in the visible. We carefully selected a fiber whose resonance peak was symmetrical and its FWHM relatively low. We stretched it from the near IR to bluish green and recorded the spectra with shifts of around 25 nm. We then fed the spectra collected to the Matlab code described before and plotted the Chromaticity coordi-



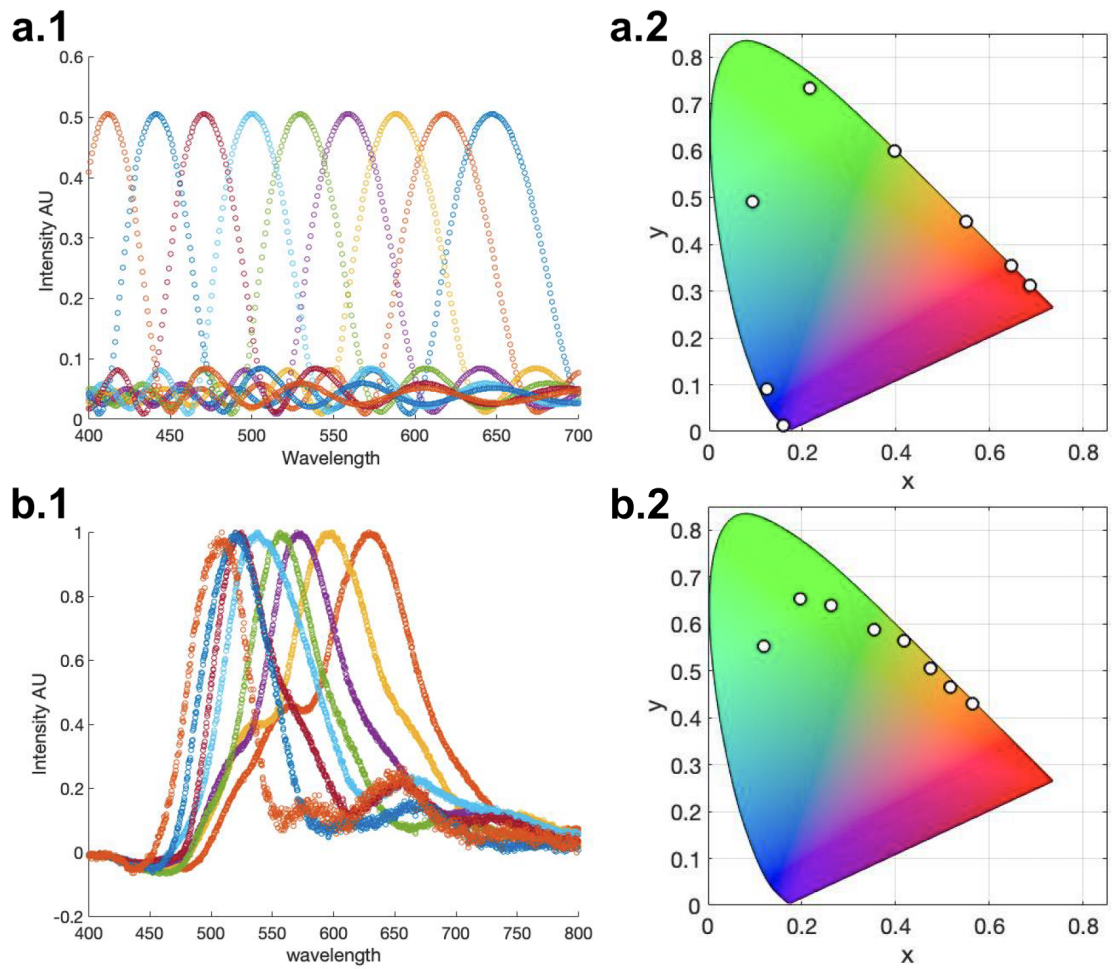


Figure 3.15 – a) The simulated resonance peak (1) and their position on the Chromaticity diagram (2). b) The resonance peaks measured experimentally (1) and their position on the diagram (2).

nates of the fiber under different conditions. We could clearly recognize a similar trend between the simulated color coordinates (figure 3.15.a) and the real ones(3.15.b). The perceived colors of the fiber follow indeed the same trajectory of the ones simulated from a perfect Bragg mirror. While the simulated colors stand on the edge of the diagram and are almost perfect spectral colors, the coordinates of the spectra collected from the real fiber are slightly closer to the center, where the color saturation is lower. This difference was expected and it's due to any imperfection in the film stack and thickness homogeneity, that distributes the resonance on a broader part of the spectrum and gives a less pure reflected color.

This last experiment proves that thermal drawing is a valid alternative to fabricate elastomeric bandgap fibers with resonance in the visible and is actually the only alternative that can assure a scalable and low-cost production of this kind of fibers ever reported.

## **4 Alternative architectures for stretchable optical fibers**

In this chapter we present projects that have been carried out during my PhD years that extend beyond step-index and Bragg fibers. All these projects have some fabrication steps, materials or techniques in common with the devices discussed before but they aim at fibers or devices with different architectures and novel properties. We will discuss three projects: a multicore step index fiber with multiple functionalities, the design and fabrication of a stretchable-liquid core step index fiber; and a fully stretchable, elastomer-based, 2D photonic crystal fiber.

### **4.1 Multicore stretchable optical fiber**

We presented, in the second chapter, the design and fabrication of a fully stretchable step-index fiber. we now introduce the fabrication, functionalization and possible applications of the same type of fiber, but holding multiple ordered cores in its cross-section. One major advantage of thermal drawing is the high degree of complexity that can be achieved within the cross-section of the fiber. As discussed already in the first chapter, most stretchable fibers are fabricated with methods that allow the fabrication



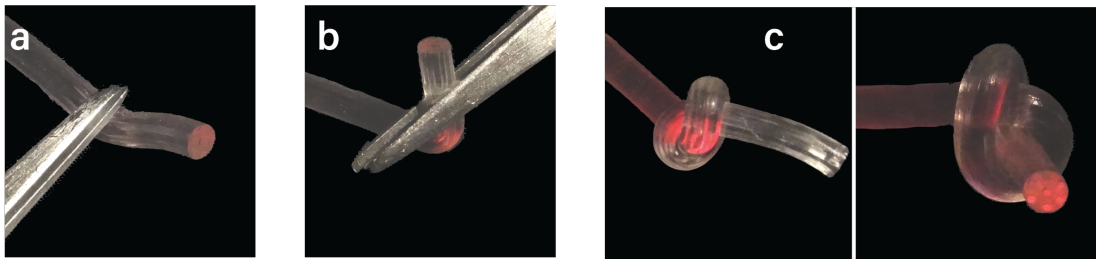


Figure 4.1 – A 7-core stretchable optical fiber is squeezed (a), bent (b) and shaped into a knot (c). Big deformations provoke, as expected, light leakage but don't prevent light to reach the tip of the fiber.

only of simple cross sections and often the cladding is added with post-processing. We show in figure 4.1 that, with our methods, we were able to fabricate fibers with different cores within the same cross-section. We fabricated a preform of low-index polymer with hollow channels, obtained putting metal cylinders in the mould. As the cylinders were thick enough (3 mm), they could be directly screwed to the base of the mould. We then inserted SEBS rods to fit perfectly in these channels and consolidated the preform. Following this procedure, we fabricated a fully stretchable multi-core step index fiber with a central core surrounded by 6 more cores, forming a centered hexagonal pattern. The fiber remains fully stretchable, as shown in fig. 4.1, under pressure, bending and tight knots. To illustrate one example of potentiality of such multi-core configurations, we show in figure 4.2 that the fiber can be used as a proximity sensor. The central core can be used to guide an optical signal, while the surrounding cores are connected to diodes and can collect the amount of light reflected by the objects in front of the fiber tip, giving information about their proximity. The graph in figure 4.2 shows experimental results of the proximity sensor: the amount of light collected by the external cores increases dramatically when the tip approaches a fiber, giving the probe a spatial sensibility of less than 1 mm.

This architecture allows the transmission and the recording of decoupled signals within the same fiber, allowing a spatial resolution that is beneficial for different appli-

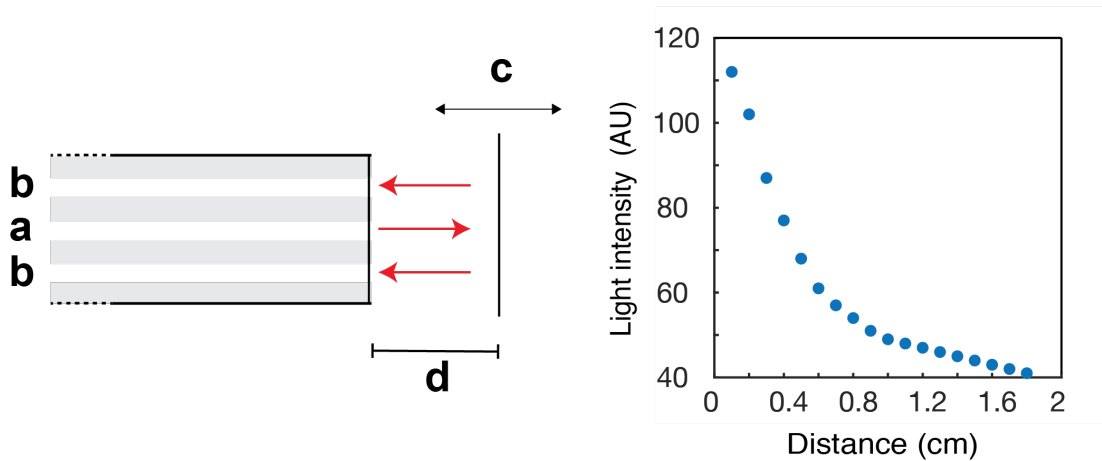


Figure 4.2 – The graph on the right displays the intensity of light collected collectively by the 3 external cores (b) after it was transmitted through the central core (a) and reflected by a flat object (c) versus the distance of the reflecting object (d).

cations. For example, in the optogenetic domain, spatially resolved neuronal activity recordings are performed in vivo with polymeric rigid multicore fibers[78]. The use of a soft multicore fiber would limit the disturbance on the neuronal tissue and prevent damages to the patient. Fibers can be drawn with a combination of hollow channels and optical cores, tailored for different applications. These kinds of fibers would be the ideal platform for in-situ optical polymerization in delicate positions, for example as an alternative of metallic coils used to fill in intracranial aneurysms, by injecting the polymer precursor and the light to activate photopolymerization [79].

Moreover, these fibers can be processed to become platforms for more advanced multifunctional devices. In figure 4.3 we show the first fully stretchable multi-purpose fiber probe, that combines one core that delivers light (in green), 3 cores that collect light (emitting red for display purposes) and three hollow: one for the insertion of wires or more sophisticated tools like manipulators or specimen collectors, one to insert or extract liquids. As the fibers are not in a bundle but geometrically organized, the light collection can give coherent spatial information. The probe is obtained starting from the 7 core optical fiber described above. Three of the cores are then

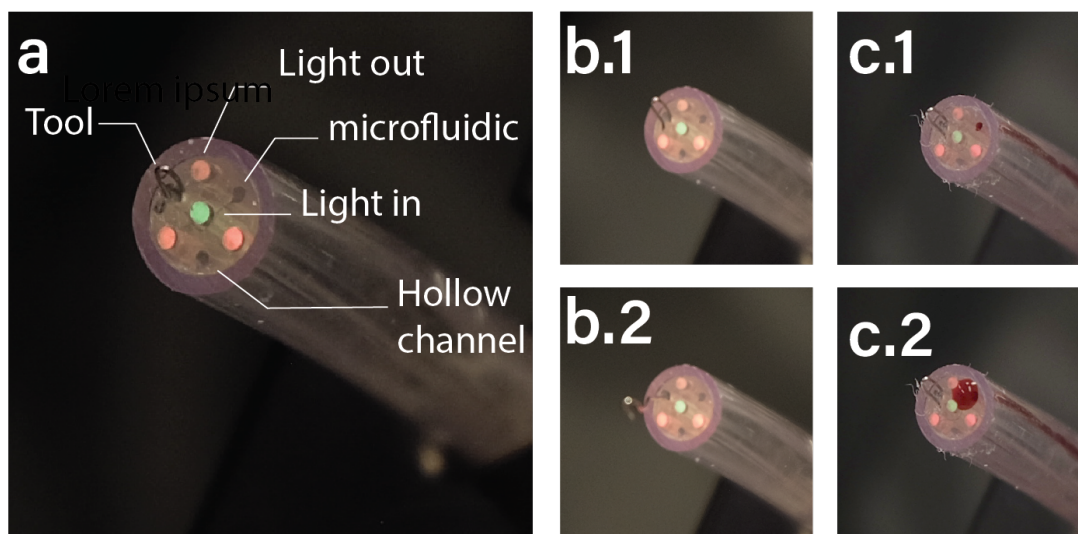


Figure 4.3 – a) Cross-section of the stretchable endoscope: the central core, entitled to guide light, is green while the cores devoted to collect light are transmitting red light. A metallic wire tool is inserted through the hollow channel devoted while the channels for liquid and gas are empty. b,1, 2) The metallic wire can be extracted from the fiber head and controlled to move and turn in different directions c), The Red liquid is inserted with a syringe in a hollow core and liquid easily travels the channel (1) and reaches the tip of the fiber (2)

extracted in order to obtain hollow channels. Red and green LEDs are then connected to the cores, a metallic wire with a twist is inserted in one hollow channel and the other channels is connected to a syringe. The fiber probe can perform all the tasks required from a similar instrument to operate, for example, as discussed above, proximity sensing collecting the intensity of the light reflected by an obstacle in proximity (fig.4.10a), liquid insertion or collection (fig.4.10c) and instrument insertion (fig 4.10b) remaining fully stretchable. These characteristics, usually found in regular endoscopes, allow the use of this kind of instrument where a larger, flexible yet harder endoscope would be more dangerous for the tissues around it in case of abrupt movement of the patient or misuse by the operator.

## 4.2 Liquid core Stretchable optical fiber

In the previous chapters of this elaborate we explored different designs and fabrication techniques to develop a new generation of optical fibers that could undergo extreme mechanical solicitations and stretching. While carrying out the project, we developed the idea of designing an optical fiber with a liquid core as a valid alternative to elastomers, inspired by the use of liquid metals in soft electronics. This feature would overcome many limitations coming with the use of elastomers as core or solid materials in general. First of all, a liquid core could reshape and readapt to even the strongest external solicitations: a given amount of pressure that would delaminate the elastomeric core from the cladding of the fiber, maybe inducing a mechanical failure of one of the components, would ideally just cause a temporary displacement of the liquid contained in the core. Moreover, a highly stretchable liquid core fiber would allow us to easily tune the diameter of the fiber. This would in turn allow us to better control the number of modes allowed to travel in the fiber and ideally have a fiber that could switch from multi-mode to single mode transmission under stretching. The mechanical properties would depend only on one material, the one forming the cladding, as the liquid would flow accordingly. This would simplify the fabrication process, the selection of the materials and the overall mechanical properties of the fiber. Our objective was to develop a process that would allow us to insert the liquid directly in the preform and then draw it.

We decided to start our trials using silicone oils as liquids, for multiple reasons. A silicon oil is any liquid made of siloxane polymerized with organic chains. This family of materials is known for their optical properties, both in terms of transmission and refractive index value spectrum: they are indeed widely used as index matching liquids in optical devices. They can be heated to high temperatures without degrading

or changing phase, as their chains are very stable, resulting in a wide use as thermal bath liquids. Another important feature of these materials is their range of viscosity: depending mostly on the length of their chains, these oils can have viscosity ranging over multiple orders of magnitude. They are readily available and their cost is low. Lastly, their toxicity for the human body is low and consequently they can be handled with few precaution steps.

We could pick a suited elastomer from one of the two we used in the projects previously discussed: Styrene Ethylene Butylene Styrene Block Copolymer, a block copolymer with refractive index of  $n=1.52$ , and Geniomer, a polydimethylsiloxane/urea copolymer with refractive index  $n=1.42$ . Although SEBS is more easy to process during the fabrication of the preform and in the drawing process, we had to select the polymer with the lower refractive index possible, Geniomer, because of the values of the index of the oils as explained below.

We first decided to test the possibility of drawing a preform with silicone oil inside and study the distribution and uniformity of the oil in the fiber. The Geniomer grade selected was the Geniomer 145 while as core oil we selected the Waker AK 60000 Siliconol, a methyl silicone oil with refractive index of  $n=1.41$  and viscosity of 50000 cP. We fabricated a hollow polymer preform in the shape of a tube with the same process described in the previous chapter, using Geniomer instead of SEBS as polymer. We then added a dye to the oil in order to improve its visibility after drawing and sealed the two ends of the preform. During the drawing process the oil remained inside the preform and didn't leak. We could observe with the optical microscope that the drawn fibers were homogeneous in thickness, their liquid core was still present and didn't collapse. The oil could be easily observed inside the core and appeared to be continuous for long portions of the fiber (15-20 cm). We managed to observe the uniformity of the distribution of the liquid for fibers down to  $15\ \mu m$  in diameter, but



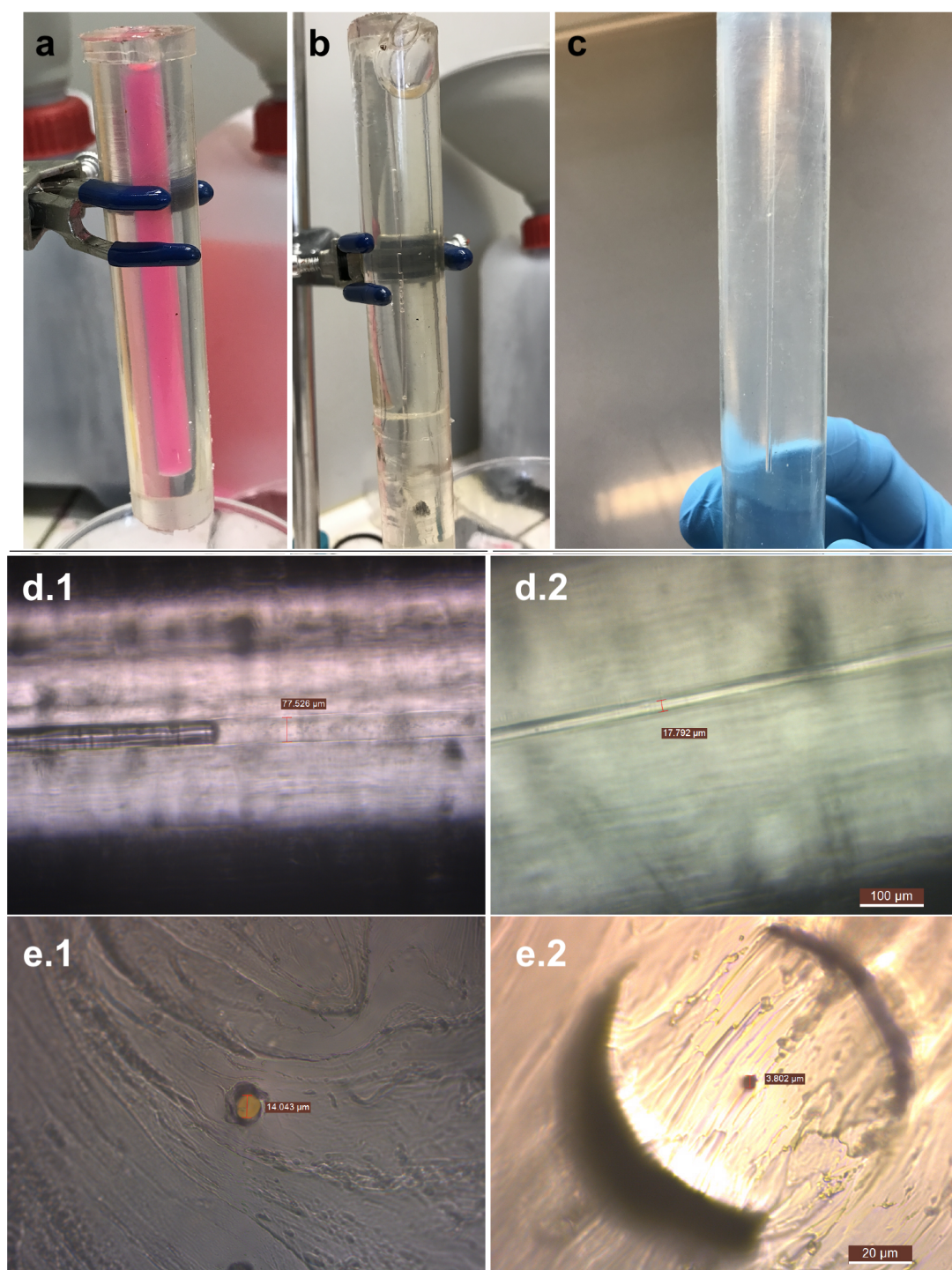


Figure 4.4 – a,b,c) Preforms with silicone oil in the core, ready to be drawn. d) Optical microscope image of the fiber after 1 (1) and 2 (2) drawing processes. e) optical image of the cross-section of two fibers, with core diameter down to 3.8  $\mu\text{m}$ .

we could prove, as shown in figure 4.4, that we could draw cores, through multistep drawing, smaller than  $5\mu m$ . These results put us in condition to aim at single mode transmission. As shown in figure 4.1.d.1, the contact angle between the liquid and the cladding polymer is relatively low, suggesting the affinity between the two materials: this would easily explicable by the fact that polydimethylsiloxane chains are the main component of both materials. We could therefore prove that Silicone oil could be drawn effectively into fibers from elastomeric preforms, remaining homogeneous and stable as core filler.

We then needed to address the optimization of the liquid core properties, in order to make it efficiently guide light. Although the silicon oil used presented optimal mechanical properties to be drawn as core in a fiber, its refractive index is slightly lower than the one of Geniomer ( $n_{oil} = 1.41$  while  $n_{cladding} = 1.42$ ) therefore light wouldn't be able to travel the core guided by total internal reflection mechanism.

To overcome these limitations, we identified the family of phenyl-methyl silicone oils to be a valid alternative. These silicone oils are made of chains that are similar to the polydimethylsiloxane chains present in the most known methyl silicone oils, but some methyl groups are substituted by phenyl groups. This change can increase the refractive index from  $n=1.42$  up to  $n=1.50$ . We obtained two different types of Phenylmethyl silicone fluids: The first one with refractive index of 1.42 and viscosity of 50 cP (PM-50 from now on) and the second one with refractive index of  $n=1.50$  (PM-125 from now on) and viscosity of 125 cP. In the case the three were perfectly miscible, we would have had a platform to tune both the refractive index and the viscosity of our core fluid. As first trial, we fabricated a fiber with the same architecture discussed before but we used as oil a commercial grade Phenylmethyl Silicone Fluid with refractive index of  $n=1.50$  and viscosity of 125 cP. Due to the fact that the viscosity is dramatically lower than the one of the oil previously used, we had to make sure the liquid wouldn't

have escaped the core due to gravity forces. we hence drew the fiber at different core diameters and we looked for the biggest core diameter at which the adhesion forces and capillarity forces would have dominated the gravity force. The biggest diameter at which the oil remained stable in the core even after exerting pressure and stretching on the fiber was around  $400\mu m$ . This means that in any fiber drawn with a core diameter smaller than this value the liquid was remaining inside the core also under manipulation.

We measured then the transmission of a fiber with core diameter of  $100\mu m$  via the cut-back technique and compared to the transmission of the similar fiber without liquid inside the core. The liquid was present uniformly inside the core and the two ends of the fiber were open. On both ends, after every cut, the first few mm of fiber core were empty. The losses due to imperfections and bad light coupling aren't expected to affect the result, as the cut-back technique measures the relative losses and evens out this kind of errors. The results are shown in figure 4.5. The fiber with the silicon core (figure 4.5.b) effectively transmitted light much better than the one with only cladding (figure 4.5.a), where light travels only inside the cladding. This result proves that silicone oil can be successfully used as core for a super stretchable step-index optical fiber.

The ultimate goal of this project would be the fabrication of a single mode liquid core optical fiber. The fabrication of a fully elastomeric optical fiber would require either multiple drawing steps, hardly sustainable by the cladding material, or the non-trivial fabrication of a preform with a core diameter in the order of few hundreds  $\mu m$ , impossible to pursue with the techniques already presented. The possibility of injecting the core material as a liquid inside the hollow core of a preform would instead simplify the process. As we discussed already in the second chapter, a single



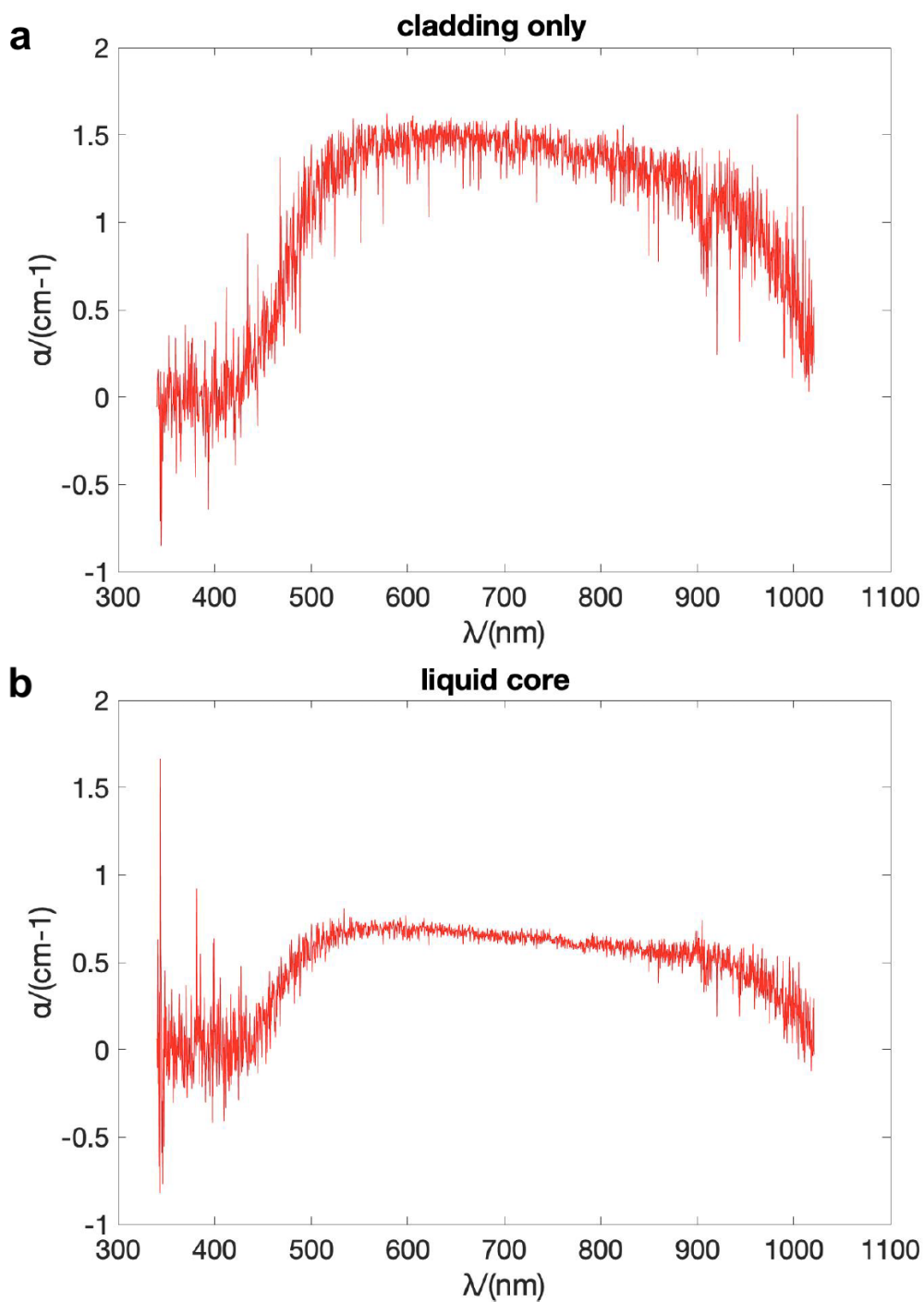


Figure 4.5 – Losses of the fiber with hollow core (a) and Liquid core (b) in the visible and low-IR range, obtained through cut-back measurement.

mode fiber could transmit information with lower losses, and could interface rigid single mode fibers in environments that require mechanical solicitations. In order to transmit only one mode, two factors play a crucial role: the diameter of the core, that should remain in the order of few  $\mu m$ , and the numerical aperture, hence the difference in refractive index between the core and the cladding, that should be as low as possible. We decided therefore to investigate these two parameters individually, in order to conceive the most performing liquid core step-index fiber.

First we wanted to study the impact of the refractive index on light transmission and the feasibility of mixing different oils to tune the refractive index. Unfortunately the pure methyl silicon oil couldn't be mixed effectively with any of the two phenyl-methyl oils we had, at any ratio: the mixture appeared opaque due to small bubbles and didn't improve its optical properties even after weeks spent in a vacuum chamber. We therefore studied the optical properties of the PM oils and their mixtures. We observed that a mixture 1:1 of the oils PM-50 and PM-125 was still giving the same unwanted reaction described before, while a ratio of PM-50:PM-125=6:1 remained transparent. We studied the transmission losses for the three in fibers of similar core diameter, the result is shown in figure 4.6.

As both pure PM-50 and its mixture with PM-125 show higher transmission losses, probably due to different chemical features that reflect in the optical properties, we decided to carry out the rest of the work using only PM-125 oil. We wanted first to study the influence of the core diameter on the light transmission. We know from theory that increasing the size of the diameter increases number of the transmission modes of the light in the core. Higher order modes are usually overlapping with the interface of the cladding and the cladding itself more than the lower order ones and are consequently more lossy. We therefore performed cutback measurement on fibers

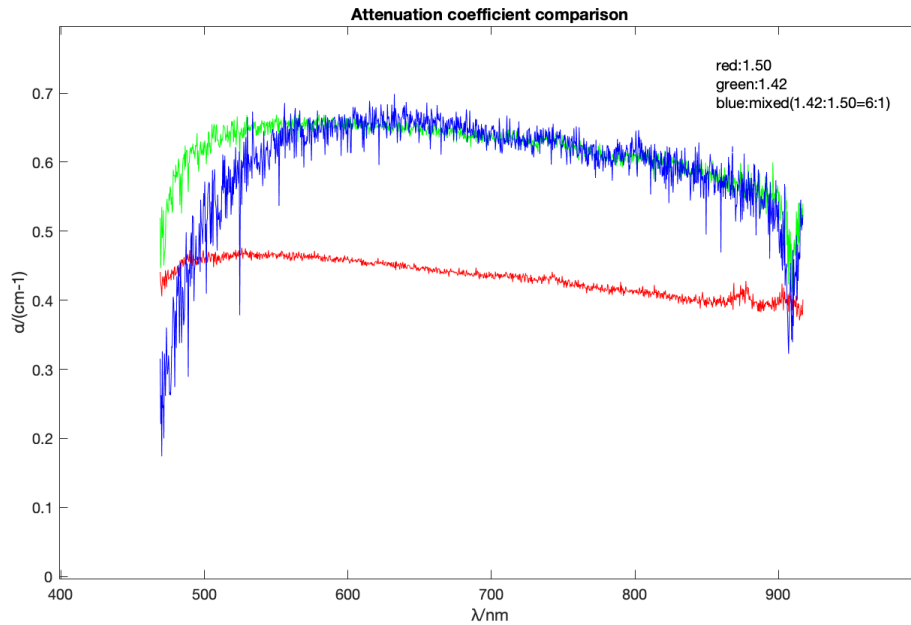


Figure 4.6 – Transmission losses of fibers with different grades of PM oils in the core: PM-50 (green), PM-125 (red) and a mixture PM-50:PM-125=6:1 (blue).

with 3 different core diameters (165, 125, 90  $\mu\text{m}$ ) and compared their transmission losses: as we can see from figure 4.7.a, the transmission losses decrease with the decrease of the diameter.

We decided then to measure the effects of stretching on light transmission. Compared to the cut-back measurement, there is mainly one more factor that could play a role in defining the effective transmission losses of the fiber: the decrease in diameter of the core. The decrease of the diameter, as discussed before, would lead to a smaller V number of the fiber and a smaller number of travelling light modes in the core, which we expect to decrease the transmission losses of the fiber. It's important to clarify that, even if we refer to intrinsic losses of the fiber for the stretching measurement, the "effective" losses we discuss are not the actual losses of the fiber. Instead of using portions of the same fiber at different lengths, we use the same fiber at different stretch elongations. We therefore now that the results don't refer to the actual losses

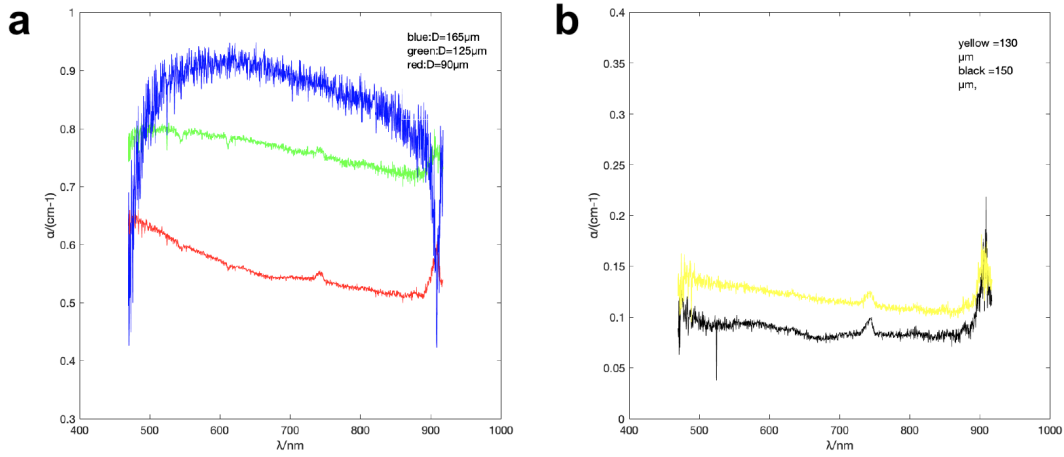


Figure 4.7 – a) Transmission losses of fibers with different diameters. b) effective transmission losses of fibers under stretching).

of the fiber, but they give us valuable information about the light transmission. We recorded the transmission spectra of the fiber at different stretching lengths, and measured the "effective" transmission losses as if the measures were taken for a cut-back measurement. From the right graph of figure 4.7.b, we can see the results of two fibers of core diameters of 130 and 150  $\mu\text{m}$ , comparable with the fibers measured before, showing effective transmission losses way smaller than the fibers measured at rest with constant diameter: this proves our hypothesis of dependence between the core diameter and the light transmission of these fibers. Of course, many other effects could have played a role in mitigate this effect, like the deterioration of the elastomer cladding and decrease of the injected light under stretching, or improved the effect, like the smoothing of the interface induced by the stretching of the fiber.

In this section we proved how Silicon oil can be a valid alternative to elastomers in stretchable optical fibers, opening the path for the development of a new generation of super elastic optical fibers.

### 4.3 Liquid-based 2D photonic fiber

In chapter 3 we presented the fabrication of a stretchable 1D photonic crystal fiber. As discussed already, the main breakthrough that photonic crystals brought to the fiber optics world is the band-gap based light guiding. The simplest photonic crystal fiber and the first ones fabricated and presented to public were the 2D photonic crystal fiber[49]. It was a pure silica fiber with ordered channels shaped in a triangular pattern. Light can travel either in a hollow core, similarly to the 1D photonic crystal fiber discussed already, or, in the simplest case, directly in silica[80]. Although these fibers, from their origin, have been fabricated via thermal drawing, the fabrication of their elastomeric version poses a lot of challenges, from the fabrication of the preform to the drawing itself.

The preforms of the silica fibers are in the order of tens of centimeters in diameter, therefore the fabrication process is less complicated: the channels are obtained either through milling techniques that assure high precision and reliability, or via stack and draw: pre-stretched tubes are assembled in a preform and drawn. These fabrication techniques are not an option anymore if we want to substitute silica with elastomers: the milling process would deform and overheat the material, and even in the case that the channel resulted present, its internal smoothness wouldn't match the requirements for this kind of fiber. The stack and draw technique would be non trivial too: the required consolidation step of stacked elastomer tubes would easily lead to the deformation of the internal architecture. The drawing process itself would be another major challenge: the viscosity of the elastomers we selected wouldn't allow the drawing of hollow channels down to the diameters required for these applications: already a channel of tens of  $\mu m$  would easily collapse on itself.

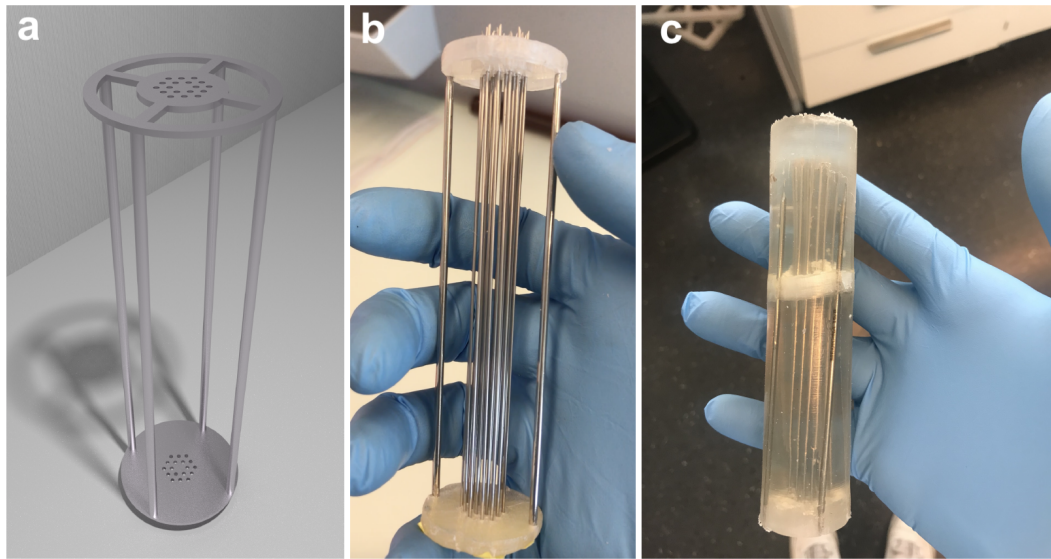


Figure 4.8 – a) Rendered image of the design of the structure to insert in the mould. b) The structure with metallic needles ready to be inserted. c) The structure after the polymer has flown around it.

We addressed the preform fabrication first: instead of fabricating the polymer cylinder first and then create the channels through milling, we decided to directly mould the polymer with the channels inside, in a similar fashion to the technique discussed before to fabricate multicore step index fibers. We therefore needed a structure in the mold and let the polymer flow and solidify around it, but the small diameter required for the channels didn't allow us to use metallic rods screwed at the bottom of the mould. We first tried with a knitted metallic structure to insert in the mould, but it could not ensure an ordered array of channels as the pressure exerted by the piston and the flow of the polymer deformed it. We hence decided to design a structure with a CAD software that could accommodate ordered thin metallic bars inside the preform. The final design resulted in the two discs shown in the rendered image in figure 4.8.a: The lower disc is made to sit at the bottom of the cylindrical mould, while the top disc has to keep the metallic rods in place but still allows the flow of the polymer through itself. These structures were then fabricated through additive

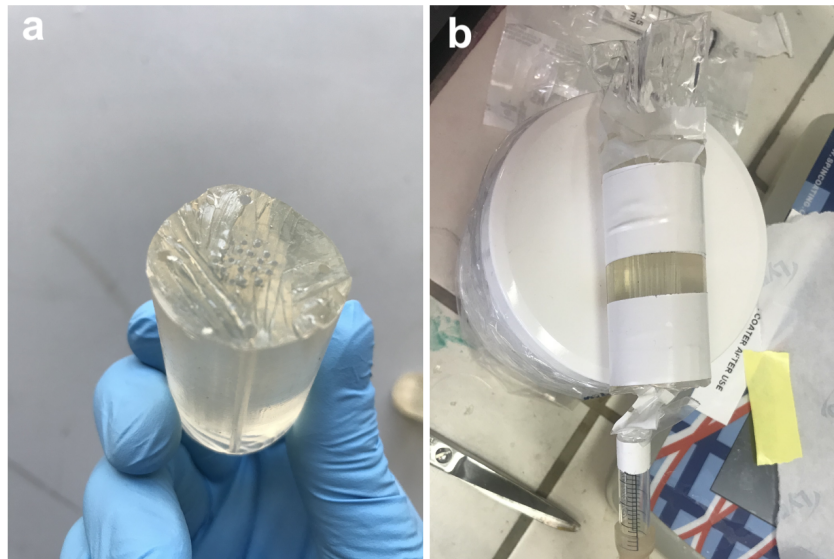


Figure 4.9 – a) A cross-section of the polymer preform after all the rigid parts have been removed. b) The preform getting filled with Silicone oil through vacuum pressure.

manufacturing in a rigid polymer that could sustain the molding temperatures of the elastomer selected (figure 4.8.b). We decided to use SEBs as elastomer for the preform, as its thermo-mechanical properties allow multiple drawing steps with a single preform. After few optimization steps, we successfully managed to fabricate a preform holding all the characteristics we envisioned: a cylindrical preform with an hexagonal array of triangularly-ordered channels of 0.8 mm in diameter, with a central missing channel.

We now needed to face the second fabrication challenge: the drawing of a preform with these thin hollow channels. To overcome the collapse of the channels, we decided to exploit a material already discussed in this thesis, silicone oil. As presented in the previous section, filling hollow channels of elastomeric preforms with silicone oil prevents their collapse during drawing and helps conserving their shape. Waker AK 60000 Siliconol, a methyl silicone oil with refractive index of  $n=1.41$  and viscosity of 50000, was elected for this use. The high viscosity of this oil helps keeping the uniformity of the channel diameter and cross-section, but complicates its injection in



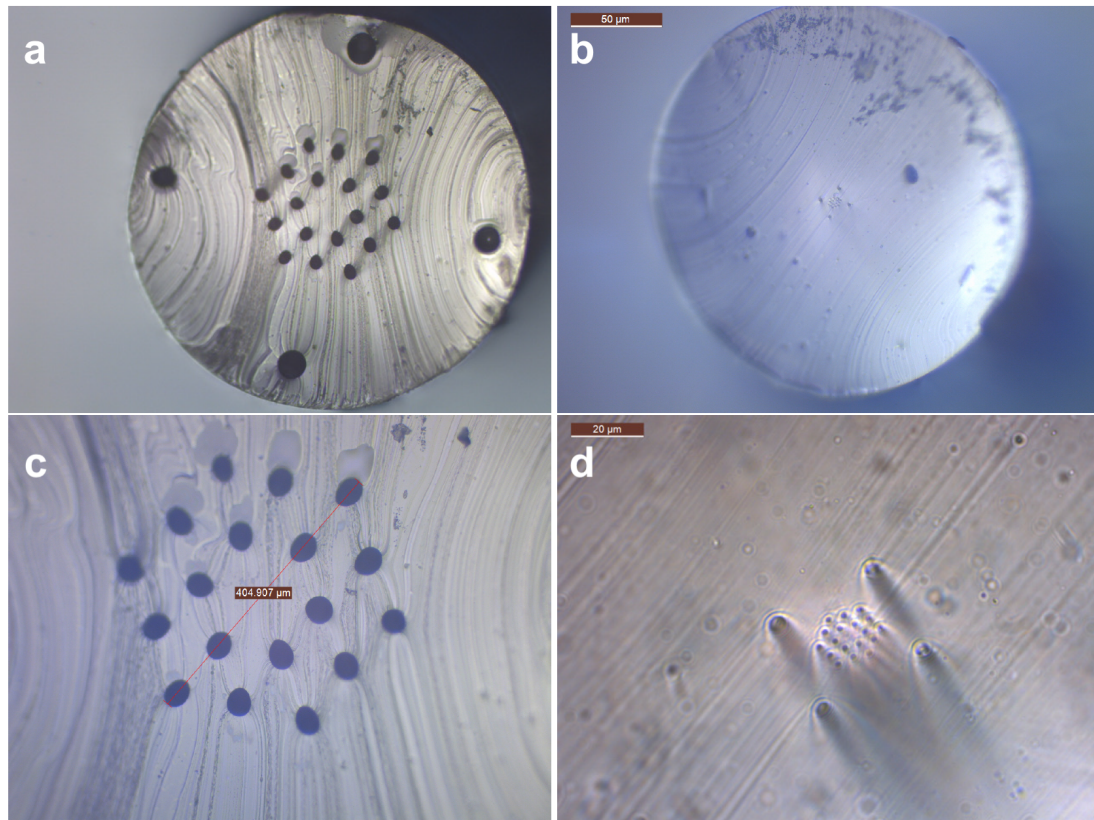


Figure 4.10 – (a,c) Microscope images of the cross-section of the fiber after 1 drawing step. (b,d) Microscope images of the cross-section of the fiber after two drawing steps.

the fiber. After multiple attempts, we found a successful technique to insert it in the channels (figure 4.9.b): The preform was connected to a oil reservoir on one end and a vacuum pump to the other end. A filter was inserted between the preform and the vacuum pump to prevent the oil to enter the pump. In a few hours, the oil successfully filled all the channels of the preform. We then sealed the preform with silicone paste and moved to the drawing step.

We performed one first drawing with a draw-down ratio of around 15 and observed the cross section of the fiber (figure 4.10.a,c): the array of channels is clearly present and doesn't show major modifications in the architecture. The oil can be seen coming



out of every channel therefore is still present. We then added another layer of polymer around the fiber, in order to improve stability, and performed another drawing, with a draw-down ratio still around 15. The microscope image showed clearly that the array of channels is still present and respects the original architecture (figure 4.10.b). The hole diameters don't exceed  $3 - 4\mu m$ , and their presence could be verified through multiple cross-section observations along the fiber axis.

We could therefore confirm that a stretchable photonic crystal-like structure can be successfully fabricated via thermal drawing. This result is paving the way to the development of ultra-soft 2D photonic crystal fibers. We did not have the time to model and characterize these fibers but a continuation of this project is planned beyond my thesis work.

## 5 Conclusion

In this last part we are going to summarize the results of the projects presented and discuss possible outlooks that could be carried out in the future.

### 5.1 Stretchable step-index fiber

We showed the scalable fabrication of highly stretchable, elastomeric step index fiber through thermal drawing. We could obtain tens of meters of fibers from a single preform. The fiber can conduct light down to 0.5 dB/cm, comparable to the best results obtained by highly stretchable fibers to our knowledge. The fiber can sustain deformations up to 500% of its length and be cycled at 100% for thousands of times, without altering its optical properties. We designed and assembled a simple device that could exploit the opto-mechanical properties of the fiber to quantify the force applied to superelastic training bands.

Future research on this project should focus on two different aspects, apparently far from each other and yet quite related. On one side, a deeper understanding of the light transmission mechanisms could help improve the performance of the

fiber and expand its application domains: a systematic study of the core diameter influence, the cladding-core interface roughness and an optimization of the polymer core absorption and refractive index, either by selecting new polymers or collaborating with polymer chemists directly, could gather useful information and pave the way to a new generation of fibers. On the other side, the design of new devices that would exploit the scalability of the fiber drawing process, i.e. large area - low cost sensing platforms, could highlight the major advantages that thermal drawing brings to this field and highlight the strong novelty already present in these results.

## 5.2 Soft 1D photonic crystal fiber

We showed the scalable fabrication of highly stretchable photonic bandgap fiber with a fundamental resonance in the visible. We proved for the first time that these photonic structures can be fabricated in a scalable approach without the use of nanofabrication or others expensive techniques. We showed the stability of these structures, that could still show color after multiple stretching cycles. We could model the opto-mechanical properties of the fiber and track its color shift under stretching.

These results open many exciting research pathways to undertake, both based on a fundamental approach and application oriented. The first objective should be the optimization of the color, that could be carried out in multiple ways, not mutually exclusive: the optimization of the thickness ratio of the double stack of films, the increase of the number of films deposited and the increase of the refractive index difference. Both the optimization of thicknesses and the increase of film number could be dramatically improved by switching to a new deposition technique, that we recently started to study: automatized blade casting technique, allowing us to deposit large area films and control its thickness down to few  $\mu m$ .

Another important step would be the systematic study of the opto-mechanical properties of the fiber. The quantitative measurement of the absolute reflection, an automated cyclical stretching setup paired with a microscopic study of the mechanical damages on the fiber would improve the comprehension of the structures on the fibers and help the fabrication of more resistant fibers ready for the market. One last interesting step, already begun in parallel during the recent times, would be the simulation of the optical properties of textiles made of these fibers. As the color perceived changes with the observation angle, different knitting techniques would result in different play-of-colors and optical effects. The development of a strong knowledge of this aspect would help bridging the gap from the lab results and a possible market and could present new properties not studied before.

## **5.3 Alternative architectures for Stretchable optical fibers**

### **5.3.1 Multicore stretchable optical fiber**

We fabricated for the first time meters of multicore step-index fibers and hybrid multicore-hollow core fibers from which we obtained, through few simple post processing steps, the first fully stretchable multi-purpose fiber probe and we discussed possible breakthrough applications in different fields.

The study of an application, first with a phantom and then eventually directly in vivo could prove the advantages that this kind of fiber fabrication technique and, in particular, this fiber probe could bring to different fields.

### 5.3.2 Liquid core Stretchable optical fiber

For the first time we showed that a hybrid stretchable optical fiber could be fabricated and could actually transmit light with performances down to 0.4 db/cm, comparable if not superior to its elastomeric alternatives. We studied the effect of the core diameter and stretching on light transmission and we could successfully predict the change in performance induced by tuning these parameters.

Effort should be made in the direction of decreasing the number of travelling modes in the fiber, down to the point of showing single mode guiding for the first time in this kind of fibers. As the fabrication of a core with the diameter needed has been already shown and mastered, the main objective would be to build a setup to finely control the injection of light directly in the core and to study the intensity of the beam and its shape at its other end. Another necessary step to obtain this result would be the design of a index-matching sealing at both ends of the fiber, that would optimize light coupling and transmission and prevent liquid leakage.

### 5.3.3 Liquid-based 2D photonic fiber

We identified a clear pathway to the scalable fabrication of fully stretchable 2D photonic crystal fibers. We showed for the first time that these photonic structures could be obtained via thermal drawing and could reach the dimension required to transmit light in the visible.

Before studying the eventual light transmission performance, the fiber structure should be optimized in different ways. First of all, the number of channels should be increased, in order to increase the performance of the photonic crystal: a simple way could be the substitution, in the preform mould, of the metallic rods with metallic

wires under tension. For the same purpose, the optimal distance between the channels and their diameter should be addressed as well: in order to optimally perform, these structures need exact proportions, that can be calculated with finite-difference simulation softwares and depend tightly on the refractive index of the materials. As a consequence, an optimization of the refractive index difference between the elastomer and the core should be performed, either by extracting all the oil from the cores or using an oil with a different refractive index. Subsequently, an accurate characterisation of the optical performances of this fiber could bring exciting results, proving the existence of a new class of photonic crystal fibers.

The thermal drawing process was successfully exploited to realize different types of photonic crystal fibers, from the classic step-index architecture to 1D photonic crystal fibers, liquid core fibers and 2D photonic crystal fibers. A theoretical framework was first established to evaluate the material requirements from a rheological, optical and mechanical point of view and the design of every fiber. A step by step fabrication, from the pellets to the final fiber, was identified and described for each family of fibers. A fully stretchable step-index fiber was fully characterized and proved to be an ideal platform for sensing devices. For the first time, the scalable fabrication of a stretchable photonic fiber with features down to the nm scale was demonstrated and its properties were fully characterized. New architectures for stretchable optical fibers were demonstrated through the fabrication of the fibers.

Future efforts must be addressed mainly in expanding the theoretical comprehension of the physical phenomena that govern light-matter interaction and tune them in order to maximize fiber performances and in the development of new proof-of-concepts to show the possibilities of these fibers in various fields.



## Bibliography

- [1] E. Yablonovitch, *Journal of the Optical Society of America* **1982**, 72, 899–907.
- [2] W. Li, J. Yang, L. Luo, M. Jiang, B. Qin, H. Yin, C. Zhu, X. Yuan, J. Zhang, Z. Luo, Y. Du, Q. Li, Y. Lou, Y. Qiu, J. You, *Nature Communications* **2019**, 10, 3349.
- [3] J. Clark, G. Lanzani, *Nature Photonics* **2010**, 4, 438–446.
- [4] T. Das Gupta, I. Maurin, A. C. H. Rowe, T. Gacoin, *Nanoscale* **2017**, 9, 3504–3511.
- [5] T. Das Gupta, L. Martin-Monier, W. Yan, A. Le Bris, T. Nguyen-Dang, A. G. Page, K.-T. Ho, F. Yesilköy, H. Altug, Y. Qu, F. Sorin, *Nature Nanotechnology* **2019**, 14, 320–327.
- [6] T. D. Gupta, L. Martin-Monier, W. Yan, A. Le Bris, T. D. Nguyen, A. Page, Y. Qu, F. Sorin in Conference on Lasers and Electro-Optics, Optical Society of America, San Jose, California, **2018**, STh1I.5.
- [7] S. Shian, R. M. Diebold, D. R. Clarke, *Optics Express* **2013**, 21, 8669–8676.
- [8] W. J. L. Knollman G C, Bellin J L S, *J Acoust Soc Am (Journal of the Acoustical Society of America)* **1971**, 49, 253–261.
- [9] M. Blum, M. Büeler, C. Grätzel, M. Aschwanden in Proc.SPIE, Vol. 8167, **2011**.
- [10] N. Sugiura, S. Morita, *Applied Optics* **1993**, 32, 4181–4186.



- [11] D.-K. Lim, K.-S. Jeon, H. M. Kim, J.-M. Nam, Y. D. Suh, *Nature Materials* **2010**, 9, 60–67.
- [12] D.-K. Lim, K.-S. Jeon, J.-H. Hwang, H. Kim, S. Kwon, Y. D. Suh, J.-M. Nam, *Nature Nanotechnology* **2011**, 6, 452–460.
- [13] S. Tan, M. Campolongo, D. Luo, W. Cheng, *Nature nanotechnology* **2011**, 6, 268–276.
- [14] G. P. Acuna, F. M. Möller, P. Holzmeister, S. Beater, B. Lalkens, P. Tinnefeld, *Science* **2012**, 338, 506.
- [15] K. Lee, S. A. Asher, *Journal of the American Chemical Society* **2000**, 122, 9534–9537.
- [16] A. C. Sharma, T. Jana, R. Kesavamoorthy, L. Shi, M. A. Virji, D. N. Finegold, S. A. Asher, *Journal of the American Chemical Society* **2004**, 126, 2971–2977.
- [17] E. Tian, J. Wang, Y. Zheng, Y. Song, L. Jiang, D. Zhu, *Journal of Materials Chemistry* **2008**, 18, 1116–1122.
- [18] B. Viel, T. Ruhl, G. P. Hellmann, *Chemistry of Materials* **2007**, 19, 5673–5679.
- [19] Y. Morikawa, S. Nagano, K. Watanabe, K. Kamata, T. Iyoda, T. Seki, *Advanced Materials* **2006**, 18, 883–886.
- [20] S. N. Sheikholeslami, H. Alaeian, A. L. Koh, J. A. Dionne, *Nano Letters* **2013**, 13, 4137–4141.
- [21] D. B. Keck, R. D. Maurer, P. C. Schultz, *Applied Physics Letters* **1973**, 22, 307–309.
- [22] P. A. Xu, A. K. Mishra, H. Bai, C. A. Aubin, L. Zullo, R. F. Shepherd, *Science Robotics* **2019**, 4, DOI 10.1126/scirobotics.aaw6304.
- [23] C. K. Harnett, H. Zhao, R. F. Shepherd, *Advanced Materials Technologies* **2017**, 2, 1700087.

- [24] J. Guo, X. Liu, N. Jiang, A. K. Yetisen, H. Yuk, C. Yang, A. Khademhosseini, X. Zhao, S.-H. Yun, *Advanced Materials* **2016**, 28, 10244–10249.
- [25] N. Bartolomei, Y. Qu, T. N. Dang, W. Yan, A. G. Page, T. D. Gupta, A. Leber, F. Sorin in *Proc.SPIE, Vol. 10872*, **2019**.
- [26] Y. Qu, T. Nguyen-Dang, A. G. Page, W. Yan, T. Das Gupta, G. M. Rotaru, R. M. Rossi, V. D. Favrod, N. Bartolomei, F. Sorin, *Advanced Materials* **2018**, 30, 1707251.
- [27] A. Leber, B. Cholst, J. Sandt, N. Vogel, M. Kolle, *Advanced Functional Materials* **2019**, 29, 1802629.
- [28] C. Guignier, B. Camillieri, M. Schmid, R. Rossi, M. A. Bueno, *Sensors* **2019**, 19, 3011.
- [29] J. A. Rogers, T. Someya, Y. Huang, *Science* **2010**, 327, 1603–1607.
- [30] M. D. Dickey, *Advanced Materials* **2017**, 29, 1606425.
- [31] S. Zhu, J.-H. So, R. Mays, S. Desai, W. R. Barnes, B. Pourdeyhi, M. D. Dickey, *Advanced Functional Materials* **2013**, 23, 2308–2314.
- [32] Z. F. Liu, S. Fang, F. A. Moura, J. N. Ding, N. Jiang, J. Di, M. Zhang, X. Lepró, D. S. Galvão, C. S. Haines, N. Y. Yuan, S. G. Yin, D. W. Lee, R. Wang, H. Y. Wang, W. Lv, C. Dong, R. C. Zhang, M. J. Chen, Q. Yin, Y. T. Chong, R. Zhang, X. Wang, M. D. Lima, R. Ovalle-Robles, D. Qian, H. Lu, R. H. Baughman, *Science* **2015**, 349, 400.
- [33] X. Wang, L. Dong, H. Zhang, R. Yu, C. Pan, Z. L. Wang, *Advanced science (Weinheim Baden-Wurttemberg Germany)* **2015**, 2, 1500169.
- [34] A. Leber, C. Dong, R. Chandran, T. Das Gupta, N. Bartolomei, F. Sorin, *Nature Electronics* **2020**, 3, 316–326.

- [35] C. Dong, A. G. Page, W. Yan, T. Nguyen-Dang, F. Sorin, *Advanced Materials Technologies* **2019**, *4*, 1900417.
- [36] C. Dong, A. Leber, T. Das gupta, R. Chandran, M. Volpi, Y. Qu, T. Nguyen-Dang, N. Bartolomei, W. Yan, F. Sorin, *Nature Communications* **2020**, *11*, DOI 10.1038/s41467-020-17345-8.
- [37] J. Missinne, S. Kalathimekkad, B. Van Hoe, E. Bosman, J. Vanfleteren, G. Van Steenberge, *Optics Express* **2014**, *22*, 4168–4179.
- [38] H. Zhao, K. O'Brien, S. Li, R. F. Shepherd, *Science Robotics* **2016**, *1*, eaai7529.
- [39] V. Prajzler, M. Neruda, M. Květoň, *Journal of Materials Science: Materials in Electronics* **2019**, *30*, 16983–16990.
- [40] M. Hu, R. Deng, K. M. Schumacher, M. Kurisawa, H. Ye, K. Purnamawati, J. Y. Ying, *Biomaterials* **2010**, *31*, 863–869.
- [41] A. Gursoy, K. Iranshahi, K. Wei, A. Tello, E. Armagan, L. F. Boesel, F. Sorin, R. M. Rossi, T. Defraeye, C. Toncelli, *Polymers* **2020**, *12*, DOI 10.3390/polym12030633.
- [42] J. Kallweit, C.-A. Bunge, T. Vad, T. Gries in *Proc.SPIE, Vol. 11355*, **2020**.
- [43] M. Kolle, P. M. Salgard-Cunha, M. R. J. Scherer, F. Huang, P. Vukusic, S. Mahajan, J. J. Baumberg, U. Steiner, *Nature Nanotechnology* **2010**, *5*, 511–515.
- [44] M. Kolle, A. Lethbridge, M. Kreysing, J. J. Baumberg, J. Aizenberg, P. Vukusic, *Advanced Materials* **2013**, *25*, 2239–2245.
- [45] J. D. Sandt, M. Moudio, J. K. Clark, J. Hardin, C. Argenti, M. Carty, J. A. Lewis, M. Kolle, *Advanced Healthcare Materials* **2018**, *7*, 1800293.
- [46] V. P. Patil, J. D. Sandt, M. Kolle, J. Dunkel, *Science* **2020**, *367*, 71.
- [47] M. Malekovic, M. Urann, U. Steiner, B. D. Wilts, M. Kolle, *Advanced Optical Materials* **2020**, *8*, 2000165.

- [48] C. E. Finlayson, C. Goddard, E. Papachristodoulou, D. R. E. Snoswell, A. Kontogeorgos, P. Spahn, G. P. Hellmann, O. Hess, J. J. Baumberg, *Optics Express* **2011**, *19*, 3144–3154.
- [49] T. J. Shepherd, *Electronics Letters* **1995**, *31*, 1941–1943.
- [50] M. A. Duguay, Y. Kokubun, T. L. Koch, L. Pfeiffer, *Applied Physics Letters* **1986**, *49*, 13–15.
- [51] G. J. Pearce, G. S. Wiederhecker, C. G. Poulton, S. Burger, P. S. J. Russell, *Optics Express* **2007**, *15*, 12680–12685.
- [52] W. Belardi, *Journal of Lightwave Technology* **2015**, *33*, 4497–4503.
- [53] F. Sorin, O. Shapira, A. F. Abouraddy, M. Spencer, N. D. Orf, J. D. Joannopoulos, Y. Fink, *Nano Letters* **2009**, *9*, 2630–2635.
- [54] N. D. Orf, O. Shapira, F. Sorin, S. Danto, M. A. Baldo, J. D. Joannopoulos, Y. Fink, *Proceedings of the National Academy of Sciences* **2011**, *108*, 4743.
- [55] J. J. Kaufman, G. Tao, S. Shabahang, E.-H. Banaei, D. S. Deng, X. Liang, S. G. Johnson, Y. Fink, A. F. Abouraddy, *Nature* **2012**, *487*, 463–467.
- [56] M. Yaman, T. Khudiyev, E. Ozgur, M. Kanik, O. Aktas, E. O. Ozgur, H. Deniz, E. Korkut, M. Bayindir, *Nature Materials* **2011**, *10*, 494–501.
- [57] W. Yan, A. Page, T. Nguyen-Dang, Y. Qu, F. Sordo, L. Wei, F. Sorin, *Advanced Materials* **2019**, *31*, 1802348.
- [58] M. Bayindir, O. Shapira, D. Saygin-Hinczewski, J. Viens, A. F. Abouraddy, J. D. Joannopoulos, Y. Fink, *Nature Materials* **2005**, *4*, 820–825.
- [59] A. Stolyarov, L. Wei, F. Sorin, G. Lestoquoy, J. Joannopoulos, Y. Fink, *Applied Physics Letters* **2012**, *101*, DOI 10.1063/1.4733319.

- [60] S. Gorgutsa, J. Gu, M. Skorobogatiy, *Smart Materials and Structures* **2011**, *21*, 015010.
- [61] N. Chocat, G. Lestoquoy, Z. Wang, D. M. Rodgers, J. D. Joannopoulos, Y. Fink, *Advanced Materials* **2012**, *24*, 5327–5332.
- [62] T. Nguyen-Dang, A. C. de Luca, W. Yan, Y. Qu, A. G. Page, M. Volpi, T. Das Gupta, S. P. Lacour, F. Sorin, *Advanced Functional Materials* **2017**, *27*, 1605935.
- [63] A. Leber, A. G. Page, D. Yan, Y. Qu, S. Shadman, P. Reis, F. Sorin, *Advanced Functional Materials* **2020**, *30*, 1904274.
- [64] M. Alexander Schmidt, A. Argyros, F. Sorin, *Advanced Optical Materials* **2016**, *4*, 13–36.
- [65] U. Brush, A. Chaudhari, A. Steven, Lavender, **2020**.
- [66] G. Keiser, F. Xiong, Y. Cui, P. P. Shum, *Journal of Biomedical Optics* **2014**, *19*, 1–29.
- [67] K. Peters, *Smart Materials and Structures* **2011**, *20*, 13002.
- [68] J. D. Joannopoulos, S. G. Johnson, J. N. Winn, R. D. Meade, *Photonic Crystals: Molding the Flow of Light*, 2nd, Princeton University Press, USA, **2008**.
- [69] S. G. Johnson, M. Ibanescu, M. Skorobogatiy, O. Weisberg, T. D. Engeness, M. Soljačić, S. A. Jacobs, J. D. Joannopoulos, Y. Fink, *Optics Express* **2001**, *9*, 748–779.
- [70] L. A. Weller-Brophy, D. G. Hall, *Journal of the Optical Society of America A* **1985**, *2*, 863–871.
- [71] A. Broadbent, *Color Research & Application* **2004**, *29*, 267–272.
- [72] C. Wyman, P.-P. Sloan, P. Shirley, *Journal of Computer Graphics Techniques (JCGT)* **2013**, *2*, 1–11.
- [73] C. J. Brinker, G. C. Frye, A. J. Hurd, C. S. Ashley, *Thin Solid Films* **1991**, *201*, 97–108.

- [74] L. E. Scriven, *MRS Proceedings* **1988**, 121, 717.
- [75] L. Songhan Plastic Technology Co., *Wacker Silicones Geniomer® 140 Silicone TPE* - <http://www.lookpolymers.com/pdf/Wacker-Silicones-Geniomer-140-Silicone-TPE.pdf>.
- [76] National Center for Biotechnology Information (2020)., *PubChem Compound Summary for CID 6212, Chloroform*. Retrieved October 25, 2020 from <https://pubchem.ncbi.nlm.nih.gov/compound/Chloroform>.
- [77] M. Kolle, B. Zheng, N. Gibbons, J. J. Baumberg, U. Steiner, *Optics Express* **2010**, 18, 4356–4364.
- [78] Y. Guo, C. F. Werner, A. Canales, L. Yu, X. Jia, P. Anikeeva, T. Yoshinobu, *PLOS ONE* **2020**, 15, e0228076–.
- [79] O. Poupart, A. Schmocker, R. Conti, C. Moser, K. M. Nuss, H. Grützmacher, P. J. Mosimann, D. P. Pioletti, *Frontiers in Bioengineering and Biotechnology* **2020**, 8, 261.
- [80] P. Russell, *Science* **2003**, 299, 358.